1-1-2009

Explicit Finite Element Modeling of Knee Mechanics During Simulated Dynamic Activities

Mark A. Baldwin
University of Denver

Follow this and additional works at: https://digitalcommons.du.edu/etd

Part of the Computer-Aided Engineering and Design Commons

EXPLICIT FINITE ELEMENT MODELING OF KNEE MECHANICS DURING

SIMULATED DYNAMIC ACTIVITIES

_____

A Dissertation

Presented to

The Faculty of Engineering and Computer Science

University of Denver

_____

In Partial Fulfillment

of the Requirements for the Degree

Doctor of Philosophy

_____

by

Mark Baldwin

June, 2009

Advisor: Paul J. Rullkoetter

GRADUATE STUDIES

AT

THE UNIVERSITY OF DENVER

Upon the recommendation of the chairperson of the Department of Mechanical and Materials Engineering, this dissertation is hereby accepted in partial fulfillment of the requirements for the degree of

Doctor of Philosophy

_____
Professor in charge of dissertation

_____
Vice Provost for Graduate Studies

_____
Date

Author: Mark A. Baldwin
Title: EXPLICIT FINITE ELEMENT MODELING OF KNEE MECHANICS
DURING SIMULATED DYNAMIC ACTIVITIES
Advisor: Paul J. Rullkoetter
Degree date: June, 2009

ABSTRACT

The natural knee is one of the most commonly injured joints in the body due to relatively high loads and motions that can lead to debilitating degenerative diseases such as osteoarthritis. Total knee arthroplasty is a clinically successful method for eliminating pain in the osteoarthritic knee, but is subject to complications that can affect patient satisfaction and long-term implant performance. The work presented in this dissertation is a demonstration of how anatomic three-dimensional (3D) computational knee models can be an effective alternative for investigating knee mechanics when compared to the cost and time prohibitive nature of i*n-vivo* and *in-vitro* methods. The studies described in this work utilized the explicit finite element (FE) method to investigate varying aspects of soft tissue constraint, implant alignment, and applied dynamic loading on knee mechanics in 3D natural and implanted partial or whole joint knee models.

Combined probabilistic and FE methods were used to successfully identify the most important parameters affecting joint laxity in the natural knee and patellar component alignment in the implanted knee. Two model verification studies demonstrated strong agreement between model-predicted and experimental 3D kinematics of specimen-specific isolated patellofemoral and whole joint cadaveric knee models under simulated dynamic loading (deep knee bend and gait) collected in a

mechanical simulator. Using one of the single specimen whole joint models, an additional study successfully identified the most important anatomic and implant alignment parameters related to a clinically-relevant complication associated with a particular implant design. Lastly, a new method of efficiently generating 3D natural articular knee surfaces for FE analysis was developed through a combined mesh morphing and statistical shape modeling approach. These studies included several novel methods for investigating knee mechanics under dynamic loading and specimen-specific soft tissue constraint using the explicit FE method that could be used to better reproduce the complex *in-vivo* knee environment in forward or muscle-driven models and to assist design-phase implant performance evaluation.

ACKNOWLEDGEMENTS

TABLE OF CONTENTS

LIST OF FIGURES

LIST OF TABLES

CHAPTER 1. INTRODUCTION

Computational biomechanics is a continuously developing field applying the tools of engineering analysis to clinical and biological phenomena that remain elusive or difficult to understand. With improvements in computational processing speed and power, increasingly sophisticated and complex biomechanical models can be developed to approach more accurate and anatomic representations of the *in-vivo* biomechanical environment. Understanding mechanics of the natural and implanted knee is one area of research where biomechanical models can have a direct impact on improving clinical outcomes. The knee joint is the largest and most complex joint in the human body. Due to the large motions and applied loads, the knee is also one of the most common sites of injury and degenerative diseases such as osteoarthritis (OA).

In the case of knee OA, the harsh mechanical environment and progressive degradation of the weight-bearing articular cartilage often leaves few long-term options besides total joint replacement. The most common and most successful method for alleviating patient knee pain from OA is partial or total knee arthroplasty (TKA). This is a surgical procedure where the degenerated articular knee surfaces are removed along with some of the underlying bone and replaced with custom-designed plastic and metallic prosthetic components. Although the surgical technique and component materials have steadily improved over several decades, there remain post-operative complications (i.e. implant loosening from the bone) and physiologic limitations (i.e.

reduced range of motion) that are still not well understood and could potentially benefit from computational biomechanical evaluations.

Computational knee models are paramount during the design phase of joint replacement development, as insight into the kinematics and contact stresses/strains can guide design decisions without the cost and time associated with manufacturing parts and subsequent experiments. However, assessing long-term *in-vivo* performance of TKA implants is difficult to perform computationally due to the complex relationship between component design, surgical alignment, patient-specific anatomy, and ligamentous constraint. For this reason, computational implant evaluations have focused on reproducing the more controlled and repeatable loading environment of dynamic mechanical simulators. Studies by Godest et al. and Halloran et al. were able to demonstrate strong agreement between model-predicted and experimental three-dimensional (3D) kinematics of implant-only testing in mechanical knee simulators using the explicit finite element (FE) method (Godest et al., 2002; Halloran et al., 2009; Halloran et al., 2005c). These studies were an important step in laying the foundation for more complicated model verification under the influence of anatomic soft tissue constraint.

In large part, the work presented in this dissertation focused on improving computational representation of ligamentous constraint around the knee and modeling simulated dynamic activities. This was accomplished through a progression of studies starting with simplified one-dimensional (1D) ligament representations of natural knee structures manually optimized to match published laxity responses at two distinct

flexion angles. In a subsequent model-verification study, a more sophisticated two-dimensional (2D) ligament model was used to reproduce specimen-specific constraint of an isolated portion of the knee joint in both natural and implanted knee models under dynamic loading conditions. The final and most elaborate study applied 2D and 3D ligaments to a series of specimen-specific implanted knee models to verify model-predicted simultaneous whole joint kinematics against experimental measurements for two simulated dynamic activities. This study demonstrated a novel method for establishing specimen-specific constraint through ligament parameter optimization to match experimental laxity responses. Overall, the goal of this work was to develop a suite of computational tools that may assist in improving long term implant performance and potentially reduce the design cycle through improved representation of ligamentous constraint and FE techniques.

1.1. Dissertation Overview

Chapter 2 provides an overview of the necessary clinical terminology and relevant knee anatomy that is extensively used in subsequent chapters. There is also a brief discussion of the TKA process and a description of the fundamentals behind explicit FE modeling. Chapter 3 describes the mechanical behavior of ligaments and discusses some of the technical aspects of representing their function in a computational platform. Chapter 4 presents a computationally efficient probabilistic natural knee ligament model to identify the most important ligament characteristics affecting predicted joint laxity. Chapter 5 presents a probabilistic implanted patellofemoral joint model for identifying the most important TKA component alignment parameters

3

affecting predicted kinematics and contact mechanics for two common designs. The studies presented in Chapters 4 and 5 demonstrate the value of coupling "representative" FE knee models with probabilistic methods to identify important parameters and extrapolate a single knee model to a larger theoretical population.

Chapters 6 and 7 present studies verifying model predictions against experimental measurements for multiple natural and implanted knee cadaveric specimens. The study in Chapter 6 focused on the isolated patellofemoral joint to limit model complexity and to implement a method for representing ligamentous constraint with a fiber-reinforced material model. Model verification was performed by comparing predicted six degree-of-freedom (DOF) patellar kinematics in four natural and implanted specimen-specific knees against experimental measurements of a simulated deep knee bend activity in a mechanical knee simulator. Chapter 7 describes a follow up study in which simultaneous whole joint kinematics were predicted during simulated deep knee bend and gait cycles in the mechanical simulator in four implanted specimen-specific knee models using a novel method for matching tibiofemoral constraint to experimental measurements through ligament parameter optimization.

Chapter 8 presents an application of the verified knee models in addressing a clinical complication associated with a particular TKA design. Chapter 9 describes a method for efficiently generating natural whole joint knee models using a semi-automated geometry extraction and statistical shape modeling tool to provide a suitable baseline for future studies comparing the natural and implanted knee joint. Chapter 10 presents a summary of the work and makes recommendations for future research.

CHAPTER 2. BACKGROUND INFORMATION

The field of computational biomechanics necessitates an intimate knowledge of anatomy and physiology, computational methods, and classical engineering. Each field has its own specific terminology to describe relevant information. This chapter provides an overview of the important clinical aspects of computational biomechanics related to modeling the natural and implanted knee and using the explicit finite element method. The first section describes relevant clinical terminology, the second describes natural knee anatomy, the third presents an overview of the total knee replacement process, the fourth briefly covers technical aspects of the explicit finite element method, and the fifth provides a brief overview of the simulated annealing global optimization algorithm used in Chapter 7.

2.1. Clinical Terminology

In human anatomy, all naming is based on positions relative to the body in standing position with arms at the side and palms facing forwards (Figure 2.1). The body can be divided into three anatomic planes: sagittal, coronal (frontal), and transverse (axial). The sagittal plane divides the body into right and left halves from head to toe. The coronal plane also runs head to toe and divides the body into anterior (belly) and posterior (back) sections. The transverse plane is perpendicular to the sagittal and coronal planes and divides the body into inferior (head) and superior (toe) sections.

When describing clinical motions or anatomic locations, directions are often referred to within the anatomic planes as follows: anterior motion moves away from the body on the belly side, posterior motion moves away from the body on the back side; superior motion moves from the toes towards the head, inferior motion moves from the head towards the toes; medial motion moves towards the centerline of the body and lateral motion away from the body centerline. In describing anatomic structures, it is common to combine terms to indicate the relative spatial location within two planes (e.g. anteroinferior border). Additionally, the terms proximal and distal may be used to indicate an object is closer to the center of the body (proximal) or farther away from the body center (distal).

2.2. Natural Anatomy of the Knee

The knee is the largest and most complex joint in the human body with multiple contoured articulating surfaces, load-bearing soft tissue structures, and muscles acting to flex and extend the lower limb. The knee is a diarthrodial (freely moveable) joint typically described as having three compartments or joints: the patellofemoral and medial and lateral tibiofemoral joints (Figure 2.2). Bony surfaces of the femur, tibia, and patella are covered with hyaline cartilage that provide a smooth and durable surface for articulations under loads that can reach multiple times body weight during extreme activities (i.e. jump landing). There are two main muscle groups acting on the knee that cause it to either flex or extend. The primary knee extensors, often referred to as the quadriceps group, consist of the rectus femoris, vastus intermedius, vastus medialis and vastus lateralis. The latter two muscles are typically subdivided into longus and

obliquus portions to differentiate the force line of action on the patella (Farahmand et al., 1998) (Figure 2.3). These muscles attach directly to the anterior, superior, and medial and lateral borders of the patella and indirectly to the tibial tubercle via the patellar tendon to extend the tibia. The entire joint is surrounded by numerous load bearing ligamentous structures that provide passive structural support through the normal range of motion and a fibrous capsule to retain synovial fluid and lubricate the articular surfaces. The following section describes the anatomy and biomechanics of the relevant knee ligament structures in more detail.

2.2.1. Soft Tissue Structures of the Knee

Due to their high frequency of injury, soft tissue structures of the knee have been studied extensively. The primary load bearing soft tissue structures crossing the natural tibiofemoral joint are the anterior and posterior cruciate ligaments (ACL, PCL), the medial (tibial) and lateral (fibular) collateral (MCL, LCL) ligaments, and the medial and lateral menisci (Figure 2.4). Soft tissues of the patellofemoral joint, often referred to as the extensor mechanism, include the patellar and quadriceps tendons and medial and lateral patellofemoral ligaments (MPFL, LPFL) (Figure 2.5). Each ligament structure provides directional constraint under applied loading that is specific to its bony attachments, fiber orientation, and dimensions. The majority of studies presented in this work concentrated on biomechanics of the implanted knee in which the menisci and one or both cruciate ligaments are removed. Thus, description of ligament structures in the following sections were focused primarily on the remaining capsular structures that are important in guiding motion or affecting mechanics of the implanted knee.

2.2.2. Medial Knee Constraint

The medial ligament complex of the knee includes one large ligament and a series of capsular thickenings and tendinous attachments (LaPrade et al., 2007a). The primary stabilizer and largest structure on the medial side of the knee is the superficial medial collateral ligament (sMCL), which is roughly 100 to 120 mm long attaching to the femur on (Warren and Marshall, 1979) or slightly proximal and posterior to the medial epicondyle (LaPrade et al., 2007a) and to the posteromedial crest of the tibia (Figure 2.6). The sMCL ligament is relatively flat and broad with fibers running parallel to the tibia and femur in the inferior-superior direction. The primary function of the sMCL is to prevent medial opening of the knee (valgus rotation), but it can also act as a secondary restraint against tibial rotations and anterior-posterior translations (Robinson et al., 2006). The posteromedial corner of the knee contains a combination of fibrous tendon connections and a more distinct load bearing structure called the posterior oblique ligament (POL) (LaPrade et al., 2007a; Robinson et al., 2006; Wymenga et al., 2006) that attaches on the femur posterior and proximal to the sMCL. The ligament courses posteriorly and distally to the posterior edge of the tibia. It's primary function is near full extension where it restricts valgus and internal tibial rotation and posterior tibial translation (Amis et al., 2003a; Hughston and Eilers, 1973; Petersen et al., 2008; Robinson et al., 2006).

On the medial side of the patellofemoral joint, the MPFL is a flat, broad ligament band approximately 60 mm long and 30 mm wide that courses from the medial border of the patella to the adductor tubercle of the femur (Amis et al., 2003b; Nomura

et al., 2000; Nomura et al., 2005; Smirk and Morris, 2003). Its primary function is to restrict lateral translation of the patella in early to mid flexion.

2.2.3. Lateral and Posterolateral Knee Constraint

The primary load bearing ligamentous structures on the lateral side of the knee consist of the LCL, the popliteofibular ligament (PFL), lateral retinacula, and LPFL (Figure 2.7). The LCL is a thin, strong fibrous band that is approximately 60-70 mm long and 4 mm wide. Its femoral attachment has been described as either on (Woo et al., 2006) or slightly proximal and posterior to (LaPrade et al., 2003) the lateral femoral epicondyle with a distal attachment on the lateral aspect of the proximal fibula. The primary function of the LCL is to restrict the lateral side of the knee from opening (varus rotation) and is a secondary stabilizer for external tibial rotation and posterior tibial translation.

An additionally important lateral stabilizing ligamentous structure that is often the source of disagreement or confusion is the combination of the popliteus tendon and PFL (Maynard et al., 1996; Shahane et al., 1999; Veltri et al., 1996). The popliteus tendon is attached to the femur in the popliteus sulcus which is just proximal to the lateral femoral cartilage border, but distal and anterior to the LCL femoral attachment. The PFL joins the popliteus tendon at the musculotendinous junction (about 50 mm away from its femoral attachment) distal and posterior to the LCL femoral attachment and inserts on the proximal portion of the fibula. Due to their combined functional role in restraining varus and external tibial rotations and posterior tibial translations, the popliteus tendon and PFL will be referred to simply as the PFL (LaPrade et al., 2003).

9

The entire knee joint is surrounded by a fibrous capsule with varying thickness and strength. On the anterolateral aspect of the knee, constraint is provided by the capsule, the iliotibial tract, and the LPFL (Evans, 1979; Recondo et al., 2000). The iliotibial tract is an extension of the fascia lata and ends at the Gerdy tubercle passing over the lateral tibiofemoral joint. The combination of the lateral capsule and iliotibial tract is used in a subsequent laxity envelope study and referred to as simply the anterior lateral capsule (ALC). Similar to the MPFL on the medial side of the patellofemoral joint, the LPFL is a fibrous band running from the lateral patellar border to the lateral femoral epicondyle and is the primary restraint to patellar medial translation. The LPFL structure is smaller and weaker than the MPFL, but has a similar function to the MPFL which assists in guiding patellar motion in early to mid flexion (Atkinson et al., 2000).

2.2.4. The Quadriceps and Patellar Tendons

Understanding the anatomy and function of the quadriceps and patellar tendons is critical to computational investigations of patellar kinematics and contact mechanics. The quadriceps tendon is a thick (~ 8 mm) and broad band of fibrous tissue comprised of the distal portions of the rectus femoris, vastus medialis, lateralis, and intermedius muscle tendons (Figure 2.8). It is approximately 50 mm long proximal to its attachment on the superior patellar border (Staeubli et al., 1999). The most anterior aspect passes over and attaches to the anterior face of the patellar bone. At the base of the patella, the quadriceps tendon fuses with the patellar tendon which then attaches to the tibial tuberosity. The patellar tendon is shorter (~40 mm) and smaller than the quadriceps tendon, but has been shown to have a higher Young's modulus (Stäubli et al., 1999).

10

2.3. Total Knee Arthroplasty

Osteoarthritis (OA) is a painful condition in which the articular cartilage and the underlying subchondral bone become damaged and can no longer function normally. When OA occurs in the knee, treatment options are limited due to the harsh mechanical environment induced by large relative motions and applied loads on the femoral, tibial, and patellar cartilage surfaces. Total knee arthroplasty (TKA) is a common surgical procedure to eliminate joint pain by replacing damaged cartilage and bony surfaces with prosthetic components. The procedure consists of opening the joint via an incision on the medial side of the knee and performing bone cuts on the distal femoral, proximal tibial and posterior patellar bony surfaces (Figure 2.9). Custom-designed and sized metallic (cobalt chromium molybdenum alloy) femoral components and ultra-high-molecular-weight polyethylene tibial and patellar components are rigidly fixed to the cut bony surfaces using polymethylmethacrylate bone cement.

Different types of TKA designs may be used depending on patient requirements or surgical philosophy, but the two main types are categorized by whether they retain or eliminate the PCL. Although selection of either design type has been the subject of much disagreement within the orthopedic community, proponents of cruciate retaining (CR) designs believe it is beneficial because it retains more of the original joint anatomy and allows the PCL to influence knee motion more naturally. Proponents of TKA designs that eliminate the PCL, also known as posterior stabilized (PS) designs, tend to believe that component placement restoring natural PCL function is difficult to achieve and may induce undesirable motions that could lead to component

complications such as wear or loosening. Regardless of TKA design type, there exists considerable variability in component placement and difficulty assessing long-term implant performance under the influence of ligamentous constraint and muscle loads.

2.4. Explicit Finite Element Modeling

There are numerous commercially available and custom-developed rigid body and finite element (FE) solvers available for performing computational biomechanical studies. The work presented in this dissertation was performed using the Explicit FE solution method in the commercially available solver ABAQUS^{TM} (Dassault Systemes, Providence, RI). In general, the FE method discretizes actual geometry by sub-sectioning it into finite-sized elements of varying shapes connected by nodes. The Explicit solution method uses the central difference rule to integrate the equations of motion explicitly through time from one time increment to the next by solving for dynamic equilibrium. Using Newton's second law of motion, the nodal accelerations at the beginning of the current increment (t) are calculated using:

$$a(t) = M^{-1} [P(t) \cdot I(t)] \qquad\qquad \text{Equation 2.1}$$

where a(t) is the current nodal accelerations, M is the lumped mass matrix, and P and I are the external applied and internal element forces, respectively. The Explicit method assumes that using small enough time increments (Δt), the nodal accelerations are constant. This can be used to determine the change in velocity at the middle of the current increment $v_{(t+\Delta t/2)}$ based solely on the velocity from the middle of the previous increment $v_{(t-\Delta t/2)}$ using the equation:

$$v_{(t+\Delta t/2)} = v_{(t-\Delta t/2)} + (\Delta t_{(t + \Delta t)} + \Delta t_{(t)})/2 \cdot a(t) \qquad \text{Equation 2.2}$$

The velocities are integrated through time and added to the displacements at the beginning of the increment to determine the displacements at the end of the increment using:

$$u_{(t+\Delta t)} = u_{(t)} + \Delta t_{(t + \Delta t)} \cdot v_{(t+\Delta t/2)} \qquad \text{Equation 2.3}$$

Once the nodal accelerations are determined from Equation 2.1, the velocities and displacements are advanced "explicitly" through time (i.e. based only on the displacements, velocities, and accelerations at the beginning of the increment) using Equations 2.2 and 2.3, which makes the analysis conditionally stable with small enough time increments. Once the nodal displacements have been determined for the current increment, the element strains, strain rates, and stresses can be determined from the material constitutive relationships for each element type, populating the matrix of internal nodal forces $I_{(t + \Delta t)}$ for the next increment $(t + \Delta t)$. The Explicit FE method is well suited for solving biomechanical problems as it can resolve discontinuous events and intermittent contact situations such as ligament-to-bony contact in a simulated deep flexion activity.

An additional benefit to the explicit FE method is the dependence on a material-based stability limit and related controls for improving model run times with minimal to no impact on predicted results. The ABAQUS/Explicit solution method calculates an efficient and conservative estimate of the highest element frequency in the model to determine the stability limit (the largest allowable time increment Δt). The stability

13

limit is based on an approximation of the shortest element edge length (L_e) divided by the wave speed of the material in that element (c_d) which is calculated as the square root of the Young's modulus (E) over the mass density (ρ). This indicates that the stable time increment will need to be smaller with a stiffer material (higher E), leading to longer total run times. Conversely, if the density is higher, the wave speed of the material decreases and the total run time decreases.

In application, the dependence of the explicit solution method on the material-based stability limit can be optimized by either generating a well controlled mesh (thereby maximizing L_e) for a given geometry or adjusting the material properties (E, ρ) to an acceptable level while monitoring model predictions. In the case of predicting internal stresses and strains, the analyst must ensure that the mesh density, element type, and material definitions are appropriate for the problem at hand. Otherwise, additional controls such as fixed mass scaling, which applies a small amount of mass to elements below a specified stable time increment, can be used to decrease overall model run times with negligible effects on overall model predictions. The development of a 2D and 3D fiber-reinforced deformable ligament representation described in the following section is an example of using this knowledge of explicit techniques to maximize efficiency (minimize run time) while maintaining a level of accuracy required for complex biomechanical analyses.

2.5. Simulated Annealing Global Optimization Algorithm

There are a number of algorithms available for optimization in numerical analysis, but oftentimes selecting the most efficient and accurate algorithm for the given

problem is difficult a priori. Non-gradient based methods are the simplest to implement but often require more function evaluations than are necessary to achieve convergence. In the case of FE analyses, which may take a substantial amount of time per evaluation depending on the analysis, these algorithms are often unacceptable. Gradient-based algorithms may be subject to converging on local minima and are largely dependent on the initial guess. Global search algorithms have been developed to address some of these shortcomings and to improve efficiency in complex, multi-variable design spaces.

Chapter 7 presents a process for computational representation of specimen-specific tibiofemoral constraint using a global search optimization algorithm called simulated annealing. This algorithm is based on random evaluations of the cost function in such a way that transitions out of a local minimum are possible (Corana and Marchesi, 1987). It was selected for specimen-specific constraint optimization because of the unknown relationship between the 17 input variables and predicted laxity responses at multiple flexion angles and its robustness in escaping local minima. The algorithm name was obtained because of its analog to the physical process of cooling a material (annealing) whereby slow, careful cooling will allow the material to become highly ordered, low energy state (global minimum) compared to rapid cooling that may yield defects and leave the material at a higher energy state (local minimum). An initial "temperature" is specified that defines the search space. This temperature is reduced via a "cooling rate" reduction factor that progressively reduces the search space for all input variables to focus in on a global minimum. The algorithm robustness to local minima and its independence of start values comes from acceptance of both uphill and downhill points as a function of the current temperature and change in the output (Goffe

et al., 1994). In application, convergence and efficiency are dependent on appropriate values for the initial temperature and reduction factor, but when properly implemented, the algorithm has demonstrated efficient convergence to and successful identification of global minima.
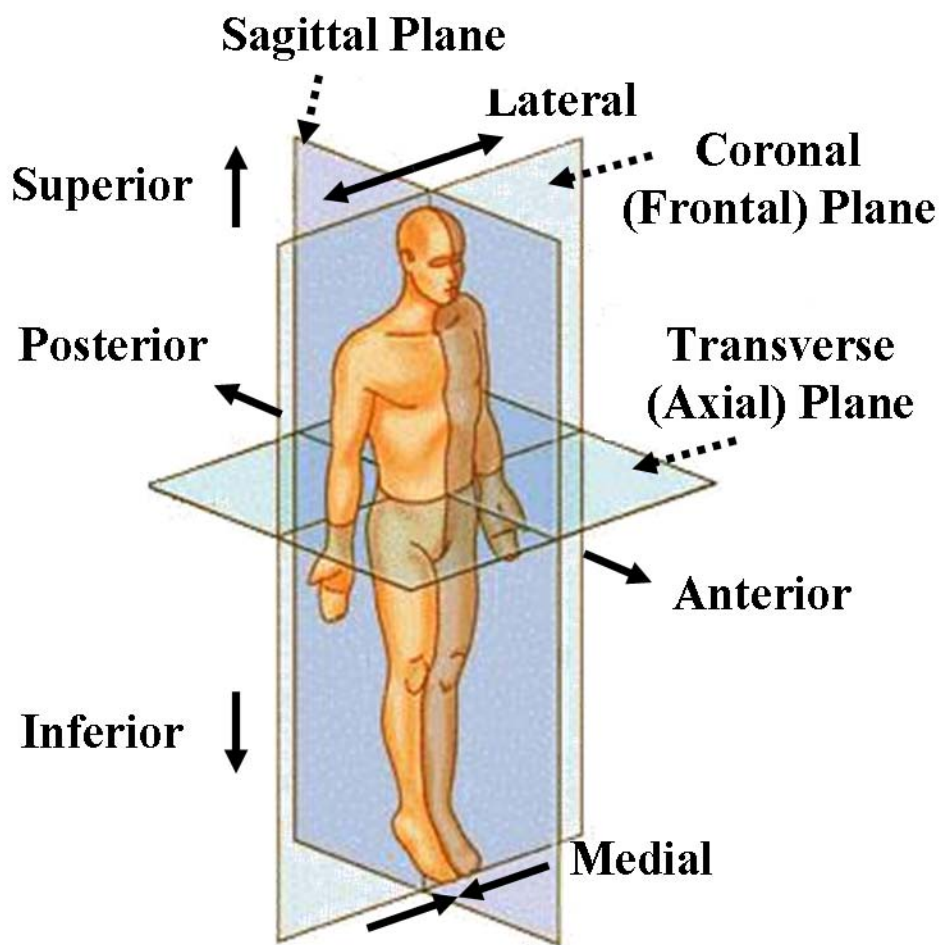
Figure 2.1 Diagram of anatomic planes and clinical directions (SEER's Training Website, 2004).

The Human Knee
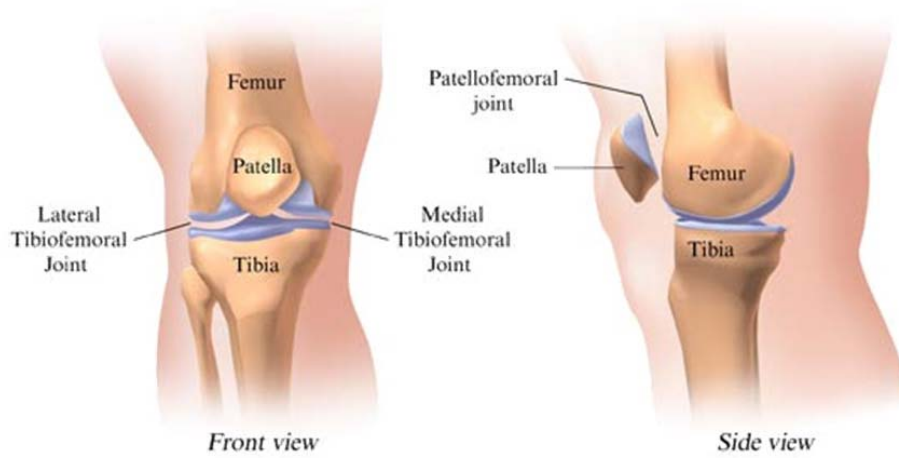
Figure 2.2 Diagram of the natural knee (www.mayclinic.org).
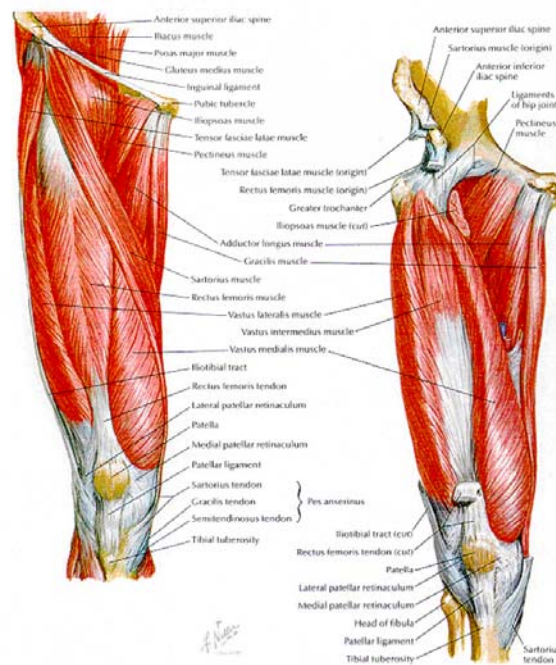
Figure 2.3 Extensor muscles acting on the knee joint (Netter, 2006).
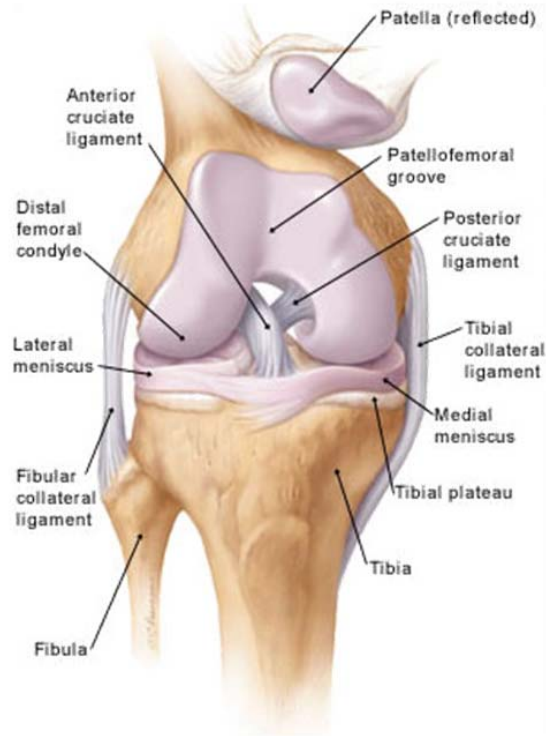
Figure 2.4 Diagram of natural knee soft tissue structures crossing the tibiofemoral joint (www.larsligament.com).
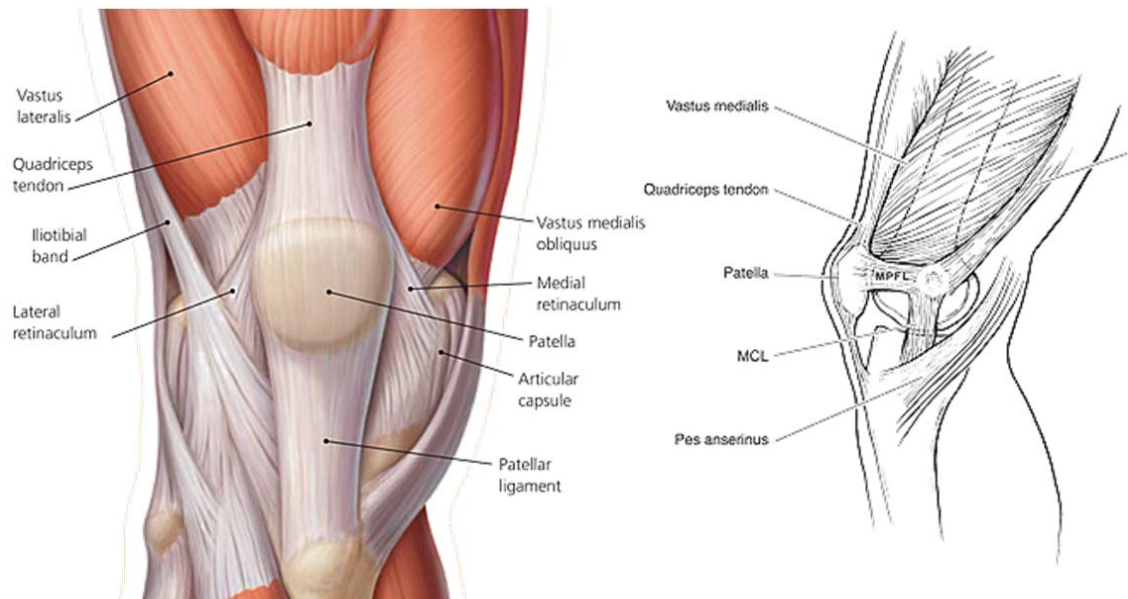
Figure 2.5 Diagram of the patellofemoral joint demonstrating location of medial patellofemoral ligament (MPFL) (www.aafp.org; www.orthosupersite.com).
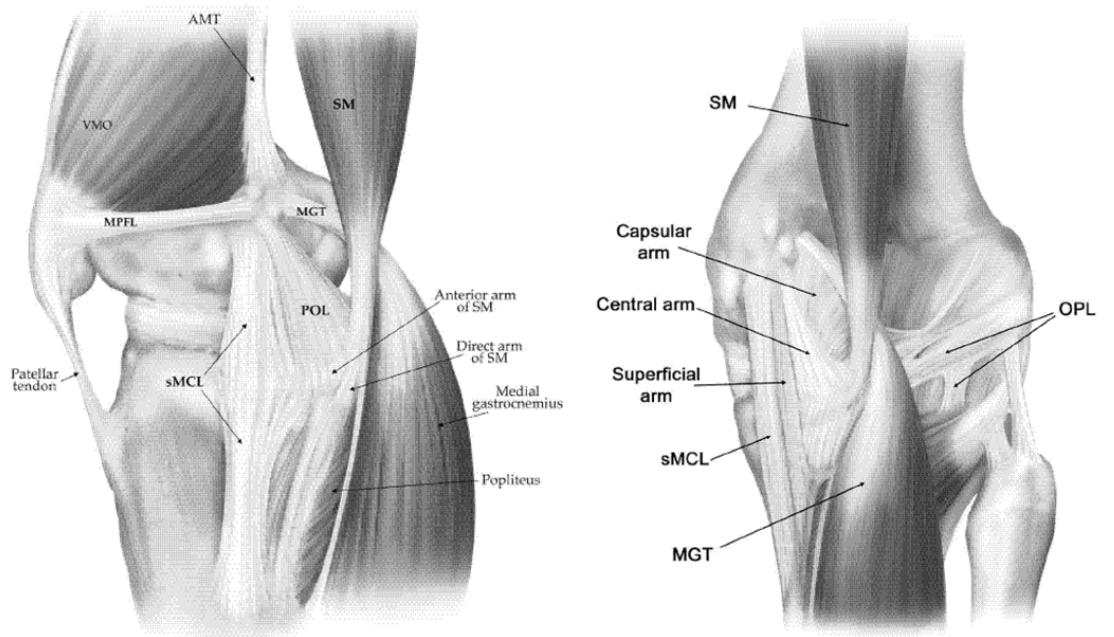
Figure 2.6 Diagram of the medial and posteromedial knee showing the superficial medial collateral (sMCL), oblique popliteal (OPL), and posterior oblique (POL) ligaments (LaPrade et al., 2007a; LaPrade et al., 2007b).
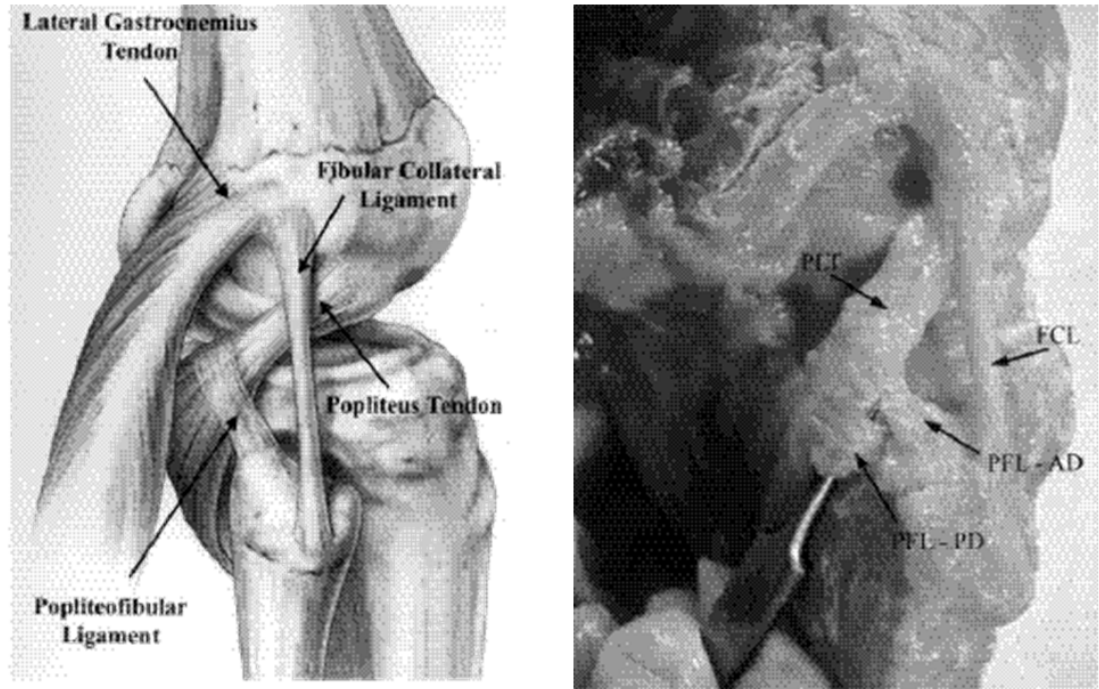
Figure 2.7 Diagram of the lateral knee showing the lateral (fibular) collateral (LCL) and popliteofibular (PFL) ligaments (LaPrade et al., 2003).
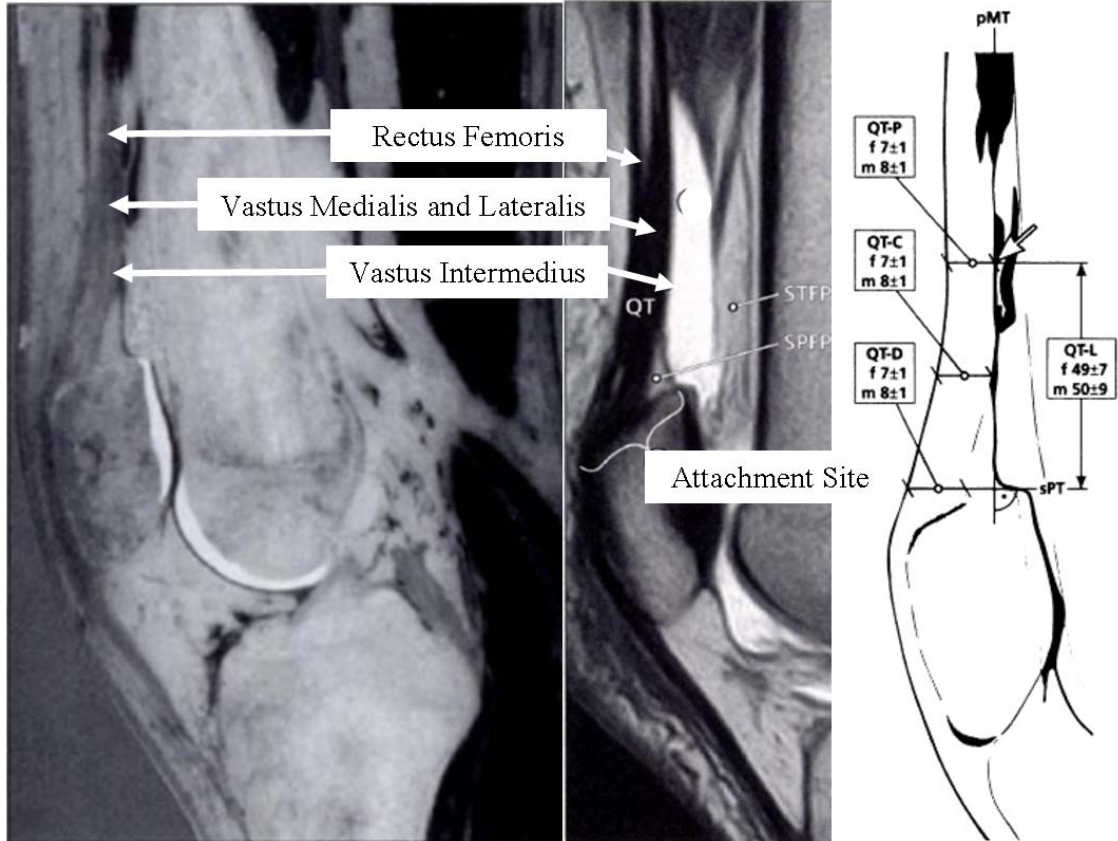
Figure 2.8 Sagittal dissection, magnetic resonance image, and diagram of quadriceps and patellar tendons (Staeubli et al., 1999).
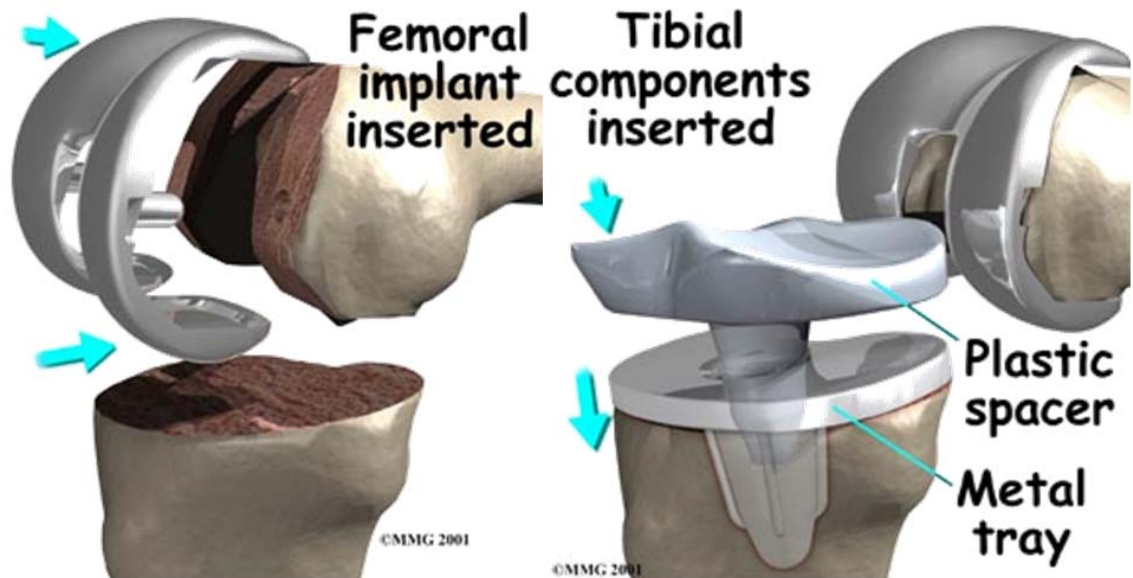
Figure 2.9 Diagram of a cruciate retaining total knee arthroplasty procedure (www.allaboutarthritis.com)

22

CHAPTER 3. MODELING OF KNEE LIGAMENTOUS CONSTRAINT

3.1. Introduction

Representing the complex geometry and mechanical function of ligaments is difficult to accomplish computationally due to their anisotropic, time- and history-dependent viscoelasticity, and hyperelastic, behavior. However, the level of complexity required is highly dependent on the research question at hand. A number of investigators have used non-linear, tension only springs to represent ligaments of the knee because of their ease of implementation and low computational cost (Li et al., 1999; Mesfar and Shirazi-Adl, 2008; Mommersteeg et al., 1996a; Shelburne et al., 2006; Wismans et al., 1980). While this type of representation is useful in studying varying aspects of joint function, it does not sufficiently capture the localized internal recruitment patterns and bony articulations that may be necessary to appropriately reproduce ligamentous constraint computationally.

More sophisticated constitutive models have been developed to represent more complex ligament mechanical behavior and elucidate internal stress-strain patterns (Limbert and Taylor, 2002; Ramaniraka et al., 2005; Weiss et al., 1996), but due to their increased computational cost and difficulty of implementation, there have been few attempts at applying these more accurate representations to whole joint evaluations (Pena et al., 2006). The following sections describe an alternative method for ligament representation within the explicit FE framework that can provide internal localized fiber

recruitment patterns and account for bony interactions (wrapping) at a reasonable computational cost. Specifically, the first section describes ligament structure and mechanical behavior as determined by experimental measurements, the second describes various methods of ligament representation and verification under linear tension, and the third describes a method for developing specimen-specific ligament constraint for the entire tibiofemoral joint using optimization and experimental laxity envelopes.

3.2. Ligament Structure and Mechanical Behavior

The skeletal ligaments are short bands of tough fibrous connective tissue that connect directly between bones to passively guide normal joint motion and limit excessive motion (Weiss, 1995). Ligaments are composed of an amorphous ground matrix, water, and multiple closely packed collagen fiber bundles oriented in a parallel fashion to provide joint stability (Woo et al., 2006). While collagen fibers may exhibit a more linear elastic response, ligament structures demonstrate a non-linear tensile load-elongation response with an upward concave toe region under low loads and a linear region under higher loads (Figure 3.1). The change in response has been attributed to uncrimping of the collagen fibers in the toe region and subsequent recruitment and elongation of fibers during the linear response.

3.3. Development of Anatomic, Efficient Ligament Representation

As described previously, ligament representations within a computational framework can take on many forms. To capture the mechanical behavior of the non-linear toe region, the subsequent linear region, and the lack of compressive stiffness, ligament force-displacement definitions are typically characterized by a piecewise function:

$$f = 0, \qquad\qquad\qquad \varepsilon < 0$$

$$f = 0.25k\, \varepsilon^2 / \varepsilon_l\,, \qquad 0 <= \varepsilon <= 2\, \varepsilon_l \qquad\qquad\qquad \text{Equation 3.1}$$

$$f = k(\varepsilon - \varepsilon_l), \qquad\quad \varepsilon > 2\, \varepsilon_l$$

where ε is the current strain value, ε_l is the level of ligament strain defining the toe region (typically 0.03), k is ligament stiffness and f is the resultant ligament force. Strain is defined as $\varepsilon = (l - l_0)/l_0$ where l is the current length and l_0 is the undeformed or zero-load ligament length (Blankevoort and Huiskes, 1996).

The above definition for ligament mechanical response was implemented in ABAQUS/Explicit as a parametric function and applied to several different computational ligament representations. Specifically, a simplified uni-axial pull model was developed to evaluate the force-deflection response of an LCL represented by a single point-to-point spring, 3 parallel point-to-point springs, a 3-bundle structure with parallel sets of springs in series (to include mid-side nodes for wrapping), and two- and three-dimensional (2D, 3D) fiber reinforced structures (Figure 3.2).   The fiber-

reinforced structures contained a low-modulus, hyperelastic material definition for the ground substance and sets of parallel springs embedded along the element edge lengths of the pull direction. The force-displacement behavior of the single spring representations was defined by a single spring stiffness or strain value and applied via Equation 3.1. Stiffness adjustment in the fiber-reinforced models was the same as the spring models, but modification of initial strain was implemented by rigidly attaching one border to a linear translator element and prescribing an initial translation. Using these methods, a suitable match to experimental uni-axial pull response (Sugita and Amis, 2001) was achieved for each representation (Figure 3.3).

The fiber-reinforced ligaments demonstrated equivalent accuracy to the simple point-to-point spring representation in the uni-axial pull models with the added benefit of providing more realistic anatomic dimensions, localized fiber recruitment information, and the ability to wrap over bony or implanted surfaces during simulated high flexion activities. The use of a low-modulus ground substance and the explicit FE method's material-based stability requirements was pivotal to achieving an anatomic representation at a relatively low computational cost. Based on the results with the LCL, additional uni-axial pull models were developed for each knee ligament structure with the 2D fiber-reinforced representation prior to implementation in whole joint knee models.

3.4. Modeling Specimen-Specific Ligamentous Constraint

Whole joint constraint is specimen-specific and dependent on ligament mechanical properties and anatomy. To properly represent specimen-specific

ligamentous constraint within the computational framework, it is essential to reproduce ligament attachments, dimensions, and mechanical responses for the primary load bearing structures crossing the joint and to verify the selected ligament representation can accurately reproduce localized recruitment patterns and constraint. Accomplishing this presents several technical challenges, which is why many computational knee studies commonly rely on literature-based ligament anatomy and mechanical definitions (Bendjaballah et al., 1997a; Mesfar and Shirazi-Adl, 2006a; Shelburne et al., 2006).

Few attempts have been made to compare knee model laxity response to experimental measurements. In their study of four cadaveric knee specimens, Blankevoort et al. demonstrated good agreement between specimen-specific 3D mathematical models and experimental internal-external (I-E) and anterior-posterior (A-P) laxity envelopes from 0 to 90° femoral flexion by optimizing ligament stiffness and strain values (Blankevoort and Huiskes, 1996). In a more recent study, Li et al. demonstrated a similar technique using manual optimization of ligament stiffness and strain values to match I-E and A-P laxity response at 0 and 30° femoral flexion on a single specimen-specific cadaver FE knee model (Li et al., 1999). Both studies found that including only a subset of the load-bearing ligament structures crossing the tibiofemoral joint likely influenced the final mechanical properties of the included ligaments, which could potentially be addressed by adding structures or a more anatomic representation. Nonetheless, they successfully demonstrated the ability to tune the ligament properties of a specimen-specific knee model to match experimental laxity envelopes.

27

Chapters 6 and 7 present computational studies in which fiber-reinforced representations of multiple patellofemoral and tibiofemoral ligament structures are tuned to reproduce specimen-specific constraint. In the previous section, it was demonstrated that the fiber-reinforced representation could be parametrically defined to reproduce experimental uni-axial force-displacement characteristics using literature values and dimensions. Chapter 6 presents a study in which pre-tensioning via translation of a ligament borders can be used to tune the patellofemoral ligaments to improve kinematic predictions in both the natural and implanted joint. Chapter 7 presents a method similar to the aforementioned ligament optimization studies applied to the tibiofemoral joint for kinematic whole joint predictions in four specimen-specific implanted cadaveric knees.
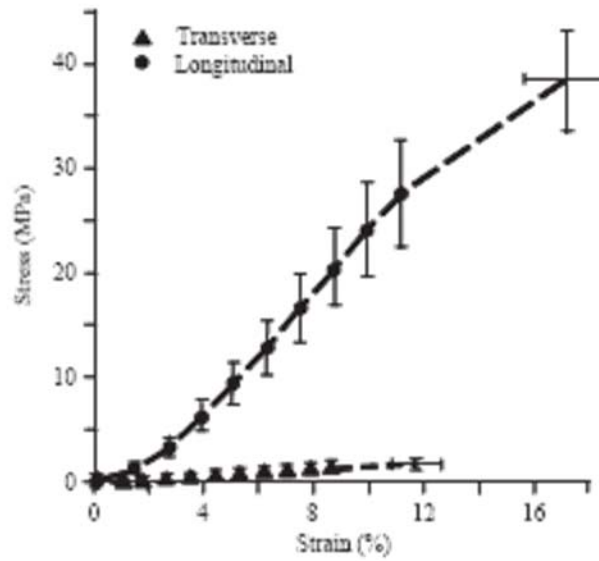
Figure 3.1 Representative ligament stress-strain curve along the longitudinal and transverse directions (Quapp and Weiss, 1998).

| 1 Spring,
point-to-point | 3 Springs,
point-to-point | 3 Bundles,
parallel springs
in series | 2-D Fiber
Reinforced | 3-D Fiber
Reinforced |
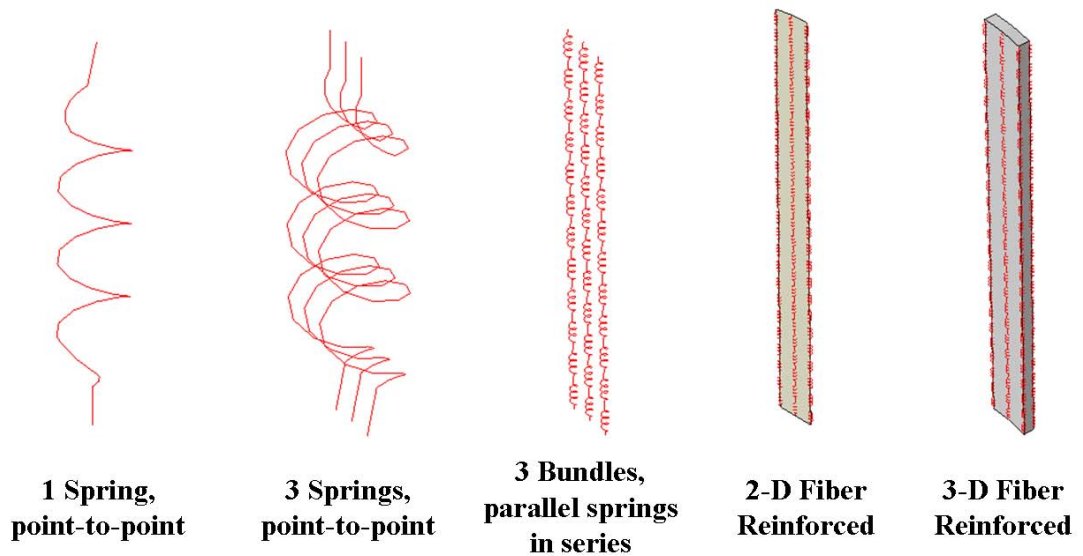
Figure 3.2 Various computational representations of the LCL for mechanical characterization in a uni-axial pull model.
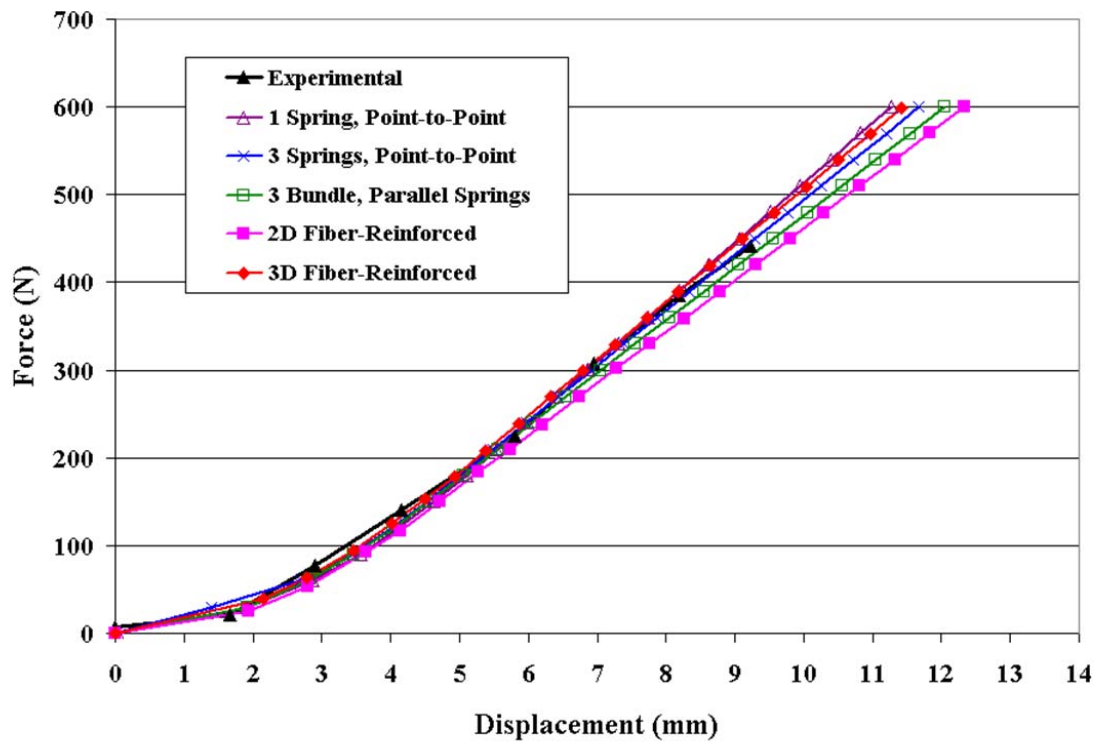
Figure 3.3 Uniaxial pull model force-displacement results for varous LCL
representations; Experimental curve from (Stäubli et al., 1999).

CHAPTER 4. A COMPUTATIONALLY EFFICIENT PROBABILISTIC KNEE LIGAMENT MODEL

4.1. Background and Motivation

The previous chapters described the fundamental aspects of knee anatomy and ligament modeling for assessing computational knee mechanics. This chapter presents an application of the computationally efficient 1D ligament representation combined with probabilistic techniques to elucidate the relationship between the inherent variability in ligament mechanical properties and attachment locations in predicting natural knee joint constraint.

4.2. Introduction

Computational representations of knee joint constraint are essential to forward dynamic (force or muscle driven) models and prediction of knee kinematics, contact mechanics and joint loading. Numerous three-dimensional (3D) computational tibiofemoral knee models have investigated the effects of ligamentous constraint on joint kinematics under applied loads (Bendjaballah et al., 1997b; Blankevoort and Huiskes, 1996; Caruntu and Hefzy, 2004; Li et al., 1999; Mommersteeg et al., 1996b), contact mechanics (Beillas et al., 2007; Bendjaballah and Shirazi-Adl, 1995; Pena, 2005; Ramaniraka et al., 2005), and ligament response (Moglo and Shirazi-Adl, 2003b; Mommersteeg et al., 1996a; Pena et al., 2005; Shirazi-Adl and Moglo, 2005). The

majority of these studies utilized patient-specific anatomic geometry generated from medical image data. In these studies, the complexity of the ligament representation ranged from a fully deformable continuum representation, e.g. (Gardiner and Weiss, 2003; Limbert and Middleton, 2006), to sets of non-linear springs, e.g. (Bendjaballah and Shirazi-Adl, 1995; Blankevoort and Huiskes, 1996; Li, et al., 1999; Shelburne and Pandy, 1997). In dynamic analysis applications, simplified ligament representations have effectively applied constraint with significant reductions in computation time.

Large variability has been reported in experimentally measured force-displacement and torque-rotation laxity curves and ligament mechanical properties. Gollehon et al. applied anterior-posterior (AP) and internal-external (IE) loads/torques of 125 N and 6 N*m to seventeen intact cadaveric specimens and noted standard deviations for displacements of up to 3.2 mm and 6.5° at full extension and 5.2 mm and 8° at 90° flexion (Gollehon et al., 1987). Similarly, Markolf et al. applied 200 N AP forces to 49 subjects at 0 and 90° flexion and 10 N*m IE torques to 20 subjects at 20° flexion *in-vivo* and found standard deviations of up to 2.7 mm and 12.1°, respectively (Markolf et al., 1984). Comparable levels of variability were also measured by Grood et al. (Grood et al., 1988) and Robinson et al. (Robinson et al., 2006).

Variability in ligament linear stiffness of more than 30% of the mean has been reported from controlled experimental characterization tests (Chandrashekar et al., 2006; Race and Amis, 1994 ; Robinson et al., 2005). Additionally, when identifying ligament attachment site locations from image data, there is uncertainty in defining attachment boundaries and differentiation between ligament and adjacent bony or other

anatomical structures. Uncertainty with standard deviations up to 12.2 mm has been reported for identifying, locating and digitizing anatomical landmarks (Della Croce et al., 1999). Due to the variability observed, the accepted methodology is to tune ligament mechanical properties (stiffness) and initial conditions (pretension) in order to replicate kinematic response for a single loading protocol or particular activity.

Recognizing the potential impact of uncertainty, Weiss et al. (Weiss et al., 2005) advocate performing sensitivity studies, especially when applying population averages to subject-specific models. Recent studies have investigated the effects of uncertainty in the ligament mechanical properties on the predicted knee joint constraint e.g. (Beillas et al., 2007; Mesfar and Shirazi-Adl, 2006a; Pena et al., 2005). Other experimental (Bylski-Austrow et al., 1990; Grood et al., 1989; Hefzy et al., 1989) and computational (Beillas et al., 2007) studies have shown that varying ligament attachment site locations by as little as 2 mm affected joint kinematics. Due to the expensive computational cost of exploring all combinations and levels of input parameter variations, constraint sensitivity predictions typically involved discrete changes in ligament input parameters (stiffness) and were focused on the cruciate ligaments under specific loading scenarios. Alternatively, a probabilistic approach can provide a more holistic evaluation by considering interaction effects between multiple sources of uncertainty. The approach represents all of the input parameters as distributions and predicts output distributions and bounds of performance while also identifying sensitivity factors indicating which input parameters were most important. Probabilistic methods have recently been applied to account for uncertainties present in orthopaedic applications e.g. (Easley et al., 2007; Pal et al., 2008). To address the typically high computational cost associated

with the commonly used Monte Carlo method, efficient methods, like the advanced mean value (AMV) method (Wu et al., 1990), have been applied successfully to evaluate variability in bone fracture risk (Laz et al., 2007), muscle moment arms (Pal et al., 2007), and implant wear (Pal et al., 2008).

Accordingly, the objectives of this study were to develop an efficient probabilistic representation of knee ligamentous constraint using the AMV probabilistic approach, and to compare the AMV representation with the gold standard Monte Carlo approach. With the probabilistic representation, the effects of inherent uncertainty in ligament stiffness, reference strain and attachment site locations on joint constraint were assessed. A subject-specific explicit finite element model of the knee with 8 major load bearing ligamentous structures crossing the tibiofemoral joint was constructed from imaging data and evaluated under a series of AP forces and IE torques at full extension and 90° flexion. The probabilistic framework enabled the prediction of the distribution and bounds of AP and IE laxity based on experimentally-measured levels of ligament variability and, through the importance factors, the identification of the most important parameters affecting the predicted bounds.

4.3. Methods

4.3.1. Deterministic Finite Element Model Development

A 3D explicit finite element model of a healthy, normal adult male knee was developed in Abaqus/Explicit 6.6-1 (Dassault Systemes, Providence, RI) from a series of sagittal magnetic resonance images (in-plane resolution of 0.66 mm/pixel; 512x512

pixels; 1.5 mm slice thickness). With the knee flexed to approximately 15° and unloaded, the visible bony and articular structures of the femur and tibia, the anterior and posterior cruciate ligaments (ACL, PCL) and medial and lateral collateral ligaments (MCL, LCL) were manually outlined and exported as 3D surface geometries using ScanIP (Simpleware, Exeter, UK). For computational efficiency, bones and articular surfaces were considered rigid and represented by triangular shell and eight-noded hexahedral elements, respectively. Frictionless contact between articular structures was defined by a literature-based pressure-overclosure relationship (Blankevoort and Huiskes, 1996).

Eight of the primary load-bearing soft tissue structures crossing the tibiofemoral joint were represented by nonlinear, tension-only spring elements (Figure 4.1) including: the ACL, PCL, LCL, MCL, popliteofibular (PFL) ligament, oblique popliteal ligament (OPL), and medial and lateral posterior capsule (PCAP) and meniscus (MEN). Attachment site areas for the cruciates and collaterals were determined from the interface between the extracted 3D ligament contours and bony surfaces, while placement of the PFL and OPL were determined from literature descriptions (LaPrade et al., 2003; LaPrade et al., 2007b; Maynard et al., 1996; Munshi et al., 2003). Cruciate attachment areas were subdivided into antero-medial (amACL) and postero-lateral (plACL) bundles of the ACL and postero-medial (pmPCL) and antero-lateral (alPCL) bundles of the PCL (Harner et al., 1999). Femoral and tibial cruciate bundle attachment areas were quartered to place four parallel springs in the centroid of each quadrant and orient them based on the extracted 3D ligament surfaces (Figure 4.1). The MCL was subdivided into two groups of parallel springs in series for bony contact, with one group

oriented in the inferior-superior direction to represent the superficial region (sMCL) and another oriented more obliquely to represent the posteromedial capsule (PMC) (Amis et al., 2003a; LaPrade et al., 2007a; Robinson et al., 2004; Wymenga et al., 2006). The medial and lateral PCAP structures were represented by seven parallel sets of springs in series evenly distributed around the femoral and tibial condylar articular geometry (Abdel-Rahman and Hefzy, 1998; Shelburne and Pandy, 1997) with node-element contact for wrapping. The LCL, PFL, and OPL were all represented by three parallel springs with no wrapping. A simplified representation of the medial and lateral menisci was adopted from Li et al. (Li et al., 1999) using two springs in series along the AP axis and one spring along the medial-lateral axis. Ligament mechanical properties (reference strain and linear stiffness) were adjusted to match reported experimental laxity profiles (Li et al., 2002) under tibial AP load and IE torque at full extension and 90° femoral flexion. Spring force-deflection characteristics were considered constant within ligament bundles and composed of a non-linear toe and linear region split at 0.06 strain (Abdel-Rahman and Hefzy, 1998; Blankevoort et al., 1991b; Li et al., 1999).

AP and IE translational and rotational laxity profiles were evaluated through a multi-step process. With all tibial degrees of freedom (DOF) fixed, the femur was allowed to find an equilibrium position under initial ligament strains and a nominal 50 N compressive load (settling) at the MR-based flexion angle of approximately 15°. The femur was then flexed to either 0° or 90° with all other femoral DOF unconstrained. Subsequently, laxity profiles were determined from AP loads up to 134 N and IE torques up to 10 N*m. Model comparison between computational and experimental

laxity values was performed by calculating an average root mean square error (RMSE) at discrete load points through the loading profile.

4.3.2. Probabilistic Methods

Probabilistic analyses were performed to incorporate the effects of uncertainty in the ligament mechanical properties and attachment site locations using custom scripting and Nessus probabilistic modeling software (SwRI, San Antonio, TX) (Easley et al., 2007; Laz, 2005; Pal et al., 2007). The probabilistic approach represents input variables as distributions and predicts an output distribution from which the likelihood of a specific level of performance can be determined. In this study, 36 normally distributed input variables were considered: ligament reference strain and linear stiffness for the amACL, plACL, pmPCL, alPCL, sMCL, PMC, LCL, PFL, PCAP, and OPL (20 inputs) and tibial and femoral ligament attachment locations for the cruciates and collateral ligaments along orthogonal axes (16 inputs) aligned to 2D anatomic planes matching respective bony geometries (Figure 4.2).

As a conservative estimate of initial ligament strain variability in the current study, a standard deviation of 0.02 was assumed for all ligaments, which at ± 2 standard deviations from the mean (5 and 95% probability levels) would represent a total of range of 0.08 in reference strain. Variability in linear stiffness has been shown to be up to 30% of the mean in controlled experimental studies (Chandrashekar et al., 2006; Race and Amis, 1994 ; Robinson et al., 2005), which was adopted for each ligament's linear stiffness variability in the current study. Force-deflection curves were parametrically defined so that a change in reference strain shifted the curve along the

deflection axis and a change in stiffness changed the slope in the linear region. While affected by the method used for identification (e.g. medical images or direct subject digitization), uncertainty in the location of ligament attachment areas is primarily dependent on the identification of an area or landmark. Intra-evaluator standard deviations ranging from 1.4 mm to 12.2 mm have been reported for locating anatomical landmarks on the femur (Della Croce et al., 1999). In the current study, a 1 mm standard deviation level was adopted for cruciate and collateral ligament tibial and femoral attachment sites.

Probabilistic analyses were performed with the efficient AMV and gold standard Monte Carlo methods. The AMV method is an optimization-based method utilizing a mean value approximation augmented with higher-order terms to determine the response at a specified probability level (Wu et al., 1990). With well-behaved monotonic systems, the AMV method requires only the deterministic trial, one trial to perturb each input variable (36 in this study), and one trial to determine output at specified probability levels. The Monte Carlo method uses repeated trials performed with input values randomly generated according to their distributions to predict a distribution of output. As the accuracy of the Monte Carlo method is dependent on the number of trials, the analysis with 200 trials was used for benchmarking purposes. Both probabilistic analysis methods were used to predict distributions of AP and IE laxity, reported as bounds at the 5 and 95% probability levels; importance factors for a relative ranking of the influence of input parameter variability on output measures were calculated with the AMV method.

4.4. Results

Following the manual optimization, the laxity profiles from the computational knee model agreed closely with published experimental data (Li et al., 2002) over the range of load application (experimental and mean predicted curves in Figure 4.3 and Figure 4.5). Average translational and rotational RMSE values were 0.51 mm and 1.87° at 0° femoral flexion and 0.70 mm and 1.89° at 90° flexion, respectively. The optimized values of stiffness and reference strain were all within the ranges of values reported in the literature. The combination of non-linear spring elements for ligament representation and rigid material definitions for bony and articular surfaces resulted in model run times of less than five minutes for generation of a single laxity curve (e.g. anterior translation at 0° flexion).

The probabilistic analyses predicted the distribution of AP and IE laxity, shown as the 5 and 95% laxity bounds with the Monte Carlo and AMV probabilistic methods (Figure 4.3 and Figure 4.5). Comparing the two methods, average translational and rotational RMSE values over the range of loading were less than 0.3 mm and 1.3°, respectively. Predicting the laxity bounds for a single loading scenario at one flexion angle required less than 50 trials with AMV (approximately 4 hours) with differences between the methods smaller than the sampling errors associated with the 200-trial Monte Carlo method.

From the probabilistic analyses, the predicted variability in AP laxity was greater at 90° flexion than full extension. To illustrate the variability in constraint present, predicted 5-95% laxity bounds under 134 N applied loads at full extension and

90° flexion for anterior tibial translation (ATT) were 2.1 mm and 4.4 mm while bounds for posterior tibial translation (PTT) were 4.7 mm and 5.5 mm, respectively (Figure 4.4). Qualitatively, ATT at full extension recruited the PCAP, plACL and posterior portion of the sMCL while PTT was restricted by the PCAP, pmPCL, LCL and sMCL. From the probabilistic analyses, ATT was found to be most influenced by plACL strain and to a lesser extent stiffness, sMCL strain, and femoral ACL attachment in both the IS and AP directions (Figure 4). PTT at full extension was influenced mostly by PCAP and pmPCL strains and somewhat by their stiffness. At 90° flexion, ATT recruited the amACL and pmPCL with PTT primarily restricted by both bundles of the PCL. ATT was most influenced by ACL AP and PCL IS attachment site perturbations followed by amACL and pmPCL strain and stiffness (not shown); PTT was most influenced by PCL femoral IS and to a lesser degree AP attachment perturbations and pmPCL strain and stiffness (Figure 4.4).

The variability predicted for IE laxity was fairly consistent through the range of applied torques at both full extension and 90° flexion. Predicted 5-95% laxity bounds under 10 N*m applied torques at full extension and 90° flexion for internal tibial rotation (ITR) were 7.0 and 9.6° while external tibial rotation (ETR) bounds were 9.6 and 9.2°, respectively (Figure 4.5). At full extension, the primary restraints to ITR were the PMC, PCAP, plACL and sMCL whereas ETR was restrained by the PCAP, OPL, LCL, and sMCL. From the probabilistic analyses with the knee at full extension, ITR was found to be largely influenced by PMC strain and to a lesser degree plACL strain and PMC stiffness while ETR was most influenced by LCL and PCAP strain and stiffness (Figure 4.6). At 90° flexion, ITR recruited the PMC, amACL, and the pmPCL

whereas ETR was restrained by the pmPCL, sMCL, and PFL. ITR was most influenced by PMC strain and stiffness, PCL femoral IS and ACL femoral AP attachment perturbations, and amACL and pmPCL strains (not shown) while ETR was most influenced by sMCL strain, stiffness and AP tibial and femoral attachments and to a lesser degree PFL stiffness and strain (not shown) (Figure 4.6).

4.5. Discussion

The soft tissue constraint controlling knee mechanics is a combination of complex interactions between multiple ligaments and other structures (e.g. meniscus, posterior capsule). As in other studies (Beillas et al., 2007; Blankevoort and Huiskes, 1996; Li et al., 1999; Mesfar and Shirazi-Adl, 2006a; Shelburne and Pandy, 1997), the current study represented ligament bundles as nonlinear, tension-only springs, but included more bundles than prior representations and incorporated wrapping for the MCL and posterior capsule. The current model exhibited ligament recruitment patterns and a screw-home response comparable to those found experimentally (Blankevoort et al., 1988; Fukubayashi et al., 1982; Gollehon et al., 1987; Grood et al., 1988) and computationally (Blankevoort et al., 1991a; Moglo and Shirazi-Adl, 2003a; Mommersteeg et al., 1996a; Mommersteeg et al., 1997; Mommersteeg et al., 1996b). Notably, the efficiency of the model representation, while reproducing constraint, is beneficial in making forward dynamic assessments and enabling probabilistic evaluation. An additional benefit of the explicit finite element platform compared to rigid body analyses is that in forward dynamic assessments, specific structures (e.g.

articular cartilage) can be modeled as deformable, allowing internal stresses and strains to be evaluated.

Uncertainties have been presented for ligament properties and experimentally measured laxity profiles from multiple subjects. The current study has utilized one subject-specific geometry with the superposition of uncertainty in stiffness, reference strain and attachment site location. Based on the large variability predicted, 5-95 percentile bounds of up to 5.5 mm of AP translation and 9.6° of IE rotation under 134 N loads and 10 N*m torques, the differences in constraint will likely impact the resulting outputs of forward-driven models. The variability in constraint characterized underscores the importance of considering the effects of uncertainty on predicted joint loading and TKR evaluation. To better predict the variability for a population, the model would need to account for geometric subject to subject differences, not only the ligament property and model development uncertainty included here.

The current study represents a novel application of probabilistic analysis to soft tissue constraint in the knee. The model predicted the distribution of AP and IE laxity response curves and presented them as 5 and 95 percentile bounds (Figure 4.3 and Figure 4.5). The efficient AMV method predicted laxity results that were in close agreement to the Monte Carlo method with a substantial four-fold reduction in computational time. Importance factors from the AMV probabilistic analysis also provided a relative ranking of the influence of ligament mechanical property and attachment site variability on knee joint response under a range of applied AP and IE loads at two distinct flexion angles. Importance factors can be influenced by the

selected levels of input variability; in this study, input variability levels were based on available experimental data and kept uniform for each variable type in order to provide relative rankings of importance between input parameters.

The importance factors and ligament recruitment reported in other biomechanical studies agreed well under a variety of loading and flexion positions. At full extension, it is generally accepted that the ACL restricts anterior tibial motion (Butler et al., 1980; Fukubayashi et al., 1982; Girgis et al., 1975; Markolf et al., 1976; Piziali et al., 1980) and that the posterolateral bundle (plACL) is the more loaded of the two functional ACL bundles (Bach et al., 1997; Caruntu and Hefzy, 2004; Mommersteeg et al., 1997; Sakane et al., 1997; Shelburne and Pandy, 1997; Song et al., 2004). In agreement with the current study, the importance factors indicated that ATT was most affected by plACL reference strain, stiffness, and femoral attachment locations in both the inferior-superior (IS) and AP directions and sMCL strain (Figure 4.4); all other parameters were found to be of lesser significance with importance factors less than 0.1. The relative importance of reference strain over the other parameters was found in several of the sensitivity results. Alternatively, ligament stiffness and attachment site variability affected laxity during load application due to changes in recruitment. Hefzy et al. noted changes in tibiofemoral distance and ligament recruitment during flexion when moving the ACL femoral attachment site, especially in the AP direction (Hefzy et al., 1989).

There is less agreement on the primary restraints to posterior laxity at full extension as the presence of coupled external rotations under posterior loads may

43

require contributions from other capsular structures or the collateral ligaments (Amis et al., 2003a; Blankevoort et al., 1991a; Gollehon et al., 1987; Grood et al., 1988; Park et al., 2004). The relative importance of pmPCL and PCAP stiffness and strain was related to the combination of external tibial rotation and applied AP loads. Similar to ATT results at full extension, PTT importance factors not presented in Figure 4.4 were all below 0.15.

As the femur flexes to 90°, it is generally accepted that both bundles of the PCL provide some amount of constraint with recruitment switching from the pmPCL in early flexion to the alPCL in later flexion (Harner et al., 1995). Although this pattern of recruitment is fairly well accepted, the relative importance of mechanical and attachment site parameters was more complex (Figure 4.4). PCL femoral attachment variability in the IS direction substantially affected ligament recruitment during flexion and loading at 90°. The importance of PCL attachment in ATT and PTT was in agreement with an in-vitro study by Grood et al. who found that changing PCL femoral attachment locations perpendicular to the tibial attachment orientation (i.e. in the IS direction) had the greatest impact on ligament lengthening (Grood et al., 1989). Likewise, perturbations in the ACL AP femoral attachment location (perpendicular to the tibial plateau at 90° flexion) were found to be important as the tibia internally rotated under anterior loads, recruiting the amACL bundle. The importance of the ACL femoral attachment location in the AP direction on ATT was supported by a study by Bylski-Austrow et al., which determined the largest difference in ACL tension over the range of flexion occurred with differences in AP position (Bylski-Austrow et al., 1990). The importance of pmPCL strain and stiffness to PTT at 90° flexion was largely due to

their improved orientation to resist AP forces (Race and Amis, 1996). All importance factors not presented in Figure 4.4 were less than 0.15 for both ATT and PTT at 90° flexion.

The relative importance of cruciate mechanical properties and femoral attachment locations to AP laxity has particular significance in relation to ligament reconstruction procedures. Previous studies have investigated the effects of ligament tensioning, positioning, and graft stiffness on recruitment and load carried by the structure (Bradley et al., 1988; Bylski-Austrow et al., 1990; Grood et al., 1989; Hefzy et al., 1989; Suggs et al., 2003), but did not elucidate the relative importance of each factor on AP laxity that may be useful in surgical decision making. For example, the current importance factors would suggest that restoring the mechanical function of the plACL bundle and the femoral AP position are more important to ATT at full extension than other parameters. Likewise, focusing attention on the pmPCL bundle and its femoral attachment would be more important to PTT at both 0 and 90° flexion. Additionally, the current probabilistic approach could be useful in predicting the magnitude of change in AP laxity (via 5-95% bounds per Figure 4.3) as a predictor of outcome after ligament reconstructive surgery.

Compared to AP forces, there is less agreement in the literature on the major ligamentous contributors to tibiofemoral constraint under applied IE torques. At full extension, it has been demonstrated previously that the plACL bundle and posteromedial capsular structures are primary restraints to internal rotation, while the LCL and posterolateral structures are the primary restraints to external rotation (Amis et

45

al., 2003a; Blankevoort et al., 1991a; Gollehon et al., 1987; Markolf et al., 1976; Robinson et al., 2006). Similar patterns were observed in the current study with rotational laxity most influenced by strain and stiffness of the obliquely-oriented structures of the PMC during internal rotation and the LCL during external rotation (Figure 4.6). Strain and stiffness of the plACL (internal) was also found to be important to rotary laxity, but to a much lesser extent; all other sensitivity factors at full extension were below 0.15. At 90° flexion, the PMC was well aligned to resist tibial internal rotation, as evidenced by the importance of its mechanical properties, but the importance of the ACL and PCL femoral attachment perturbations in AP and IS, respectively, were present due to their impact on final settled position. ETR was largely affected by sMCL mechanical properties and tibial and femoral attachment perturbations in the AP direction (Figure 4.6). In both internal and external rotations at 90° flexion, all other sensitivity factors were below 0.15.

In closing, a probabilistic representation of constraint has been developed with an emphasis on efficiency of the ligament structures and probabilistic method for use in forward driven assessments of joint mechanics and TKR designs. Sensitivity factors provided insight into the parameters (stiffness, reference strain, attachment site) of the ligaments that most affected laxity under various loading conditions and flexion angles. The efficient probabilistic representation developed can be used to represent uncertainty for a subject-specific model or, alternatively, may represent the variability present in a population of subjects.

46
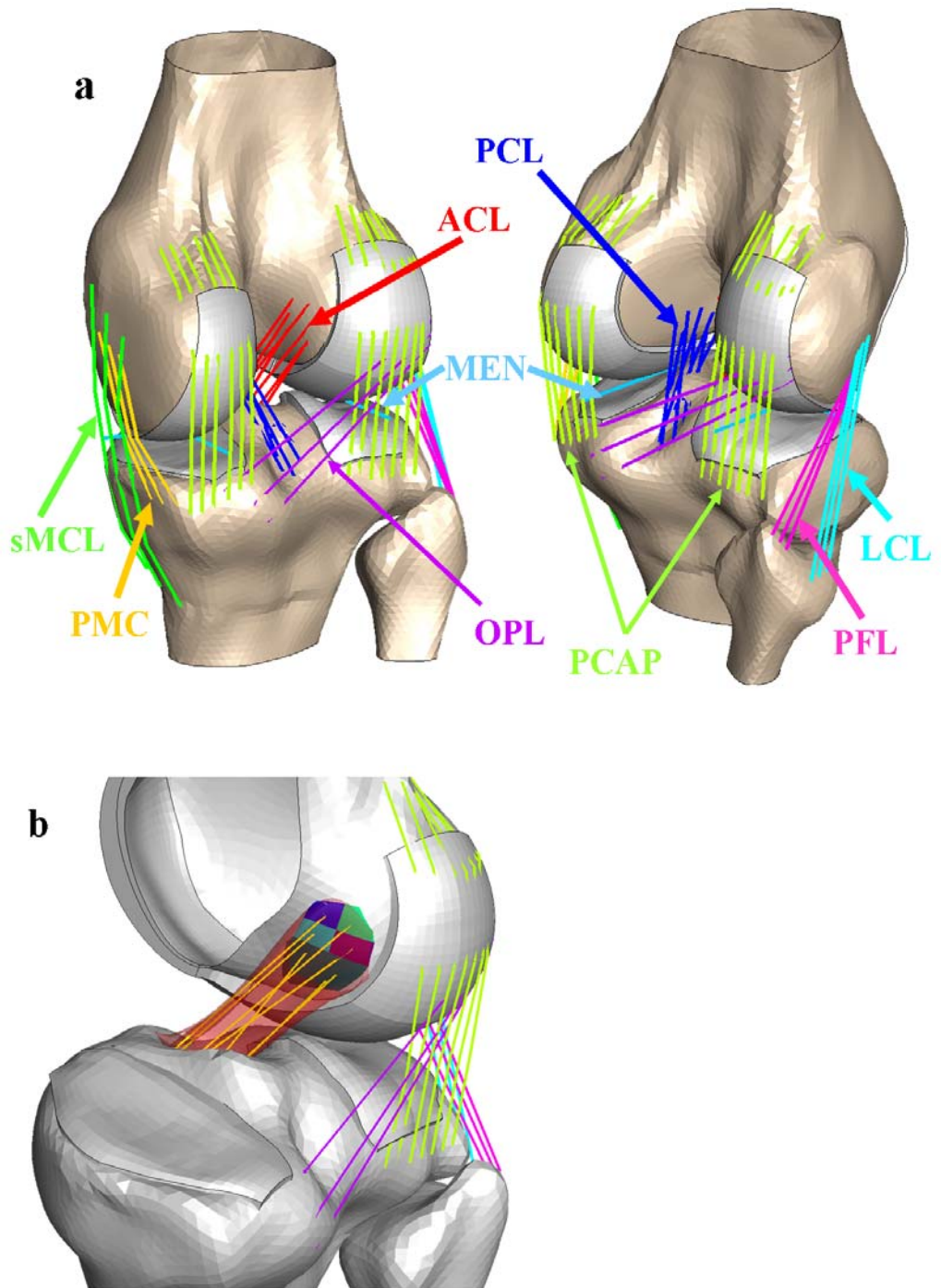
Figure 4.1 (a) Tibiofemoral model indicating soft tissue structures (b) 3D contour of segmented ACL (transparent) with quartered femoral attachment sites and springs representing the ACL bundles.
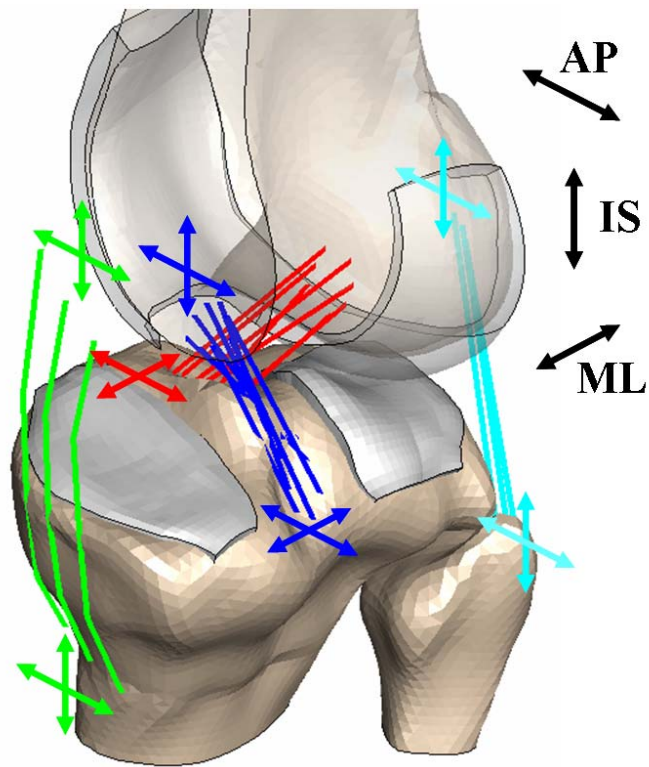
Figure 4.2 Ligament attachment site perturbations along anterior-posterior (AP),
inferior-superior (IS), and medial-lateral (ML) planes.
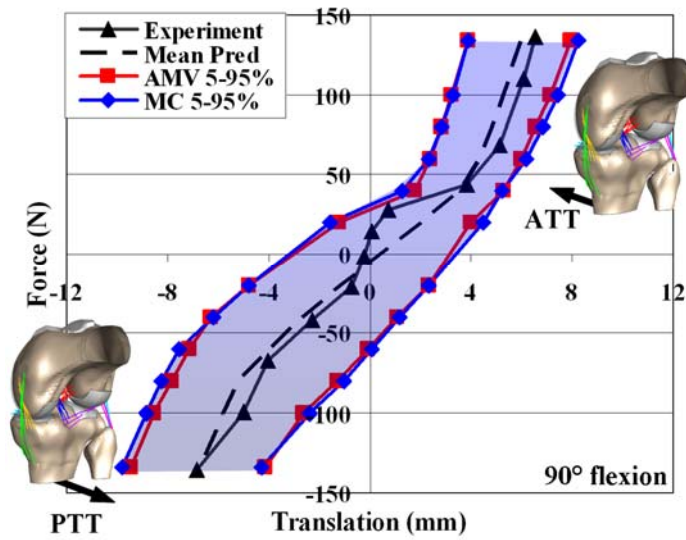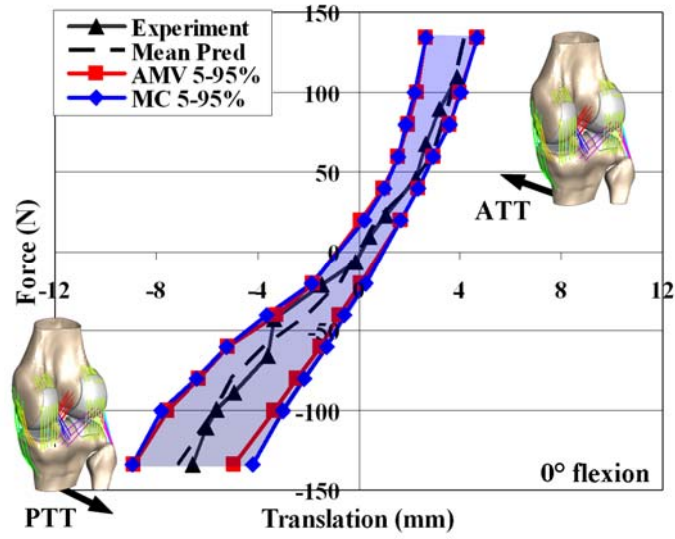
Figure 4.3 Experimental (Li et al., 2002), mean predicted and Monte Carlo (MC) and AMV bounds (5 & 95%) for AP laxity at 0° and 90° flexion. ATT and PTT refer to anterior and posterior tibial translation.
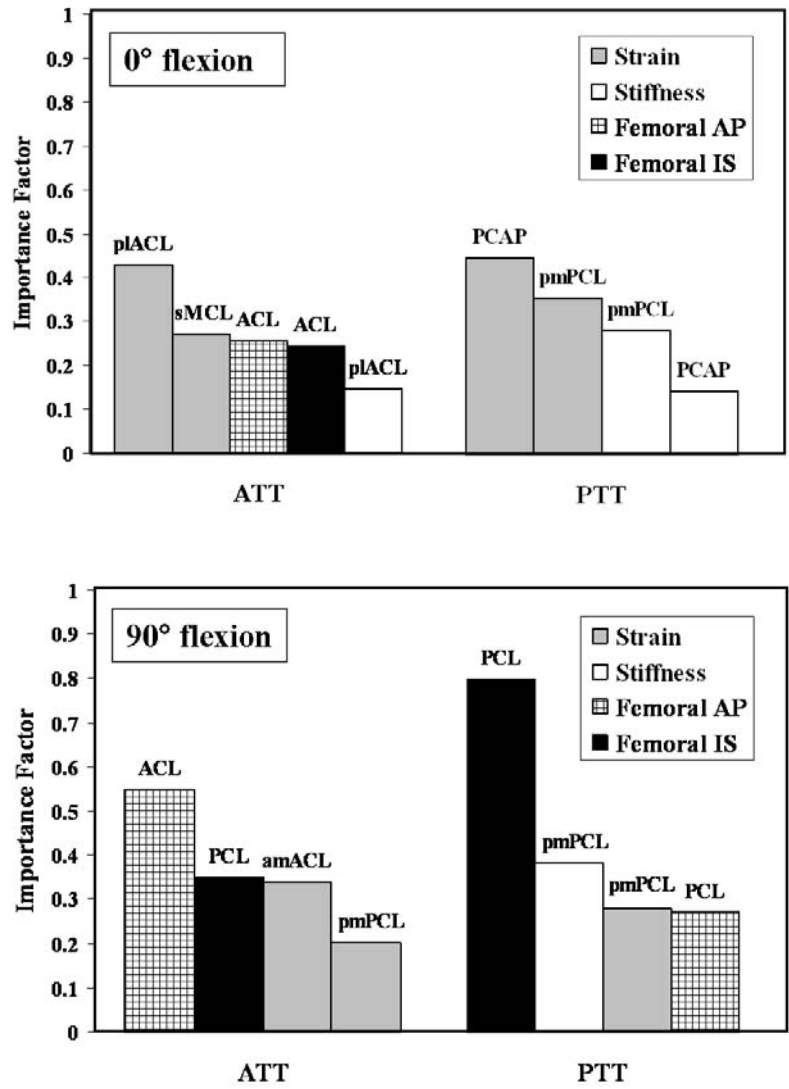
Figure 4.4 Highest ranking importance factors for AP laxity at 0 and 90° flexion.
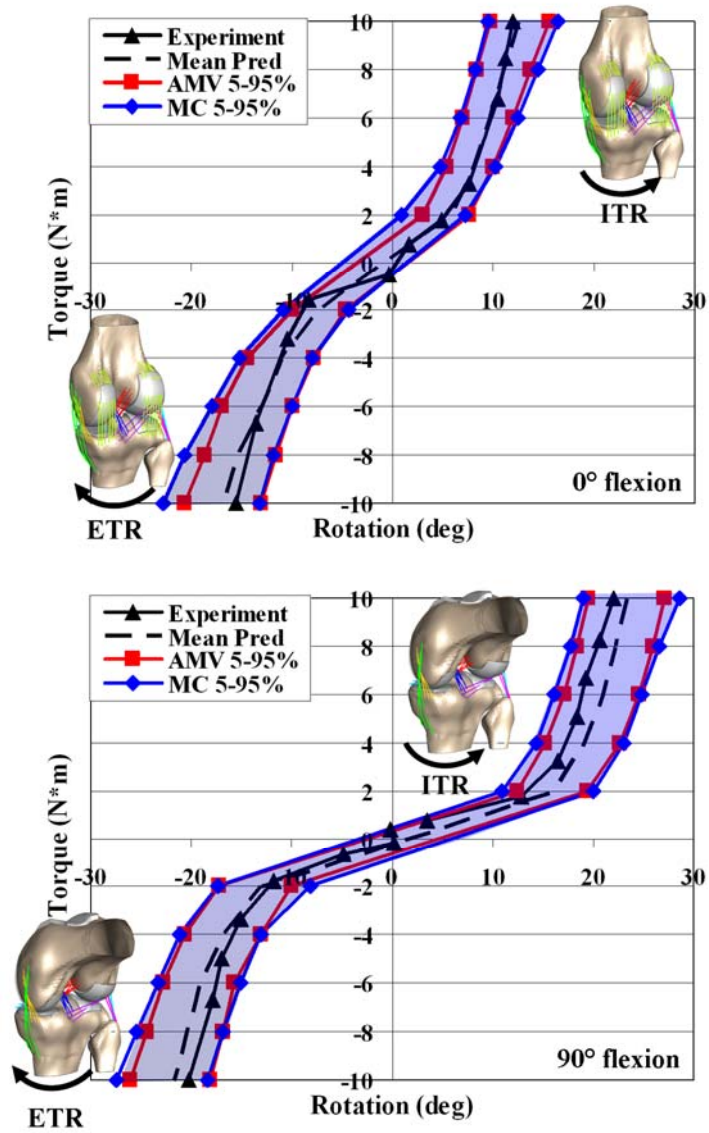
Figure 4.5 Experimental (Li et al., 2002), mean predicted and Monte Carlo (MC) and AMV bounds (5 & 95%) for IE laxity at 0° and 90° flexion. ITR and ETR refer to internal and external tibial rotation.
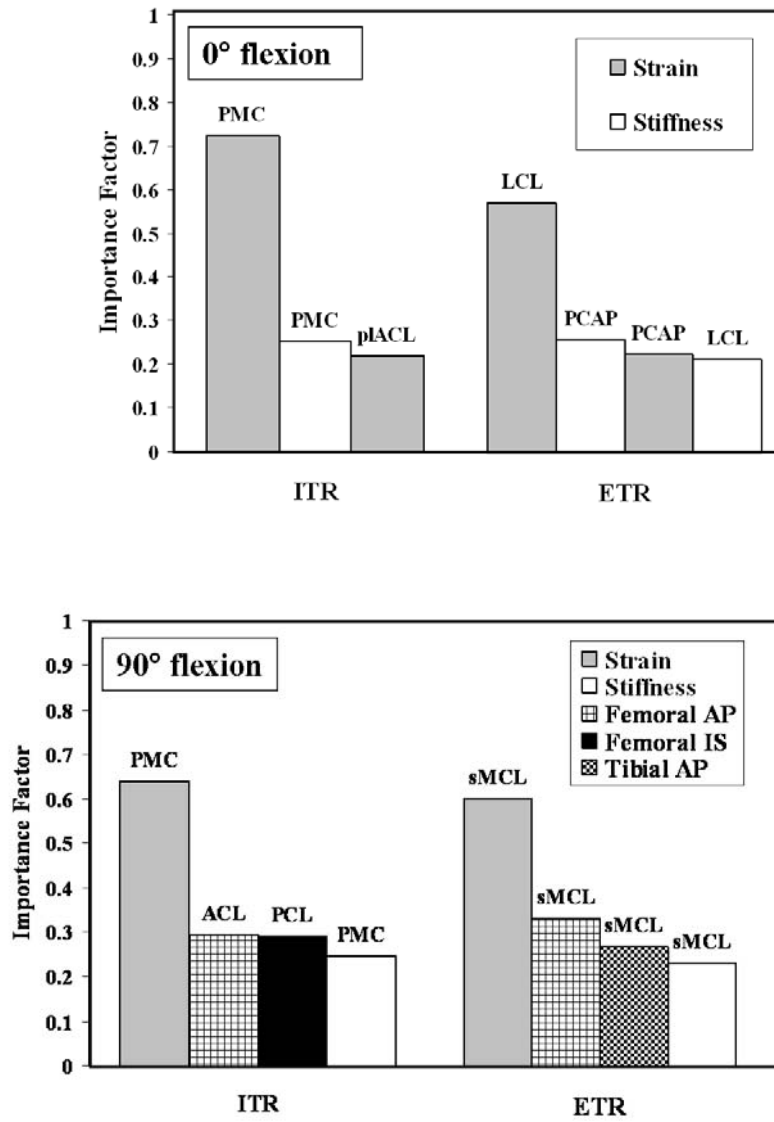
Figure 4.6 Highest ranking importance factors for IE laxity at 0 and 90° flexion.

CHAPTER 5. INFLUENCE OF ALIGNMENT PARAMETERS ON

PATELLOFEMORAL MECHANICS FOR ANATOMICAL AND DOMED

IMPLANTS

5.1. Background and Motivation

The following study applied the Monte Carlo probabilistic technique described in the previous chapter to clinically-relevant complications associated with the implanted patellofemoral joint. This study represents an example of how computational methods can be used to better understand the relationship between surgical component alignment variability and post-TKA knee mechanics as an indicator for long-term implant performance.

5.2. Introduction

Complications of the implanted patellofemoral (PF) joint, such as fracture, loosening, wear, and instability, are among the most common causes of total knee arthroplasty (TKA) failure (Brick and Scott, 1988; Meding et al., 2008) and may be attributable to malalignment of the patellar and femoral components (Anglin et al., 2008; Baldini et al., 2006; Chu et al., 2006; Kessler et al., 2008; Meding et al., 2008; Pagnano and Trousdale, 2000). Long-term TKA success may therefore benefit from an improved understanding of the affect of interoperative patellar and femoral component alignment parameters on clinically relevant outputs (i.e. tracking or internal stresses).

During TKA surgery, patellar resection is frequently accomplished through basic freehand cutting or with the aid of a patellar clamp in order to obtain a consistent thickness of remaining bone. The patellar component is subsequently aligned to optimize coverage or placed medially or superiorly depending on surgical philosophy. To improve the consistency of patellar alignment and soft-tissue balancing through advanced surgical instrumentation, the critical translational and rotational alignment parameters need to be identified, and these are likely design-specific.

Several experimental studies have investigated the influence of component alignment parameters (Anglin et al., 2008; Chu et al., 2006; Lee et al., 1999; Yoshii et al., 1992) on PF mechanics after TKA. Lee et al. demonstrated the influence of patellar medial-lateral (M-L) and inferior-superior (I-S) positioning on contact mechanics with a domed patellar component under quasi-static loads for five implanted cadaveric specimens (Lee et al., 1999). More recently, an *in-vitro* study of eight implanted cadaver specimens simulating a squat activity in a mechanical simulator was conducted by Anglin et al. to rank the relative importance of femoral internal-external (I-E) rotation, patellar resection angle, and patellar component M-L position on patellar tilt and shift at low (15°) and deep (90°) flexion angles (Anglin et al., 2008).

Computational models represent an efficient method for investigating component alignment effects on clinical output measures related to long term TKA survival. The finite element (FE) method is well suited for conducting PF investigations through the use of deformable component and soft tissue structures to predict internal component stresses and contact mechanics measurements that would

54

otherwise be difficult or impossible to obtain experimentally. Several computational studies have demonstrated the influence of femoral and patellar component placement (D'Lima et al., 2003; Heegaard et al., 2001; Kessler et al., 2008) and quadriceps load distribution (Dhaher and Kahn, 2002; Elias et al., 2006) on predicted kinematics and contact forces, but to our knowledge no study has attempted to investigate the effect of surgical alignment parameters and quadriceps load distribution on PF mechanics under simulated dynamic loading.

Accordingly, the objectives of the present study were to utilize an implanted probabilistic FE model to determine the most important surgical alignment parameters affecting PF mechanics and to compare the amount of predicted output variability between anatomic and domed patellar component designs. Specifically, patellar component I-S and M-L position, M-L tilt, flexion-extension (F-E), and M-L rotation, femoral I-E position, and percent vastus medialis oblique (VMO) load contribution were treated as distributed input variables to determine their relative importance on predicted PF kinematics, contact pressures, areas and forces, and internal von Mises stresses during a simulated deep knee bend activity. The current probabilistic framework provided a direct comparison of design robustness to surgical malalignment, statistical comparisons, and a relative ranking of the importance of alignment and load input parameters on predicted outcomes for the two designs.

5.3. Materials and Methods

5.3.1. Deterministic Patellofemoral Model Development

A three-dimensional (3D) FE model of an implanted knee joint was constructed for dynamic analysis in Abaqus/Explicit™ 6.7-1 (Dassault Systemes, Providence, RI). Femoral, tibial, and patellar bony surfaces of a healthy normal subject were extracted via segmentation from magnetic resonance imaging data using ScanIP (Simpleware, Exeter, UK) and surface meshed with triangular elements using Hypermesh 9.0 (Altair Inc., Troy, MI). Size-matched fixed-bearing cruciate-retaining domed and anatomic femoral and patellar components were imported from CAD surfaces and aligned to the bony geometry under the direction of an orthopedic surgeon (Figure 5.1). Femoral components were meshed with two-dimensional (2D) triangular elements; patellar components were solid meshed with three layers of 8-noded hexahedral elements (~1.5 mm element edge length). To eliminate potential effects of tibial insert design on PF tracking, a meshed flat surface was placed on the proximal end of the tibial bone and aligned to the femoral components in the frontal and transverse planes and perpendicular to the mechanical axis of the tibia in the sagittal plane. In the analyses, bones and the femoral components were assumed rigid; patellar components were defined by a linearly elastic, isotropic deformable material (E=572 MPa, v=0.45) to represent UHMWPE. Contact between the patellar and femoral components was defined using a penalty-based method with a weight factor and friction coefficient of 0.04 (Halloran et al., 2005c).

56

The patellar ligament (PL), rectus femoris (RF), and vasti soft tissue structures of the extensor mechanism were represented for load transfer across the PF joint. Each structure consisted of deformable hyperelastic 2D membrane elements, with uni-axial tension characteristics matching literature values (Stäubli et al., 1999). The vasti mesh was rigidly fixed to the medial, superior, and lateral borders of the patellar bone with the proximal ends split into five sections representing the lateralis longus (VLL), lateralis obliquus (VLO), intermedius (VI), medialis longus (VML), and medialis obliquus (VMO) (Figure 5.2). Linear actuators representing the quadriceps muscles were attached to the proximal portions of the vasti and rectus femoris tendons to distribute a resultant quadriceps load across the actuators according to physiological cross-sectional area (RF=15%, VI=20%, VLL=35%, VLO=10%, VML=15%, VMO=10%) and orientations described in the literature (Farahmand et al., 1998). The distal and proximal portions of the PL were rigidly fixed to the tibial tubercle and anterior-inferior border of the patella while the RF passed over the anterior face of the patella bone inserting just proximal to the PL. Tendon contact was defined between the extensor mechanism structures and bony or implanted surfaces to allow wrapping in deeper flexion.

A ramped quadriceps load (up to 2000 N) and fluoroscopy-based tibiofemoral (TF) kinematics were prescribed to evaluate isolated PF joint mechanics during a simulated deep squat activity. Model TF kinematics were based on previously extracted fluoroscopic motion of a CR-implanted patient performing a deep squat. Tibial internal rotation and femoral anterior-posterior translation was prescribed as the femur was flexed from 0 to 120° under a 720 N compressive load applied across the TF joint.

Patellar six degree-of-freedom kinematics were described as patellar tilt, shift, and rotation with respect to the femur using a three-cylindrical open-chain description of motion (Grood and Suntay, 1983) whereas patellar flexion was calculated with respect to the tibial long axis (Komistek et al., 2000). Specifically, a lateral patellar tilt about the local patellar I-S axis would cause the floating A-P axis to point more laterally, a lateral patellar rotation about the floating patellar A-P axis would cause the distal pole of the patella to point more laterally, and a lateral shift would translate the patella laterally (Figure 5.2).

5.3.2. Probabilistic Methods

Monte Carlo (MC) probabilistic analyses were performed using Nessus probabilistic modeling software (SwRI, San Antonio, TX) to investigate the effects of patellar and femoral component alignment and quadriceps load distribution on predicted PF kinematics and contact mechanics for both implant designs. Patellar component alignment was perturbed by translations along local medial-lateral (Pat M-L) and inferior-superior (Pat I-S) axes (1 standard deviation (SD) = 1 mm), flexion-extension about the patellar M-L axis (Pat F-E), M-L tilt about the patellar I-S axis (Pat Tilt), and rotation about the anterior-posterior axis (Pat Rot). Standard deviations of 3.3° were used for flexion and tilt and 5.0° for rotation. Perturbations in femoral component internal-external (Fem I-E) alignment (1 SD = 1.6°) and contribution of the vastus medialis obliquus (VMO Cont) within the quadriceps load distribution (1 SD = 3.3% of total quadriceps load) were also investigated (Figure 5.3). All input variables were considered normally distributed.

Ten output parameters were evaluated over 100 MC trials for each implant type, including patellar flexion, M-L tilt, shift, and rotation, M-L forces due to contact, peak von Mises stresses, contact areas and peak contact pressures. Model-predicted output bounds at the 5 to 95% confidence levels were determined for each output parameter throughout the range of femoral flexion. Statistical comparisons were made between the two designs at 10° intervals between 0 and 120° femoral flexion for all output parameters using a two-sample Student's t-test with unequal variance. To determine the sensitivity between input and output parameters, correlation coefficients were calculated from the MC analysis and averaged over the entire flexion cycle. To provide an understanding of the relationship between input and output parameters, slopes were calculated at 90° flexion for each variable.

5.4. Results

Variability in M-L tilt, shift, and rotation with the anatomic design was lesser than the domed in early flexion (< 30º) and greater throughout the rest of the range of femoral flexion; bounds for patellar flexion were more consistent throughout the range of flexion for both designs (Figure 5.4). Statistically significant differences ($p < 0.01$) were found throughout the range of femoral flexion for patellar flexion and rotation; patellar shift was only significantly different under 30º of flexion while tilt was significantly different in early (< 30º) and late (> 80º) femoral flexion (not shown).

Statistically significant differences between domed and anatomic contact areas were found throughout the range of flexion with consistently greater contact area and variability (5 to 95% bounds) with the anatomic design (Figure 5.5). Peak contact

pressure and internal von Mises stress followed similar patterns through the range of flexion for both designs. The anatomic component showed higher initial pressure and stress in early flexion (under 10º) followed by a substantial reduction in early to mid flexion (10 to 40º) and a steady increase beyond 40º flexion whereas the domed pressure and stress magnitudes remained fairly constant up to 60º flexion and steadily increased through deeper flexion (Figure 5.6). Anatomic variability (5 to 95% bounds) remained fairly constant throughout flexion and was larger than the domed 5 to 95% bounds which displayed a distinct narrowing beyond 60º of femoral flexion. Statistically significant differences in peak pressures were found at all flexion angles except where magnitudes crossed (10 and 70º femoral flexion); a similar trend was noted for stresses which were different at all flexion angles except 10, 50 and 70º.

Laterally-directed reaction forces on the patella from the femoral component were significantly higher in the anatomic design in early (< 30º) and late (> 90º) femoral flexion compared to the domed design. In general, anatomic shear forces were significantly less than the domed design in early flexion (< 40º), similar in mid-flexion, and greater in deep flexion (> 80º). Anatomic normal contact forces were significantly lower than domed normal forces at all angles below 100º.

With the selected level of input variability, the probabilistic analyses revealed very strong correlations ($r^2 > 0.7$) between several input and output kinematic parameters and highlighted distinct differences between the two patellar component designs (Table 5.1 and Table 5.2). Patellar flexion with the domed design was most correlated to component I-S ($r^2 = 0.68$) and F-E ($r^2 = 0.54$) alignment perturbations

compared to the greater anatomic design sensitivity to F-E ($r^2 = 0.73$) and then I-S position ($r^2 = 0.35$) (Figure 5.7). Anatomic M-L tilt was very sensitive to patellar tilt alignment ($r^2 = 0.83$, slope = -0.87) and to a lesser extent femoral I-E alignment ($r^2 = 0.40$, slope = 0.99); domed M-L tilt sensitivities were more distributed between M-L position ($r^2 = 0.66$, slope = -1.92), femoral I-E alignment ($r^2 = 0.56$, slope = 1.20), and patellar I-E alignment ($r^2 = 0.48$, slope = -0.42) (Figure 5.7). Patellar rotation and M-L shift for both implant types were considerably influenced by femoral I-E alignment ($r^2 > 0.7$). In both designs, an increase in external femoral rotation caused a lateral shift (anatomic slope = -0.81; domed = -0.84) and medial rotation (anatomic slope = 1.03; domed = 0.84) with respect to the femoral component (Figure 5.8 and Figure 5.9).

In general, contact mechanics showed weaker correlations to alignment perturbations than kinematics and forces but statistically significant differences were found between designs. Contact area in the domed design showed very little sensitivity to alignment perturbations (all $r^2 < 0.2$) while anatomic contact area was weakly correlated to patellar I-S ($r^2 = 0.36$) and rotation ($r^2 = 0.33$) alignment. Peak contact pressure and von Mises stress also showed weak correlations with only femoral I-E alignment above 0.3 for the domed design.

Although the amount of variability in contact forces was similar for both designs throughout the range of flexion, there were statistically significant differences in the range of outputs and some input parameters showing strong correlations to outputs. M-L forces were highly correlated to femoral I-E alignment for both the anatomic ($r^2 = 0.68$; slope = -34.78) and domed ($r^2 = 0.82$; slope = -36.20) designs with an increase in

femoral external alignment causing an increase in lateral reaction force acting on the patellar component (Figure 5.8 and Figure 5.9). Patellar M-L position was also correlated with M-L force for anatomic ($r^2 = 0.43$) and domed ($r^2 = 0.37$) designs. Normal forces were most sensitive to patellar F-E ($r^2 = 0.61$) alignment in the anatomic design and a combination of patellar M-L ($r^2 = 0.42$), I-S ($r^2 = 0.35$), F-E ($r^2 = 0.35$), and femoral I-E ($r^2 = 0.37$) alignment in the domed design. Anatomic resultant shear forces were most sensitive to patellar F-E ($r^2 = 0.45$), femoral I-E ($r^2 = 0.39$), and tilt ($r^2 = 0.33$) alignment compared to domed sensitivity to femoral I-E ($r^2 = 0.56$) and patellar I-S ($r^2 = 0.41$) alignment. At the current input variability level of $10 \pm 3.3\%$, perturbations in relative VMO contribution were not as important to kinematics or contact mechanics as alignment variability.

5.5. Discussion

Complications of the implanted PF joint are among the most common causes of total knee arthroplasty (TKA) failure (Brick and Scott, 1988; Meding et al., 2008) and may be attributable to malalignment of the patellar and femoral components. Computational analyses represent an efficient method for investigating the effects of patellar and femoral component alignment on output measures related to long term clinical success (i.e. tracking) and can be utilized to make direct comparisons between common patellar component design types. In this study, a dynamic, probabilistic FE model of an implanted PF joint successfully identified the most important surgical alignment parameters affecting patellar tracking, contact mechanics, and internal stresses and demonstrated output variability differences between anatomic and domed

implant designs. The strongest relationships between input and output parameters were identified via correlation coefficients and compared for relative importance via slope calculations between the two designs.

Femoral internal-external component alignment (Fem I-E) showed the strongest correlations to patellar shift, rotation, tilt, and M-L force for both the anatomic and domed designs. Slope calculations indicated a slightly greater influence of femoral I-E alignment on domed component shift, M-L force, and M-L tilt compared to the same responses with the anatomic design. Alternatively, femoral I-E alignment had a greater influence on anatomic patellar rotation compared to the domed response, which was likely attributable to the realignment of the patellar and femoral component I-S axes as the patella engaged the trochlear groove. The effect of femoral component I-E alignment on patellar tilt, rotation, shift, and M-L forces found in this study is in agreement with previous computational (Heegaard et al., 2001; Kessler et al., 2008) and experimental (Anglin et al., 2008; Armstrong et al., 2003; Miller et al., 2001) malalignment studies using domed implants.

The influence of patellar component alignment on output measures was found to be design specific. Conformity between anatomic articulating surfaces in the transverse plane was likely the cause of a greater influence in patellar tilt alignment on predicted patellar tilt response compared to domed tilt response. Alternatively, predicted patellar tilt in the domed design showed a high correlation to component M-L position that was absent in the anatomic design. These findings determined the most important surgical parameter affecting tilt response was component tilt alignment for the anatomic design

compared to patellar M-L and tilt alignment and femoral I-E position with the domed component. In an attempt to rank the importance of patellar component alignment on patellar tracking, Anglin et al. also highlighted these three parameters as the most influential with the domed design (Anglin et al., 2008). Although the relationship between patellar tilt and long-term TKA complications is not entirely clear, there is concern that abnormal tilt during femoral flexion could lead to increased risk of component wear (Lee et al., 1999) and soft tissue strains (Anglin et al., 2008; Armstrong et al., 2003).

In the sagittal plane, patellar flexion-extension alignment was more correlated and had more influence on predicted anatomic patellar flexion and normal and shear contact forces compared to domed flexion. Additionally, the lack of sagittal plane conformity in the domed design indicated a clear relationship between patellar inferior-superior alignment and predicted patellar flexion that was much less correlated in the anatomic design. Applying these findings to surgical planning would suggest placing emphasis on flexion-extension component position for both designs and additionally appropriate I-S positioning of the domed design to reduce the chance of increased tendofemoral or underlying bone strain due to excessive patellar flexion.

Patellar tracking and mechanics with the domed components should inherently be more robust to malalignment than the anatomic design due to a lack of rotary constraint and consistent contact regions between the constant radius patellar and femoral trochlear articulating surfaces. By comparison, the conforming anatomic patellar and femoral components were designed to more closely replicate natural

tracking throughout flexion and would therefore be less robust to alignment perturbations than the domed design. The current probabilistic method was able to demonstrate that the anatomic design was less robust to component malalignment than the domed design as evidenced by greater 5 to 95% output bounds across all output measures. The largest differences in predicted variability were observed in contact areas, pressures, and internal stresses with lesser differences in kinematics and contact forces between the two designs. The 100 Monte Carlo anatomic and domed PF models represent unique combinations of component alignment and quadriceps load distributions that could be representative of 100 patients with each design. With an estimated accuracy of ± 4% (Haldar and Mahadevan, 2000), the probabilistic 5 to 95% output bounds showed statistically significant differences in patellar flexion, rotation, contact area, and normal forces between the two designs throughout the simulated squat activity. By contrast, statistical results comparing patellar shift, tilt, M-L and shear forces, stress, and pressure values were not significantly different at certain locations within the flexion cycle.

Although focus of the current study was comparative in nature, there are several limitations that must be addressed. The current deterministic model was updated from a previous isolated PF kinematics verification study (Baldwin et al., 2009b) to apply a resultant quadriceps load distributed across multiple heads of the vastus and rectus femoris tendons represented by wrapping, deformable 2D structures connected to linear contractile elements. A specific load distribution and muscle orientation was adopted from literature (Farahmand et al., 1998) and applied via linear connector elements as performed in similar computational PF studies (Besier et al., 2008; Elias and Cosgarea,

2006; Mesfar and Shirazi-Adl, 2008; Powers et al., 2006), but model predictions would likely be more accurate if loads were applied via three-dimensional muscle volumes with localized fiber orientations (Blemker and Delp, 2005; Fernandez and Hunter, 2005). To account for the unknown state of quadriceps load distribution, VMO contribution was included as an input parameter in the probabilistic analyses which did not influence output measures as much as component alignment at the current level of variability (10 ± 3.3%). Although the selected levels of input variability used in this study for rotational (1 SD = 3.3° for flexion and tilt; 5° for rotation; 1.6° femoral I-E) and positional (1 SD = 1 mm) patellar component alignment were within the range (~3° to ~7°) of reported tibial and femoral surgical alignment variability (Restrepo et al., 2008; Siston et al., 2005), they may or may not replicate the true surgical variability associated with patellar resection plane cutting either with or without instrumentation. Additionally, the current probabilistic method does not account for any coupling or long-term adaptation effects, such as patient avoidance or load distribution compensation with a malaligned component that would likely affect predicted outcomes.

Despite these limitations, the current method seemed valid for comparing the two component designs under the selected loading condition. Additionally, the relative ranking of alignment parameters could be beneficial in designing advanced instrumentation for controlling patellar component surgical alignment by demonstrating which parameters are most important for a particular type of implant design. Alternatively, the predicted 5 to 95% confidence bounds can be a useful indicator of the expected amount of variability in a larger population of patients for different implant

designs and to demonstrate how variability changes within the flexion cycle (e.g. when

the patella engages the trochlear groove versus deep flexion).

Table 5.1 Correlation coefficients from the Monte Carlo probabilistic analysis for the domed patellar component design.

Model-Predicted Outputs	Perturbed Input Variables						
	Pat M-L	Pat I-S	Pat F-E	Pat Tilt	Pat Rot	Fem I-E	VMO Cont
Flexion-Extension	0.21	**0.68**	**0.54**	0.12	0.11	0.21	0.09
M-L Tilt	**0.66**	0.13	0.14	**0.48**	0.07	**0.56**	0.03
M-L Shift	0.41	0.15	0.13	0.27	0.11	**0.89**	0.11
M-L Rotation	0.26	0.20	0.13	0.15	0.11	**0.88**	0.22
M-L Force	**0.37**	0.18	0.12	0.24	0.11	**0.82**	0.35
Normal Force	**0.42**	**0.35**	**0.35**	0.25	0.09	**0.37**	0.10
Shear Force	0.32	**0.41**	0.29	0.28	0.09	**0.56**	0.24
Contact Area	0.13	0.21	0.12	0.10	0.09	0.13	0.11
Peak Contact Pressure	0.23	0.29	0.17	0.21	0.09	**0.34**	0.18
von Mises Stress	0.21	0.29	0.18	0.25	0.09	**0.37**	0.23

Table 5.2 Correlation coefficients from the Monte Carlo probabilistic analysis for the anatomic patellar component design.

Model-Predicted Outputs	Perturbed Input Variables						
	Pat M-L	Pat I-S	Pat F-E	Pat Tilt	Pat Rot	Fem I-E	VMO Cont
Flexion-Extension	0.15	**0.35**	**0.73**	0.09	0.31	0.07	0.08
M-L Tilt	0.16	0.03	0.04	**0.83**	0.10	**0.40**	0.06
M-L Shift	0.41	0.11	0.09	0.23	0.23	**0.72**	0.15
M-L Rotation	0.26	0.16	0.14	0.23	0.24	**0.81**	0.16
M-L Force	**0.43**	0.13	0.09	0.22	0.24	**0.68**	0.22
Normal Force	0.31	0.21	**0.61**	0.29	0.11	0.26	0.13
Shear Force	0.21	0.07	**0.45**	**0.33**	0.20	**0.39**	0.09
Contact Area	0.14	**0.36**	0.22	0.16	**0.33**	0.09	0.11
Peak Contact Pressure	0.29	0.27	0.29	0.21	0.28	0.14	0.10
von Mises Stress	0.29	0.24	0.28	0.21	0.19	0.14	0.15
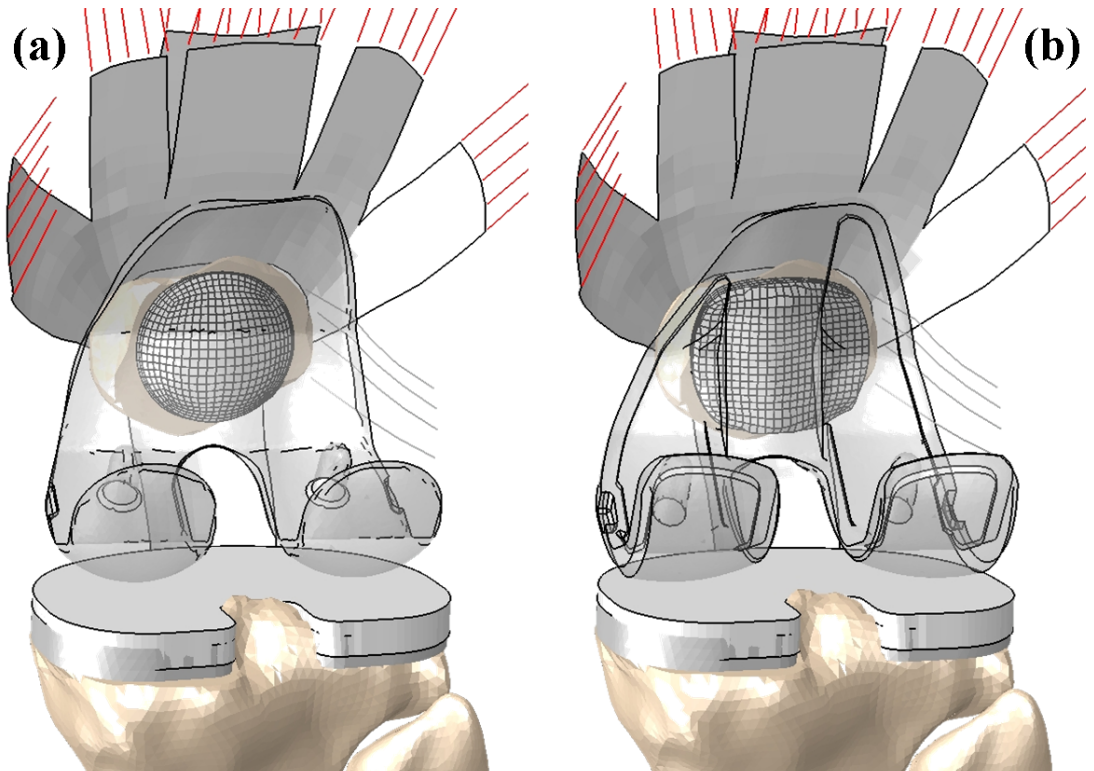
Figure 5.1 Implanted domed (a) and anatomic (b) computational knee models.
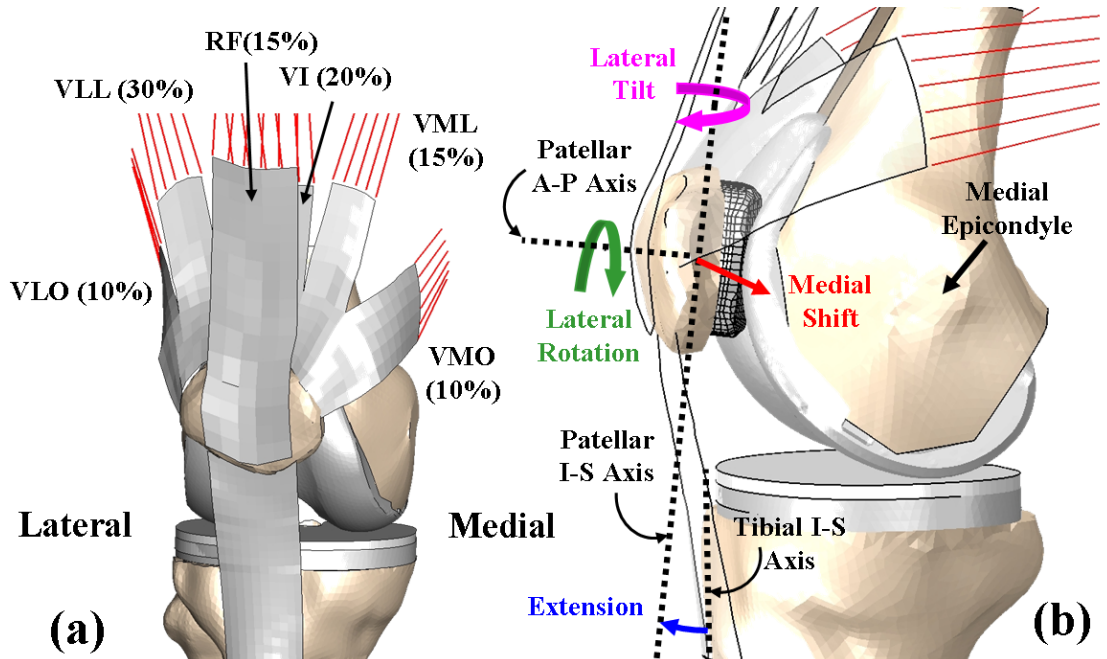
Figure 5.2 (a) Patellar ligament, rectus femoris, and vasti tendons of the extensor mechanism with quadriceps load distribution percentages (b) Output kinematic descriptions.
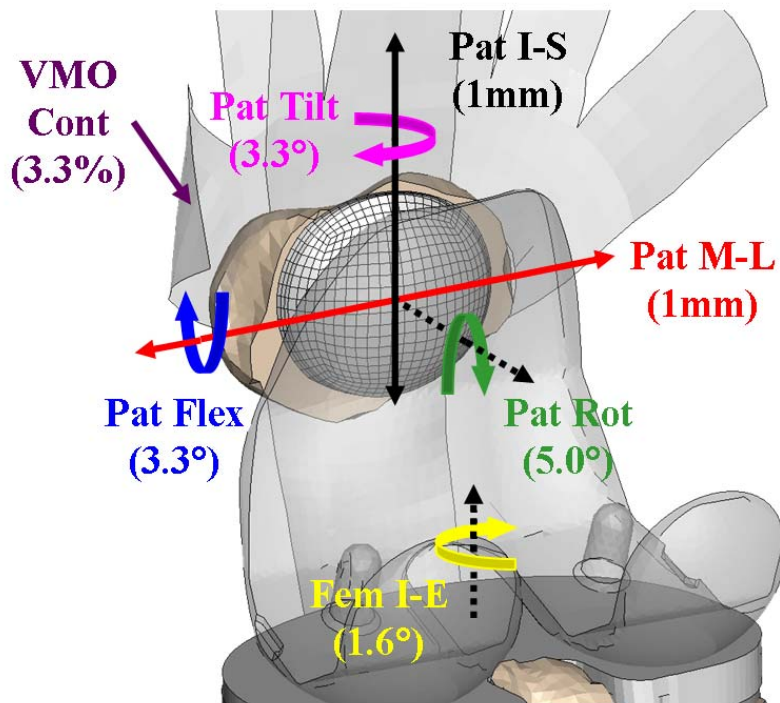
Figure 5.3 Probabilistic input parameters (standard deviations).
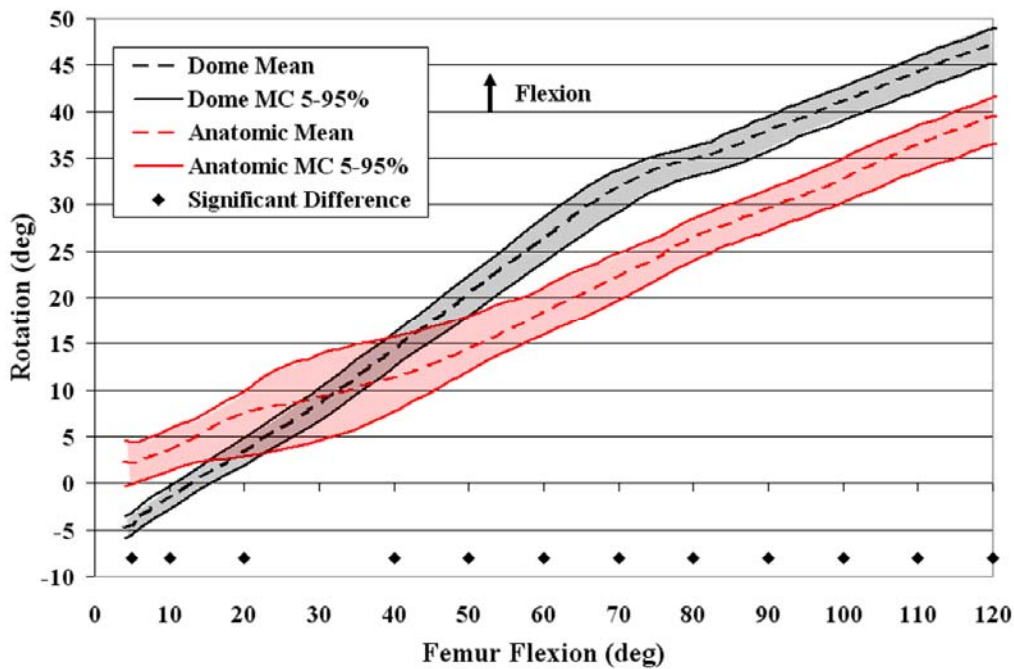
Figure 5.4 Model-predicted mean and 5 to 95% probabilistic bounds of patellar flexion with respect to the tibia for the anatomic and domed implant models.
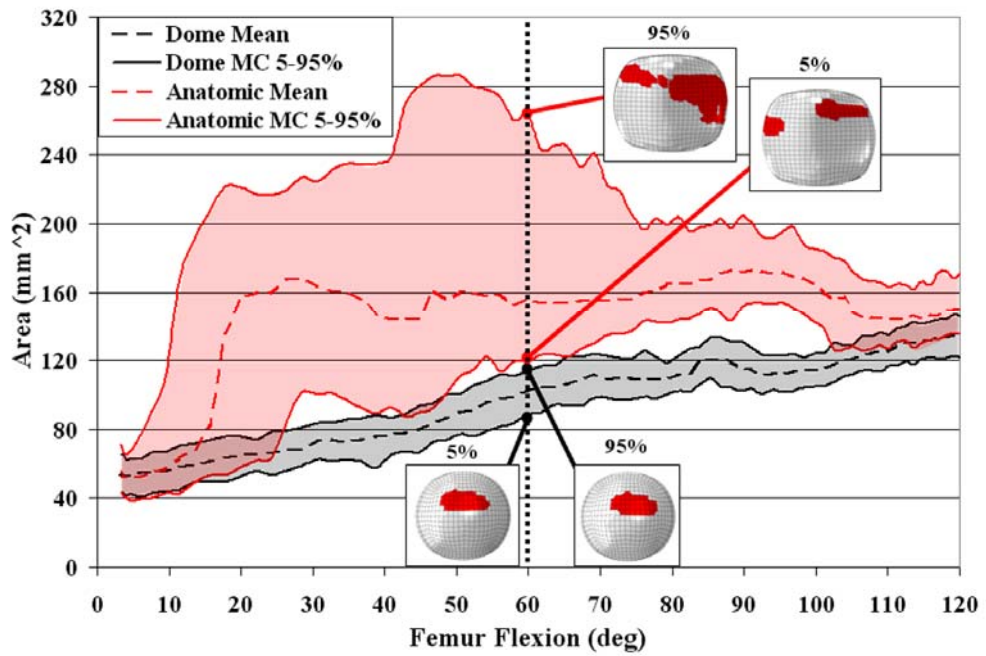
Figure 5.5 Model-predicted mean and 5 to 95% probabilistic bounds of contact areas for the anatomic and domed implant models; inlays show contact patch at 60° flexion for each design at the 5 and 95% confidence level.
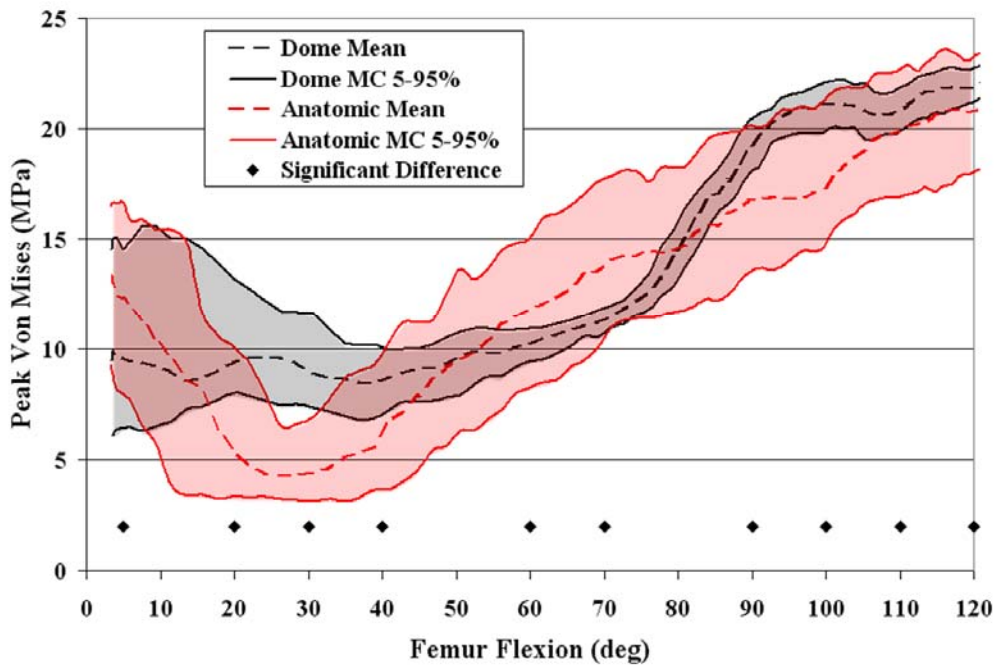
Figure 5.6 Model-predicted mean and 5 to 95% probabilistic bounds of component internal von Mises stress for the anatomic and domed implant models.

71
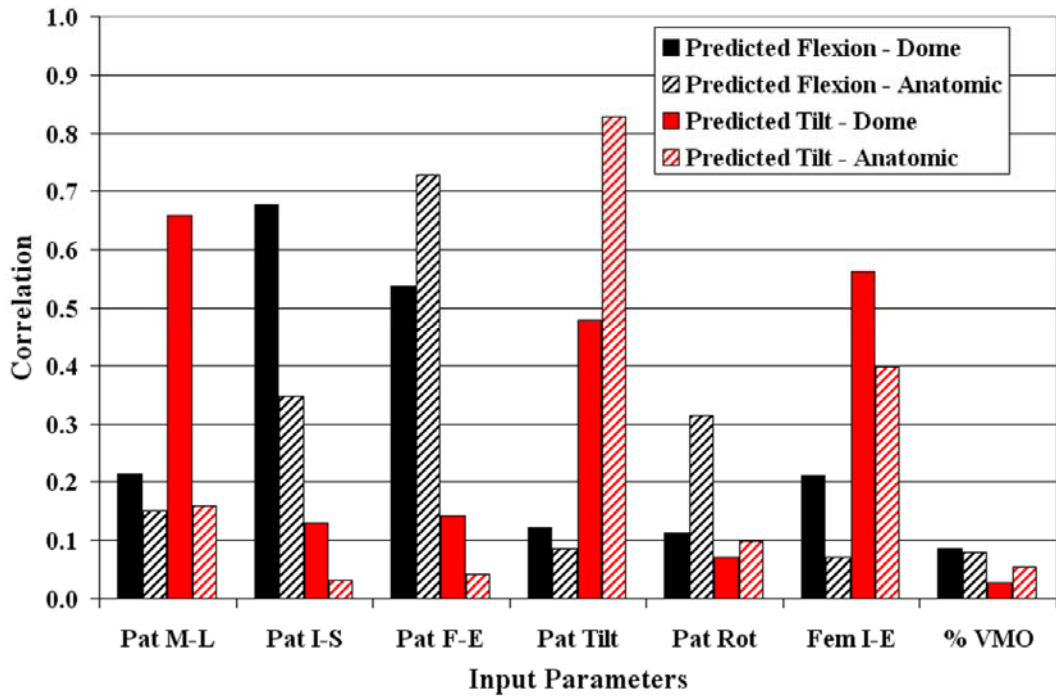
Figure 5.7 Domed and anatomic probabilistic correlation coefficients for patellar flexion and tilt.
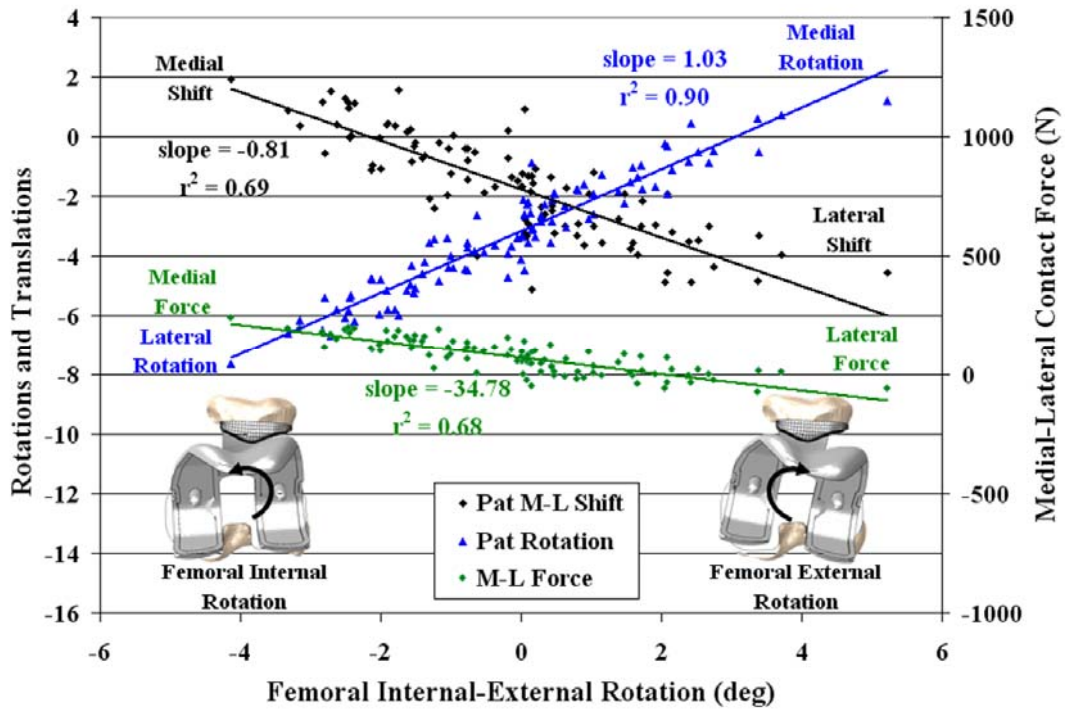
Figure 5.8 Scatter plot of patellar M-L shift, rotation, and M-L force as a function of femoral I-E rotation at 90° flexion for the anatomic implant model.
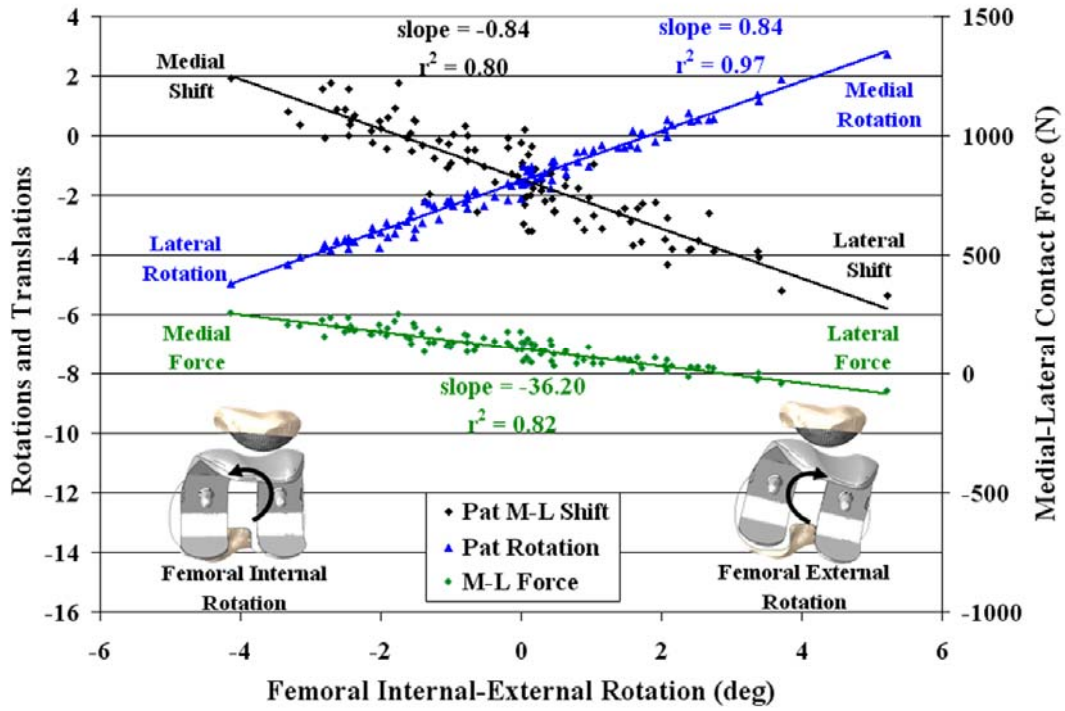
Figure 5.9 Scatter plot of patellar M-L shift, rotation, and M-L force as a function of femoral I-E rotation at 90° flexion for the domed implant model.

CHAPTER 6. VERIFICATION OF PREDICTED SPECIMEN-SPECIFIC NATURAL

AND IMPLANTED PATELLOFEMORAL KINEMATICS DURING DEEP KNEE

BEND

6.1. Background and Relevance

Model verification is an important aspect of computational biomechanical evaluations to ensure the constitutive representation in an FE solver can appropriately reproduce an idealized problem within an acceptable tolerance (Weiss et al., 2005). Due to the inherent variability of biological systems and tissues, it is pivotal that a computational model provides an accurate representation of biomechanical function. In attempting to represent a biomechanical system computationally, probabilistic methods (such as those described in the previous chapters) can be used to broaden the scope of a single deterministic model, but to ensure accuracy, some type of direct model verification against experimental measurements is typically necessary. The following two chapters present model verification studies that apply the previously described fiber-reinforced ligament representation to multiple specimen-specific cadaveric models to compare predicted 3D kinematics against experimental measurements.

6.2. The Kansas Knee Simulator

The computational studies in Chapters 6 and 7 were verified against experimental kinematic and actuator measurements recorded in the dynamic mechanical Kansas knee simulator (KKS). As a brief overview, the KKS is a multi-axis mechanical

system designed to reproduce simultaneous tibiofemoral and patellofemoral motion under the application of ankle and hip loads and the translation of a simulated quadriceps tendon (Maletsky and Hillberry, 2005) (Figure 6.1). Knee motion is constrained only by soft tissue structures or articulating surfaces at the knee joint. Implant components or cadaver bones can be rigidly mounted to a representative upper and lower limb through custom fixtures. The KKS ankle is a four DOF joint allowing medial-lateral motions and three rotations. Ankle internal-external and flexion-extension torques can be applied and rotations measured using a feedback control loop. The hip joint is a two DOF joint allowing flexion and inferior-superior (I-S) translation. A compressive or distractive I-S hip load is typically applied in conjunction with the ankle flexion load to maintain a reasonable load across the knee. Overall knee flexion is controlled by translation of the quadriceps actuator and constraint around the knee joint.

6.3. Introduction

The unknown etiology of patellofemoral pain syndrome (PFPS) in the natural knee and relatively high incidence of patellofemoral (PF) complications following total knee arthroplasty (TKA) surgeries (up to 50%) (Brick and Scott, 1988; Healy et al., 1995; Hsu et al., 1996; Komistek et al., 2000) highlight the importance of understanding the soft tissue structures, boundary conditions or applied loading, and articular geometry that contribute to overall PF mechanics. Multiple three-dimensional (3D) computational models have been created to investigate varying aspects of the PF joint, such as reaction forces (Dhaher and Kahn, 2002; Neptune et al., 2000; Powers et al.,

2006), contact mechanics (Besier et al., 2005a; Besier et al., 2005b; Cohen et al., 2001; Elias et al., 2004b; Fernandez and Hunter, 2005; Heegaard et al., 1995; Mesfar and Shirazi-Adl, 2005), kinematics (Elias et al., 2006; Elias et al., 2004a; Hefzy and Abdel-Rahman, 1996; Mizuno et al., 2001), and simulated surgical procedures (Cohen et al., 2003; Elias and Cosgarea, 2006). Verified computational models have been shown to be a valuable source of information regarding patellar tracking and contact mechanics, some of which would otherwise be difficult to obtain experimentally.

Computational models are also paramount during the design phase of joint replacement development, as insight into the kinematics and contact stresses/strains can guide design decisions without the cost and time associated with manufacture of parts and subsequent complex experiments. For this purpose, explicit finite element models of the Kansas knee simulator (KKS) have been developed and knee kinematic predictions for total knee replacement designs mounted in aluminum experimental fixturing were verified (Halloran et al., 2009). The KKS is an experimental knee simulator capable of dynamic loading (Maletsky and Hillberry, 2005), and computational representation of the simulator is an excellent platform for both verification of the computational methodology due to the known, carefully controlled loading conditions, as well as eventually a verified computational platform for evaluation of design-phase implant concepts. The goal of the present study was to take the next step in this systematic verification process, which was a complete update of the KKS model geometry and evaluation of isolated PF kinematic predictions for both natural and implanted cadaver conditions during simulated deep flexion in the KKS. The isolated PF evaluation was chosen in order to evaluate the PF model predictions

without the additional, perhaps confounding situation of simultaneous tibiofemoral kinematic prediction. Specifically, model-predicted three-dimensional PF kinematics were compared to experimental measures collected on the KKS during a simulated deep knee bend activity with four cadavers in their unaltered, natural states or implanted with either a cruciate-retaining (CR) or posterior-stabilized (PS) total knee replacement. For assessment of the tradeoffs between model accuracy and computational efficiency, analyses were performed with fully deformable as well as rigid articular surfaces. Due to the unknown initial state of the medial-lateral PF soft tissue constraint in the experimental setup, a model sensitivity analysis was performed to evaluate the affect of two-fold increases and decreases in ligament pre-tension and linear stiffness values on model-predicted kinematics.

6.4. Materials and Methods

6.4.1. In-vitro Testing

Four fresh-frozen unmatched, healthy cadaver knees (average age 63 yrs) were mounted in the five-axis Kansas Knee Simulator (KKS) to reproduce a simulated deep knee bend activity in their natural and implanted states (Figure 6.1). Each natural knee specimen was harvested from an intact lower limb X-rayed in its natural state in the frontal plane. Additionally, a series of sagittal magnetic resonance (MR) images (CISS sequence, in-plane resolution of 0.35 mm/pixel; 512x512 pixels; 1.0 mm slice thickness) were collected for model construction using an extremity coil with the knees fully extended. Tibial and femoral bones were transected approximately 20 cm from the natural joint line, cemented into aluminum fixtures and mounted in the KKS. A

two-piece aluminum clamp was used to rigidly attach the proximal portions of the rectus femoris (RF) and vastus intermedius (VI) tendons to a linear actuator aligned to the femoral shaft (Figure 6.1). Light emitting diode markers were rigidly fixed to the tibial and femoral fixtures and directly to the patella via bone screws to track six degree-of-freedom (DOF) kinematics using an Optotrak (Northern Digital Inc., Waterloo, CA) motion analysis system. A hand-held digital stylus was used to collect post-test 3D point data on specimen natural and implanted articular surfaces relative to their respective local frames and locate anatomical axes for describing relative motion using a three-cylindrical model of joint motion (Grood and Suntay, 1983). Relative 3D kinematics for the tibia and patella were calculated with respect to the femoral coordinate frame using a custom Matlab script (Mathworks Inc., Natick, MA).

A simulated deep knee bend activity was performed in the KKS using a combination of five load-controlled actuators at a simulated hip and ankle and a quadriceps actuator operating in position control to prescribe hip and knee flexion angles (Maletsky and Hillberry, 2005). During the deep knee bend cycle, knee flexion ranged from approximately 10 to 110° with all ankle actuators unconstrained (attempting to maintain zero internal-external torque and medial-lateral load). After the natural test series was completed for a single specimen, total knee arthroplasty (TKA) was performed by an orthopedic surgeon with either a posterior cruciate retaining (CR, two knees) or a posterior stabilized (PS, two knees) fixed bearing prosthesis. After surgery, the implanted knees were mounted again in the KKS and the knee bend activity was repeated.

6.4.2. Explicit Finite Element Model Development

Three-dimensional FE models of the KKS assembly (Figure 6.1) and the four cadaver specimens in their natural and implanted states (Figure 6.2) were created for dynamic analysis in Abaqus/Explicit^{TM} 6.6-1 (Dassault Systemes, Providence, RI). Natural anatomic 3D surfaces for the tibial, femoral, and patellar bones and articular cartilage were extracted from the MR images via segmentation using ScanIP (Simpleware, Exeter, UK). Implanted geometries of the PS or CR devices were generated from size-matched computer-aided design (CAD) surfaces. Bones and the implanted femoral components were represented with two-dimensional (2D) triangular shell elements; patellar and natural femoral articular surfaces were represented by three layers of eight-noded hexahedral elements (Figure 6.2). Bony and articular meshes were aligned in the models to their respective initial experimental positions using digitized surface point data.

A previously verified fiber-reinforced composite material model (Baldwin and Rullkoetter, 2007) consisting of non-linear, tension only springs embedded in a low-modulus, hyper-elastic deformable 2D quadrilateral mesh was used to represent the patellar ligament, rectus femoris (RF) and vastus intermedius (VI) tendons and medial and lateral PF ligaments (Figure 6.2). The composite structures were manually adjusted in separate planar analyses to match published experimental uni-axial force-deflection responses (Atkinson et al., 2000; Stäubli et al., 1999). The distal and proximal nodes of the patellar ligament mesh were rigidly fixed to the tibial tubercle and antero-inferior patellar border, respectively. The distal border of the VI mesh was attached to the

proximal patella at the interface of the articular and bony surfaces; the RF wrapped around the patellar anterior face. The RF and VI meshes were attached proximally to a set of translational elements to apply experimentally measured quadriceps loads. Patellofemoral ligament structures were rigidly fixed to the medial and lateral borders of the patella; femoral borders were attached to translator elements oriented posteriorly (Figure 6.2) to apply pre-tension. Penalty-based contact was defined between all soft tissue structures and relevant bony and articular surfaces for wrapping.

6.4.3. Patellofemoral Kinematic Verification

Dynamic FE analyses of each specimen were initiated by applying experimentally measured quadriceps load (200 N) to the patella to bring articular surfaces into contact. Natural cartilage and patellar button components were considered deformable, isotropic materials with mechanical properties adopted from previous studies (Deheer and Hillberry, 1992; Mesfar and Shirazi-Adl, 2006a) while bones and the femoral components were considered rigid. PF ligament pre-tension was manually adjusted in each knee to minimize differences in initial experimental and model positions after quadriceps load application and prior to femoral flexion. To isolate PF kinematics during the analyses, all tibio-femoral DOFs and measured quadriceps loads were prescribed between 10 and 110° femoral flexion. Model-predicted and experimental patellar kinematics were described with respect to the femur using a three-cylindrical model of motion (Grood and Suntay, 1983, and Figure 6.2). Average and maximum root mean square (RMS) differences between model-predicted and experimental translations and rotations for each knee specimen were calculated between

10 and 110° femoral flexion and then averaged across all four specimens for the natural and implanted states separately.

For the rigid analyses, articular contact in the natural models was based on a linear pressure-overclosure relationship adopted from Blankevoort et al., and a previously verified pressure-overclosure relationship developed by Halloran et al. in the implanted models (Blankevoort et al., 1991b; Halloran et al., 2005b). Natural contact was considered frictionless whereas a friction coefficient of 0.04 was applied in the implanted models (Godest et al., 2002). Model sensitivity analyses were conducted to evaluate the computational efficiency and accuracy of treating articular surfaces as rigid and to determine the effect of modifying PF ligament mechanical properties on model-predicted kinematics. PF ligament pre-tension and linear stiffness values were adjusted to either one half or double the manually optimized values in the deformable analyses and repeated to establish which predicted DOFs were most affected by the property perturbations. Additionally, all analyses were repeated without PF ligaments. RMS differences between experimental and predicted kinematics for the rigid and PF ligament-adjusted models were calculated for each natural and implanted model.

6.5. Results

All natural and implanted computational models with deformable articular surfaces remained stable through the range of motion with model run times of approximately 1 and 6 hours, respectively, on a single processor Windows-based desktop PC. In natural and implanted states, the patella consistently translated posteriorly and inferiorly and flexed with respect to the femur while trends in medial-

lateral translation (shift), medial-lateral tilt and medial-lateral spin rotation were less consistent (Figure 6.3, single natural specimen shown; Figure 6.4, single implanted specimen shown). Average RMS differences between predicted and experimental natural patellar kinematics were less than 3.1° and 1.7 mm for rotations and translations, respectively, while differences in implanted kinematics were less than 2.1° and 1.6 mm between 10 and 110° femoral flexion (Table 6.1). Maximum RMS differences for individual specimens were less than 5.7° and 3.0 mm and 3.5° and 2.9 mm for the natural and implanted states, respectively. The rigid contact formulation reduced natural and implanted model run times to approximately 0.5 and 1.5 hours, respectively, representing a two- and four-fold decrease compared to the deformable analyses. Average RMS values for natural and implanted rigid analyses were very similar to the deformable analyses at 3.7° and 1.9 mm and 2.0° and 1.6 mm, respectively (Table 6.2).

Perturbations in PF constraint provided by the medial and lateral PF ligaments had a negligible effect on model-predicted patellar spin, medial-lateral and anterior-posterior translations but increased average RMS differences in flexion, medial-lateral tilt, and inferior-superior translations for both the natural and implanted models (Table 6.2). Patellar flexion predictions were most affected by doubling initial PF ligament pre-tension in both the natural and implanted models and eliminating PF constraint in the natural models (Figure 6.6, single natural specimen shown). Medial-lateral tilt rotation and inferior-superior translation predictions were sensitive to increases or decreases in PF constraint in all models (Figure 6.6, single implanted specimen shown).

6.6. Discussion

Complications involving the PF joint in the natural and implanted knee occur frequently enough to warrant continued biomechanical evaluations. Verified computational models present an efficient method for understanding PF mechanics to address clinically relevant issues or evaluate implant component performance during the design phase. Accordingly, the objective of the current study was to evaluate an explicit FE approach for predicting PF kinematics of multiple specimen-specific knee models in both their natural and implanted states under experimentally measured loads and soft tissue constraint representation. Previous finite element models of the Kansas knee simulator have been developed to predict tibiofemoral and PF kinematics during a simulated gait cycle using various implants mounted in aluminum fixturing, but not in cadavers (Guess and Maletsky, 2005; Halloran et al., 2005a; Halloran et al., 2006; Halloran et al., 2005c). The current study focused on updating the entire geometry of the KKS and including the constraint representation of the extensor mechanism and medial-lateral PF ligaments. An isolated PF joint was evaluated by applying experimentally measured quadriceps loads and prescribing the measured specimen-specific tibiofemoral kinematics. Modeling cadaveric specimens introduced additional variability due to the unknown state of ligamentous constraint during the experiments. Prior to femoral flexion in the models, specimen-specific adjustments to PF ligament pre-tension was required to reproduce initial experimental positions upon application of measured quadriceps loads. Using a deformable contact formulation for all articular surfaces, model-predicted results showed strong agreement with experimental measurements as average RMS differences were less than 3.1° and 1.7 mm and

maximum RMS differences were less than 5.7° and 3.0 mm for all models over the range of femoral flexion investigated (10 to 110°).

The explicit FE solution method is well suited for maintaining computational stability during large displacement dynamic analyses such as the articulation of the patella on the femur in a deep knee bend cycle. An evaluation of the tradeoffs between model accuracy and computational time was conducted using both deformable and rigid contact formulations for the natural and implanted articular surfaces. The rigid contact analyses showed negligible differences in model-predicted PF kinematics with reductions in run times of two (natural) and four (implanted) times that of the deformable analyses. In a similar study, Halloran et al. predicted kinematics of two types of implant designs under gait loading conditions with both deformable and rigid contact formulations (Halloran et al., 2005c), and found kinematic predictions to be nearly identical between the two contact formulations for the implants. They also reported average RMS differences between model-predicted and experimentally measured PF rotational and translational values to be less than 2.7° and 2.7 mm. The average RMS values of less than 2.1° and 1.6 mm in the implanted models of the current study represent slightly improved model accuracy despite the larger sample size, greater range of motion studied and uncertainty associated with modeling cadaveric soft tissue constraint.

Predicted PF kinematics in the models matched experimental measurements well for all DOFs and were found to be in agreement with trends and magnitudes of previously reported values for patellar flexion and inferior and posterior translations in

84

the natural (Amis et al., 2006; Heegaard et al., 1994) and implanted (Heegaard et al., 2001; Komistek et al., 2000) knee. Overall, greater accuracy was achieved in predicting translations versus rotations and in the implanted versus natural models. This was likely attributable to the influence of articular surface geometry on tracking, which in the case of the implanted models was based on precise CAD surface geometry compared to natural patellar and femoral articular cartilage surfaces reconstructed with segmentation and standard meshing techniques. Additionally, the low conformity between the domed patellar button and femoral components in the implanted models allowed PF rotations to be more influenced by ligament pre-tensioning and by the change in quadriceps load path in deeper flexion. By comparison, the more conforming natural articular surfaces reduced the effect of ligament pre-tensions and largely directed patellar motion in deep flexion.

Reproducing the appropriate amount of constraint provided by the medial and lateral PF ligaments was found to affect model accuracy in both the natural and implanted knees, agreeing with previous anatomic and biomechanical studies about the importance of PF constraint (Amis et al., 2003b; Luo et al., 1997; Smirk and Morris, 2003). In the current study, the linear stiffness of the PF ligaments in the cadaveric specimens were not measured during the experimental test series and were therefore based on previously published anatomic studies (Amis et al., 2003b; Andrikoula et al., 2006; Atkinson et al., 2000; Nomura et al., 2005; Smirk and Morris, 2003). In each model, varying amounts of pre-tension was applied to PF ligament femoral borders prior to flexion in an attempt to reproduce initial experimental positions. Due to the unknown affects of these mechanical properties on kinematic predictions, a subsequent

sensitivity study was performed to quantify the affects of increasing or decreasing PF constraint. Model predictions for flexion, medial-lateral tilt, and inferior-superior translation were most adversely affected by changing PF constraint while medial-lateral rotation and translation and anterior-posterior translation were relatively unaffected. Eliminating the PF ligaments or over-tightening them had a greater effect on predicted kinematics than changes in ligament stiffness. Despite adopting literature-based stiffness values for the PF ligaments, acceptable model accuracy was achieved by manually optimizing PF ligament pre-tension in the deformable analyses. For subsequent analyses without a matched cadaveric specimen, a probabilistic approach should be utilized to represent the uncertainty in the medial and lateral soft-tissue constraint (Laz et al., 2006, Easley et al., 2007).

Although this study focused on matching predicted and experimental PF kinematics, the current approach could also be used to evaluate clinically relevant mechanical outcomes in the natural and implanted knee such as contact mechanics or patellar bone strains for insight into clinical issues. Additionally, the set of verified models could be used to investigate perturbations in component alignment, soft tissue pre-tension, or quadriceps load on PF mechanics through the use of design of experiment or probabilistic techniques. Ongoing efforts are focused on the verification of simultaneous tibiofemoral and PF predictions with cadaveric specimens in the KKS.

Table 6.1 Average and maximum RMS differences between model-predicted and experimental PF rotations and translations between 10 and 110° femoral flexion for natural and implanted states.

Model State	Rotations (deg)			Translations (mm)		
	Flexion	Spin	Tilt	Med-Lat	Ant-Post	Inf-Sup
Natural (avg)	2.9	2.1	3.1	0.9	1.7	1.7
Implanted (avg)	2.1	1.4	1.9	0.7	1.3	1.6
Natural (max)	5.7	4.5	5.2	1.6	2.5	3.0
Implanted (max)	3.3	1.8	3.5	1.3	2.9	2.7

Table 6.2 Average RMS differences between model-predicted and experimental PF rotations and translations between 10 and 110° femoral flexion for natural and implanted states with deformable and rigid contact, with reduced linear stiffness, increased pre-tension and no PF constraint.

Average RMS Differences for Natural Models			
Model Type	Flexion Rotation (deg)	Medial-Lateral Tilt Rotation (deg)	Inferior-Superior Translation (mm)
Deformable contact	2.9	3.1	1.7
Rigid contact	3.0	3.7	1.9
Half linear stiffness	3.4	4.5	2.2
Double pre-tension	4.6	3.9	3.4
No PF constraint	4.1	5.0	3.0
Average RMS Differences for Implanted Models			
Deformable contact	2.1	1.9	1.6
Rigid contact	2.0	1.8	1.6
Half linear stiffness	1.8	2.4	1.9
Double pre-tension	3.4	2.4	1.8
No PF constraint	2.0	2.1	2.5
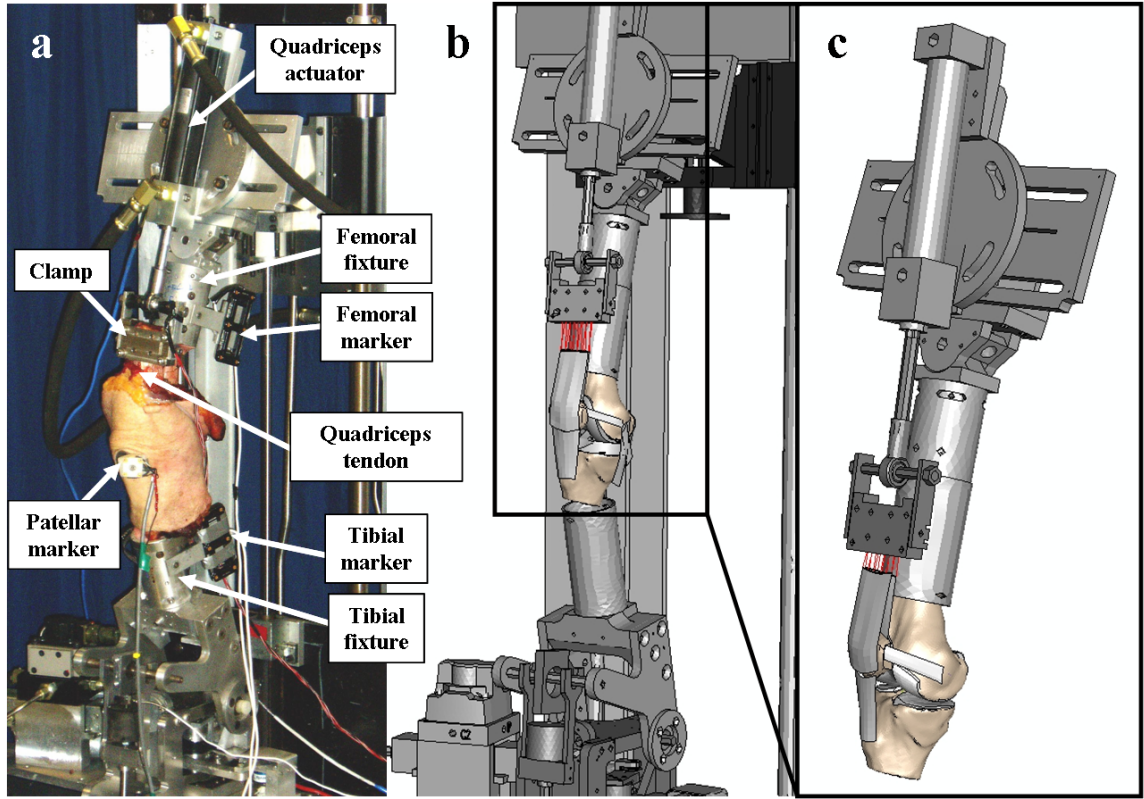
Figure 6.1 (a) Natural knee specimen in experimental KKS setup, (b and c) finite element computational model of the full KKS setup.
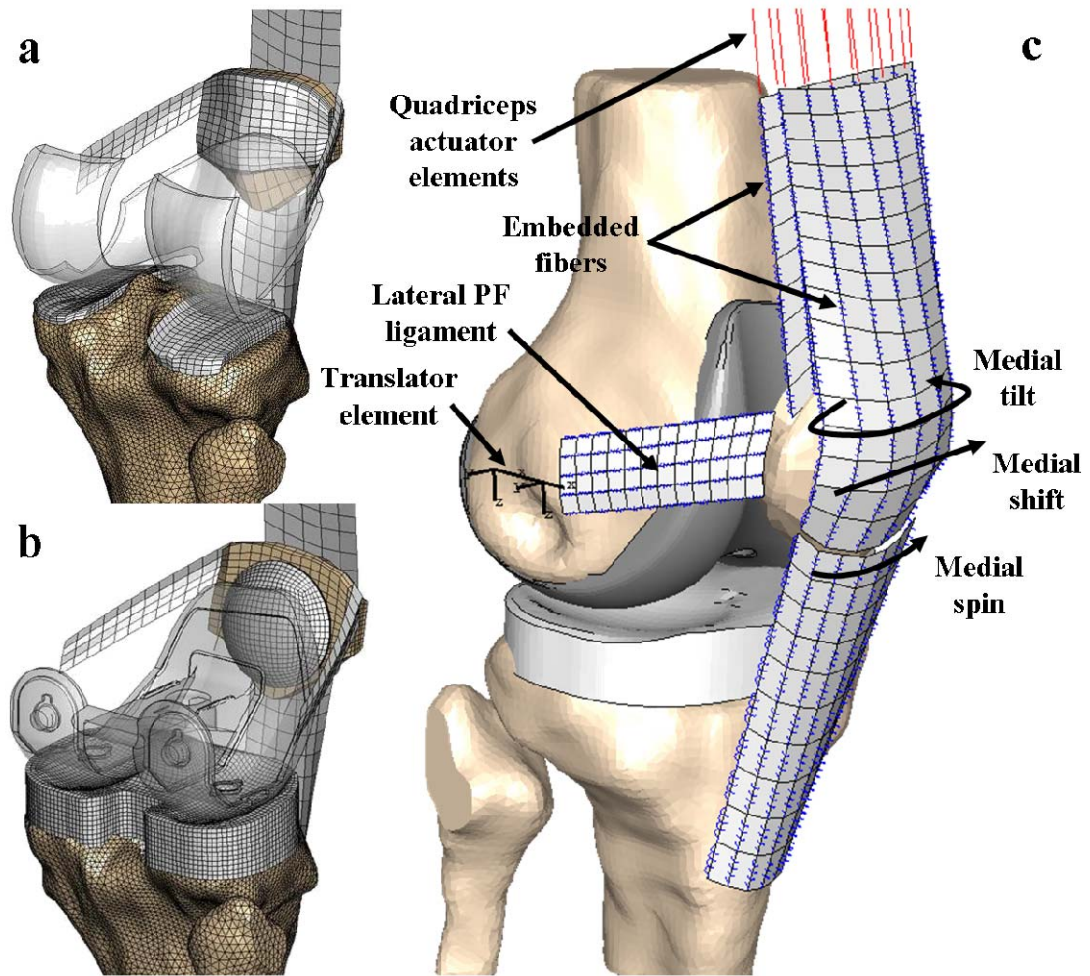
Figure 6.2 Computational model of (a) natural and (b) implanted specimen; (c) diagram of fiber-reinforced soft tissue structures and patellar motion descriptions.
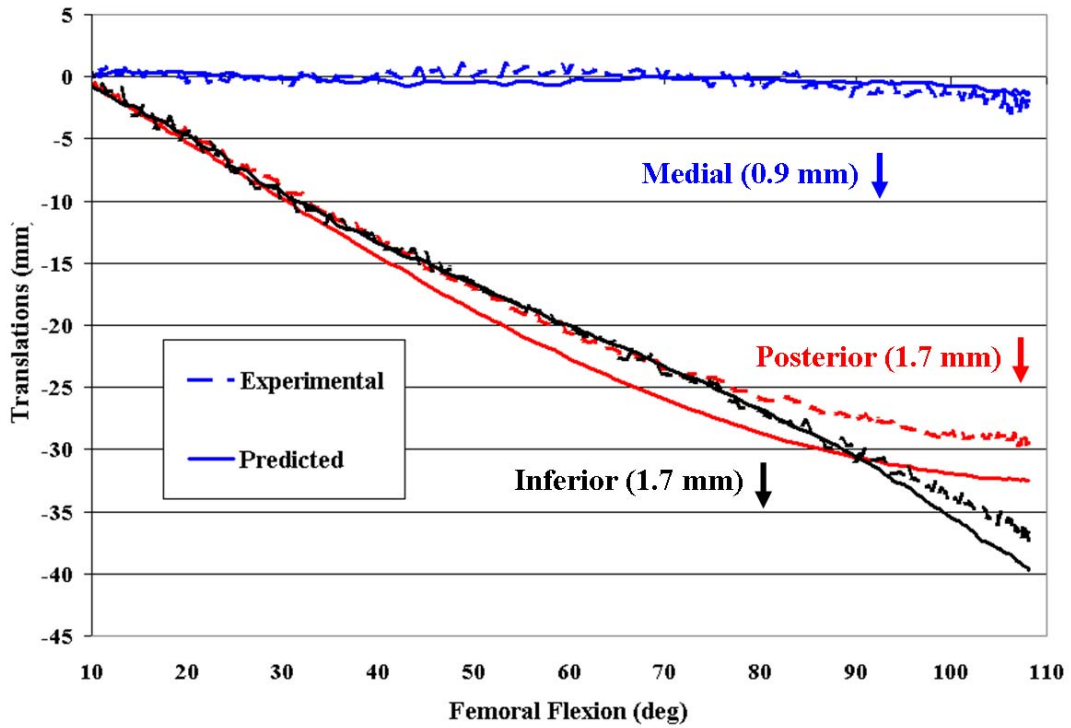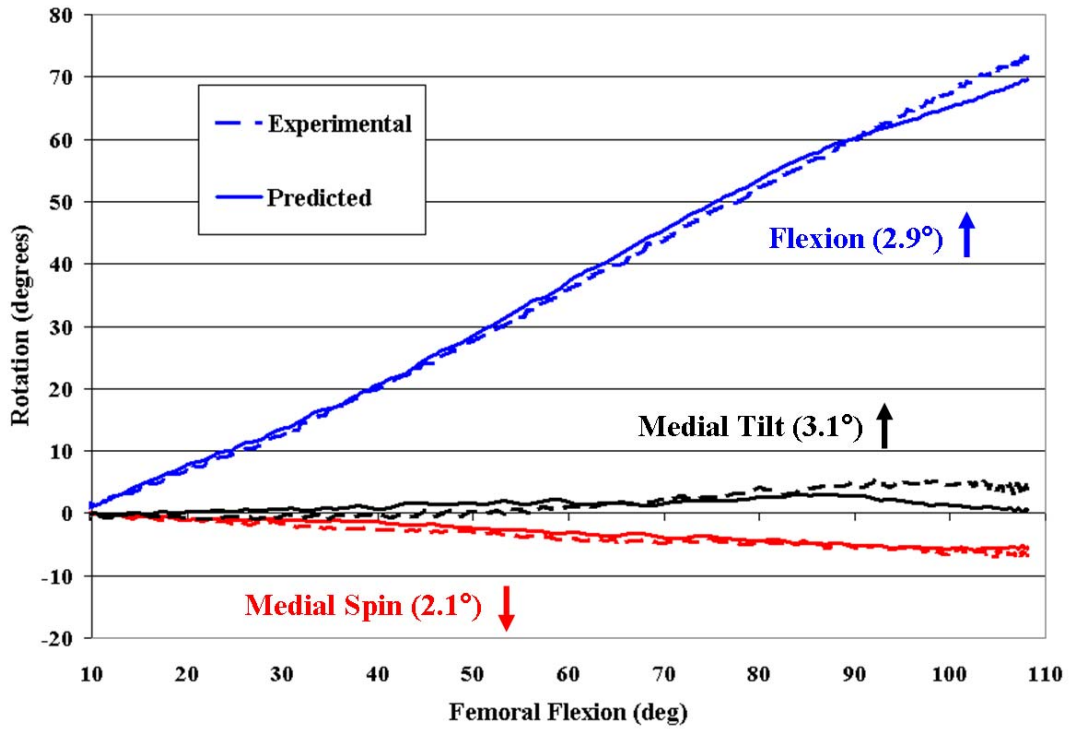
Figure 6.3 Model-predicted and experimental kinematic results for single natural specimen; labels represent direction of patellar motion with respect to the femur with average RMS values for all natural specimens in parentheses.
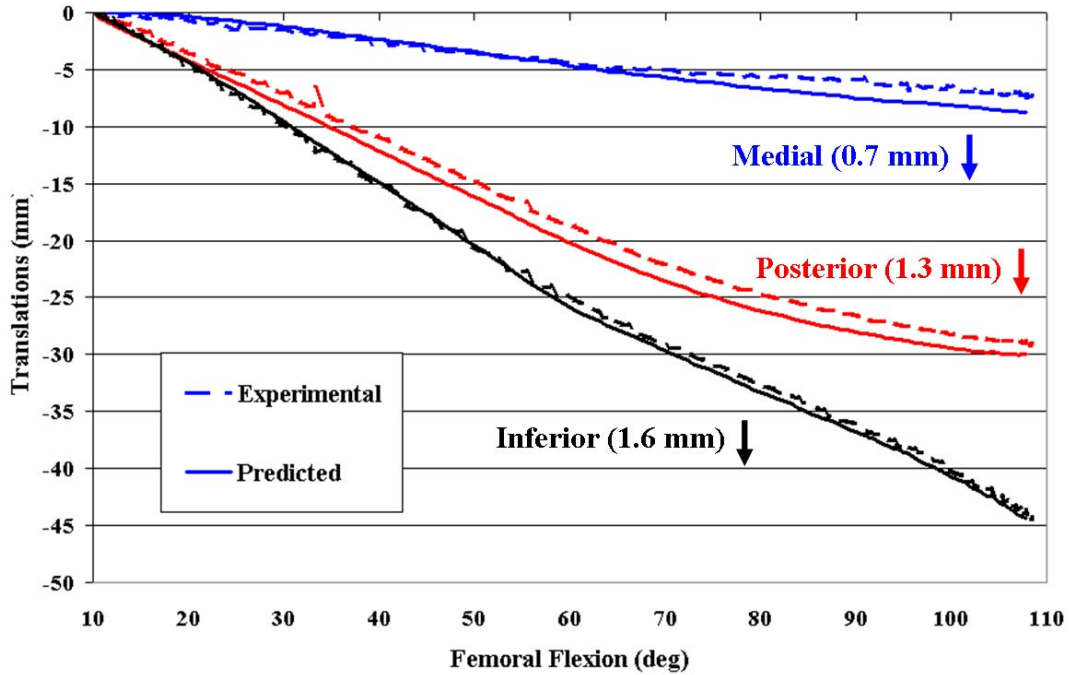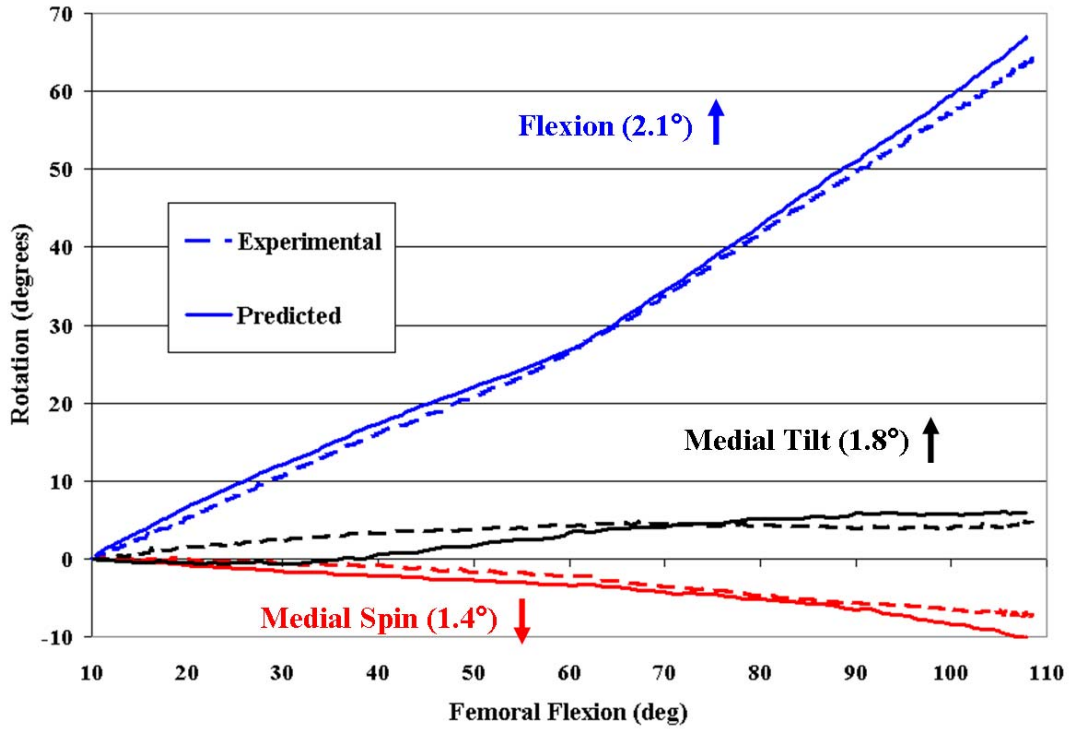
Figure 6.4 Model-predicted and experimental kinematic results for single implanted specimen; labels represent direction of patellar motion with respect to the femur with average RMS values for all implanted specimens in parentheses.
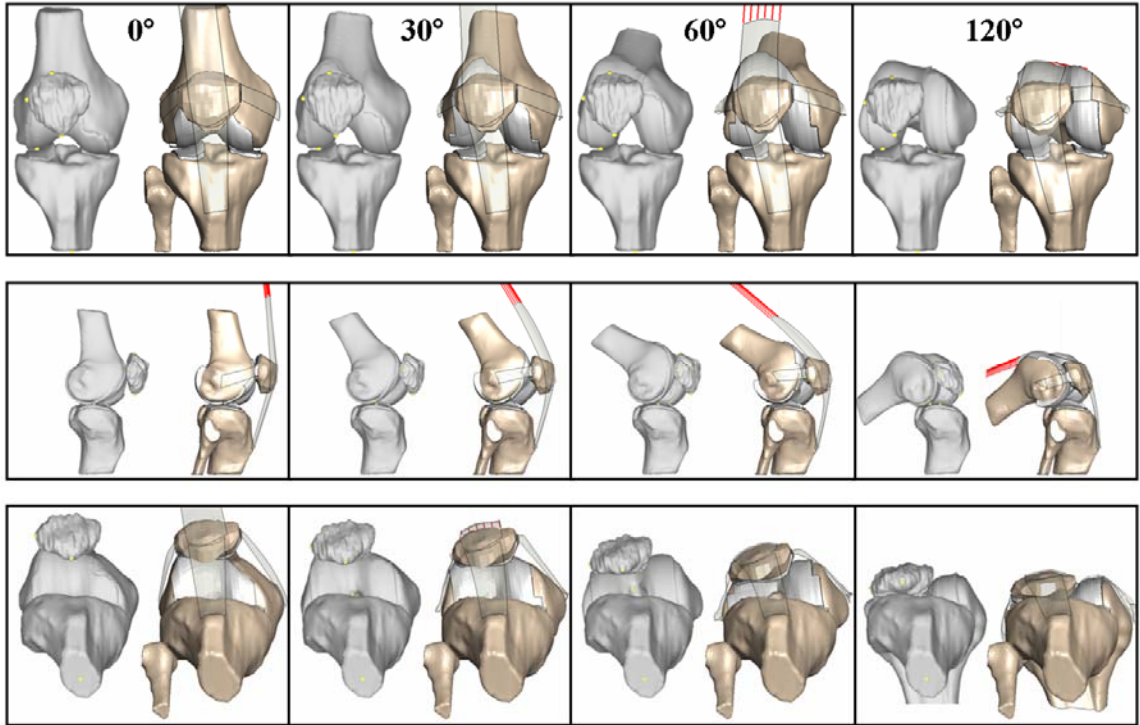
Figure 6.5 Comparison of experimental and model-predicted bone positions at 0, 30, 60, and 120° femoral flexion for a single natural specimen in frontal (top), sagittal (center), and axial (bottom) views; extracted bone geometries are on the left and predicted motion on the right.
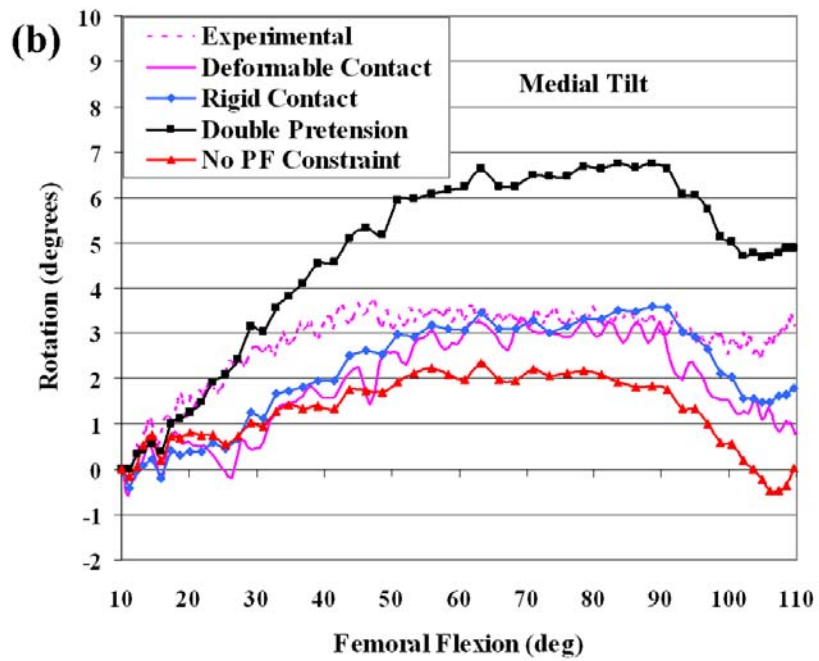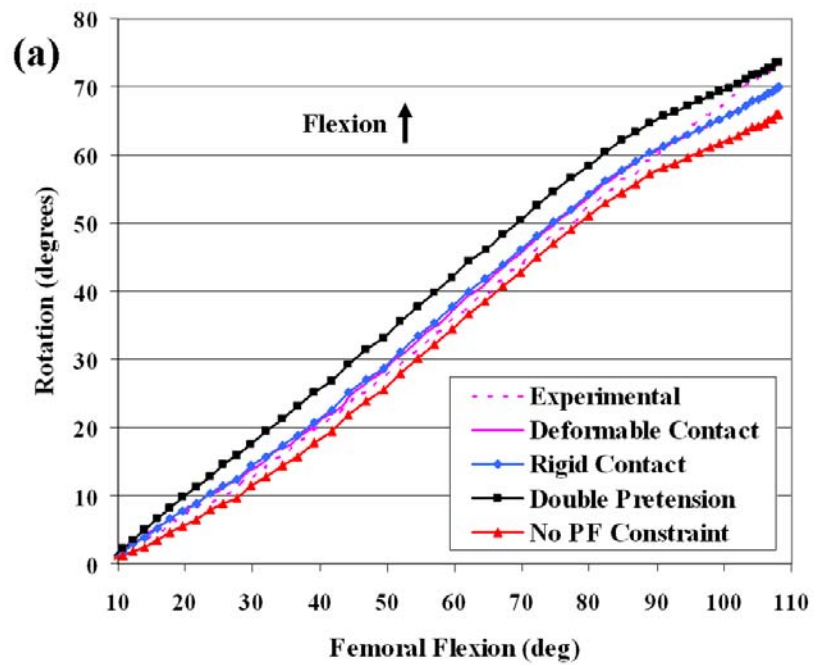
Figure 6.6 (a) Model-predicted patellar flexion from contact and ligament sensitivity analyses (single natural specimen shown); (b) model-predicted patellar tilt rotation from contact and ligament sensitivity analyses (single implanted specimen shown).

CHAPTER 7. PREDICTING WHOLE JOINT MECHANICS DURING SIMULATED

DYNAMIC LOADING USING SPECIMEN-SPECIFIC LIGAMENTOUS

CONSTRAINT

7.1. Introduction

Assessing long-term *in-vivo* performance of total knee arthroplasty (TKA) is complicated by the relationship between component design, surgical alignment, patient-specific anatomy, and ligamentous constraint. The difficulty and variability associated with implant evaluation under *in-vivo* conditions has caused implant manufacturers to characterize component designs in the more controlled and repeatable loading environment provided by dynamic mechanical simulators. *In-vitro* force-controlled mechanical simulators have been developed to elucidate the relationship between natural and implanted constraint and whole joint kinetics and kinematics under simulated dynamic activities (Maletsky and Hillberry, 2005; Withrow et al., 2006; Zavatsky, 1997). Whole joint cadaveric testing of implanted specimens provides a useful indication of implant performance under applied loads and realistic soft tissue constraint, but becomes time and cost-prohibitive as a design-phase tool in evaluating multiple component designs, sizes, and potential surgical alignments.

Computational models represent an efficient way to perform component design evaluations under a variety of dynamic loading conditions that would otherwise be difficult and costly to accomplish experimentally. Several finite element (FE) studies

have been performed using representative implant component surfaces and simplified soft tissues to investigate kinematics and contact mechanics under the loading and boundary conditions of a mechanical simulator (Godest et al., 2002; Halloran et al., 2009; Halloran et al., 2005c). Godest et al. investigated the influence of mesh density, friction, and step size on model-predicted kinematics and contact stresses for an explicit FE model of a cruciate retaining design in the Stanmore knee simulator (Godest et al., 2002). Halloran et al. presented a method for accurately predicting implanted kinematics and contact mechanics at a reduced computational cost in an explicit FE model of the Stanmore knee simulator for tibiofemoral articulations and the Purdue knee simulator for patellofemoral articulations (Halloran et al., 2005c). In a more recent model verification study, the same group created an explicit FE model of implanted components mounted in the Kansas knee simulator (KKS) and demonstrated strong agreement between model-predicted and experimental kinematics for simultaneous tibiofemoral and patellofemoral results under gait loading conditions (Halloran et al., 2009). These component-level model verification studies represent an important step in the development of a design-phase computational tool, but may not fully capture the relationship between component design and anatomic soft tissue constraint that could influence short and long-term *in-vivo* performance. Accordingly, a more recent explicit FE model of the KKS was developed to compare model-predicted natural and implanted kinematics of the isolated patellofemoral joint under the influence of representative soft tissue structures of the extensor mechanism and medial and lateral patellofemoral ligaments (Baldwin et al., 2009b).

The current study represents the next step in the systematic development of a computational evaluation tool for implant design under the combined influence of passive soft tissue constraint and applied loading within the KKS. Specifically, a previously verified computational method for generating specimen-specific tibiofemoral constraint through ligament optimization was applied to four posterior-stabilized (PS) implanted cadaveric specimens prior to prediction of simultaneous tibiofemoral and patellofemoral six degree-of-freedom (DOF) kinematics during simulated gait and deep knee bend activities the KKS. Root mean square (RMS) differences between model-predicted and experimental kinematics and machine actuator load and displacements were averaged across all four specimens and compared for each loading condition. Ligament recruitment and forces were recorded in the models with optimized and non-optimized tibiofemoral constraint.

7.2. Methods

7.2.1. In-vitro testing

A series of dynamic *in-vitro* tests were conducted on four fresh-frozen unmatched cadaver left knees implanted by an orthopedic surgeon with posterior-stabilized (PS) components to determine simultaneous whole joint kinematics during simulated dynamic deep knee bend and gait activities on a mechanical simulator. Each specimen was harvested from an intact leg by transecting tibial and femoral bones approximately 20 cm from the natural joint line, mounting the bones into fixtures and leaving the remaining tissues intact after TKA surgery. Infrared light emitting diodes were rigidly fixed to tibial and femoral fixtures and directly to the patellar bone via

surgical bone screws to collect three-dimensional (3D) kinematic data with an Optotrak motion analysis system (Northern Digital Inc., Waterloo, CA). Each implanted knee specimen was subjected to a passive laxity envelope assessment by manually applying internal-external and varus-valgus torques to an instrumented prosthetic foot and recording resulting rotations at 0, 30, 60, and 90° femoral flexion (Figure 7.1). After envelope assessments, cadaver specimens were placed in the Kansas knee simulator (KKS) for whole joint kinematic data collection (Figure 7.1). Using a two-piece aluminum clamp, the proximal portions of the rectus femoris (RF) and vastus intermedius (VI) tendons were rigidly fixed to a linear actuator to reproduce the original specimen quadriceps angle in the frontal plane.

Simulated deep knee bend and gait activities were performed in the KKS using a combination of five load-controlled actuators at a simulated hip and ankle and a quadriceps actuator operating in position control to prescribe hip and knee flexion angles (Maletsky and Hillberry, 2005). During the deep knee bend cycle, knee flexion ranged from approximately 10 to 120° with all ankle actuators attempting to maintain zero internal-external torque and medial-lateral load. The gait cycle consisted of heel strike, stance and swing phases with out-of-plane loading applied at the ankle, as has been described previously (Halloran et al., 2009). During each simulated dynamic activity, tibial, femoral, and patellar six DOF motions were recorded along with position and load data from ankle, hip, and quadriceps actuators. Experimental kinematics were converted to relative tibiofemoral and patellofemoral motions using digitized anatomical bony axes and a three-cylindrical open chain description of motion (Grood and Suntay, 1983) calculated via custom scripting in Matlab 7.1 (Mathworks

Inc., Natick, MA). After dynamic testing, each specimen was dissected down to the bones to record spatial position of implanted components, bony surfaces, and collateral ligament attachment areas relative to the local bony frames using a hand-held digitization probe (Figure 7.2).

7.2.2. Finite Element Model Development

A 3D finite element (FE) model of each implanted cadaver specimen was created for dynamic analysis in ABAQUS/Explicit[TM] 6.8-1 (Dassault Systemes, Providence, RI). Specimen-specific tibial, femoral, and patellar bones were manually extracted from the magnetic resonance (MR) images via segmentation using ScanIP (Simpleware, Exeter, UK). Size-matched 3D models of PS implant component surfaces were aligned to the extracted bones using experimental point data. For all analyses, bones and femoral components were meshed with two-dimensional (2D) triangular shell elements; patellar and tibial components were represented by 8-noded solid hexahedral elements generated in Hypermesh 9.0 (Altair Inc., Troy MI). To reduce computational time, bones and implant components were considered rigid for all analyses with component contact defined by a previously verified pressure-overclosure relationship (Halloran et al., 2005c).

Specimen-specific ligamentous geometry crossing the tibiofemoral joint was developed using post-test dissection to identify bony attachment locations and 3D extracted surfaces from MR scans while mechanical properties were established using a dual-phase optimization approach to match computational and experimental laxity envelopes through a range of femoral flexion. Six capsular soft tissue structures

crossing the implanted tibiofemoral joint were represented, including the lateral collateral and popliteofibular ligaments (LCL, PFL), anterior lateral capsule (ALC), superficial medial collateral ligament (sMCL), and medial and lateral posterior capsule. Prior to optimization, LCL and sMCL tibial and femoral attachments were placed at the centroid of experimental attachment areas; PFL, ALC, and posterior capsular structure attachment locations were adopted from literature descriptions (LaPrade et al., 2007a; LaPrade et al., 2003; Shahane et al., 1999; Shelburne et al., 2006).

Due to the complexity and run time associated with optimizing the attachment locations and mechanical properties of multiple ligament structures to match experimental laxity envelopes at multiple flexion angles, the optimization process was performed in two phases. In the first optimization phase, a tibiofemoral ligament model which represented ligament structures as multiple bundles of point-to-point tension-only nonlinear springs similar to (Baldwin et al., 2009c) was used for computational efficiency (Figure 7.2). The simulated annealing global optimization algorithm was customized in Matlab 7.1 (Mathworks, Natick, MA) to perturb sixteen input parameters: ALC and PFL initial strain and stiffness, localized LCL and sMCL strain (anterior, middle, posterior bundles), LCL and sMCL stiffness (applied to all bundles), and inferior-superior and anterior-posterior LCL and sMCL femoral attachment locations. Using literature values to define initial and maximal bounds for strain and stiffness (Blankevoort and Huiskes, 1996; Li et al., 1999; Mommersteeg et al., 1996a), differences in model-predicted and experimental internal-external laxity responses at 30°, 60° and 90° femoral flexion were minimized at 1 N*m intervals between 5 and 10 N*m torque levels. Using phase I optimized ligament stiffness and femoral attachment

positions, phase II re-optimized ligament initial strains using two-dimensional (2D) fiber-reinforced structures to include a distribution of internal fibers and account for ligament-to-bone or component interactions (Figure 7.2).

To account for extensor mechanism contact with the bony and component surfaces during deep knee flexion in the KKS, a 3D ligament representation was implemented for the patellar and quadriceps tendons (PT, QT) and patellofemoral ligaments. Dimensions were determined from MR images and represented by 3D fiber-reinforced structures attached to the inferior and anterosuperior patellar borders, respectively (Figure 7.3); uni-axial tension responses were manually perturbed in separate analyses to match literature values (Stäubli et al., 1999). Medial and lateral patellofemoral ligament dimensions and stiffness values were adopted from literature (Atkinson et al., 2000); a previously verified pre-tensioning method was adopted to account for the initial pretensioned state of the patellofemoral ligaments prior to the dynamic tests (Baldwin et al., 2009b). Contact was defined between extensor mechanism structures and bones and implanted components to allow wrapping in deep flexion.

7.2.3. Simulating Dynamic Activities in the KKS

A rigid body model of the KKS was generated in ABAQUS/Explicit[TM] using 2D meshed surface representations of simulator components with appropriate centers of mass and rotary inertias (Figure 7.3) and kinematic joints to replicate DOFs at the simulated hip and ankle. Each specimen-specific implanted knee model was aligned to initial positions within the KKS using point data and recorded machine actuator

positions. Experimental hip and ankle actuator loads and quadriceps translations were applied for the simulated deep knee bend and gait activities.

Model verification was performed by comparing predicted tibiofemoral and patellofemoral kinematics and KKS hip, ankle, and quadriceps actuator responses to experimental measurements at every 5º of femoral flexion during the deep knee bend activity or at every 5% of the gait cycle. Model-predicted and experimental root mean square (RMS) differences were averaged across all four specimens for each kinematic and machine output for each activity. To normalize actuator output comparisons between the two loading cycles, machine feedback was calculated as a percentage of maximum (minimum) values within the cycle. Ligament recruitment patterns were identified for each tibiofemoral structure by measuring bundle forces. To illustrate the importance of specimen-specific tibiofemoral constraint on predicted kinematics, all models were also analyzed with no initial pre-strain, literature-based stiffness values, and femoral collateral attachment locations at the epicondyles to represent a literature-based or pre-optimized model. Kinematics and ligament strains were then compared between the optimized specimen-specific and literature-based constraint models for the two simulated dynamic activities.

7.3. Results

7.3.1. Tibiofemoral Constraint Optimization

All specimen-specific implanted knee models matched experimental internal-external laxity torque-rotation curves with the dual-phase optimization approach better

than using literature-based mechanical properties and initial femoral attachment locations. The computationally efficient phase I optimization required an average of 320 iterations (~32 hours at 6 minutes per iteration) to reach acceptable convergence as the initial state of phase II optimization, which required an average of 66 iterations to achieve convergence (~78 hours). Phase II model-predicted internal-external torque-rotation responses summed over 5 to 10 N*m torque levels at 30, 60 and 90° femoral flexion matched experimental measurements to within an average of 2.4 ± 0.6° across all specimens compared to average literature-based differences of 9.6 ± 1.3° (Figure 7.4). Individual specimen optimization results can be found in Appendix A.

7.3.2. Tibiofemoral Kinematic Verification

Trends and magnitudes of model-predicted tibiofemoral kinematics showed good agreement with experimental measurements for all DOFs across all four specimens and in both the deep knee bend and gait loading conditions (Figure 7.5) (Table 7.1). Under prescribed translation of the quadriceps tendon, model-predicted knee flexion in the simulated deep knee bend (up to 120°) and gait (up to 60°) matched experimental knee flexion with an average difference of 4.0 ± 0.8° and 2.7 ± 0.6°, respectively. Using the phase II-optimized tibiofemoral ligamentous constraint, deep knee bend tibiofemoral internal-external (I-E) and varus-valgus (V-V) rotations had average RMS differences from experimental measurements of 1.5 ± 0.4° and 0.9 ± 0.5°, respectively; anterior-posterior (A-P), inferior-superior (I-S), and medial-lateral (M-L) translations matched within 1.8 ± 0.8 mm, 1.2 ± 0.7 mm, and 0.6 ± 0.1 mm, respectively (Figure 7.5). Tibiofemoral I-E and V-V rotations during gait matched experimental

measures to within 2.2 ± 1.8° and 0.7 ± 0.3°; translation RMS differences for A-P, I-S, and M-L were 2.7 ± 0.2 mm, 1.2 ± 0.6 mm, and 0.7 ± 0.5 mm respectively (Figure 7.5). Predicted tibiofemoral V-V rotations and M-L translations showed the strongest correlations for all models (average for both loading conditions less than 1° and 1 mm) whereas I-E rotations and A-P translations showed the greatest differences. Tibiofemoral I-E rotations and A-P translations showed better agreement in the deep knee bend compared to the gait cycle.

7.3.3. Patellofemoral Kinematic Verification

Similar to tibiofemoral kinematic results, model-predicted patellofemoral kinematics matched experimental trends and magnitudes well for all DOFs across all four specimens and in both loading conditions. Patellofemoral flexion, medial-lateral tilt and spin rotations in the deep knee bend activity produced average RMS differences of 2.9 ± 1.1, 2.4 ± 0.2, and 1.7 ± 0.7° respectively while local A-P, I-S, and M-L translations (with respect to the femur) differed by 1.8 ± 0.7, 3.1 ± 1.1, and 1.4 ± 0.3 mm (Figure 7.6). In the gait model, average RMS differences for patellofemoral flexion, tilt, and spin were 3.2 ± 0.5°, 2.7 ± 1.1°, and 0.8 ± 0.5°; average RMS differences for A-P, I-S, and M-L translations were less than 1.9 mm (Figure 7.6). Patellar spin, M-L and A-P translations showed the strongest agreement for both loading conditions whereas patellar flexion and tilt typically showed the weakest correlations.

7.3.4. KKS Machine Feedback Verification

Model predictions for machine feedback showed good correlation with experimental measures for the two simulated activities. With experimental quadriceps translation as a model input, predictions for quadriceps load as a function of peak load had an average RMS difference of $17.7 \pm 6.5\%$ throughout the deep knee bend cycle and $20.1 \pm 8.2\%$ in the gait cycle (Figure 7.7). In general, model-predicted KKS sagittal plane motions showed strong correlations across all specimens with hip flexion and translation and ankle flexion demonstrating less than 5.0 % RMS differences in the deep knee bend cycle and 6.8 % in the gait cycle.

7.3.5. Ligament Responses

Substantial differences between the phase-II optimized and non-optimized TF ligament recruitment patterns demonstrated the need for combining experimental laxity data collection and computational specimen-specific optimization. Specifically, in the optimized ligament deep knee bend models, strains increased in the anterior and middle sMCL bundles up to an average peak of 5.5% and 2.5%, respectively from full extension up to ~80° femoral flexion with a subsequent decrease in deeper flexion (Figure 7.8). By comparison, non-optimized sMCL anterior and middle bundle strains were much higher with an average peak of 11.2% and 5.9%, respectively. Recruitment in the lateral optimized structures (LCL, ALC, and PFL) showed less consistent patterns, but were generally slack in early to mid flexion and recruited in late (> 90°) flexion. Lateral structure strain predictions in the non-optimized models were much higher than optimized models with average peak strains of 7.0, 10.8, and 11.0 for the

LCL, PFL, and ALC ligaments, respectively. Model-predicted kinematics using the non-optimized ligaments showed weaker agreement with experimental measurements compared to models with the optimized ligaments for femoral flexion ($5.2 \pm 1.9°$), tibiofemoral I-E rotations ($2.2 \pm 1.2°$) (Figure 7.8), and patellofemoral flexion ($3.3 \pm 0.6°$) during the deep knee bend. Similar trends were found in those kinematic outputs during the gait cycle but to a lesser extent due to the reduced range of motion.

7.4. Discussion

Achieving long-term clinical success after TKA is dependent on a variety of patient and surgical factors, but can be directly influenced by implant component design and soft tissue balancing. Whole-joint mechanical simulators are useful design-phase tools capable of demonstrating implant performance under simulated dynamic loading conditions and ligamentous constraint during *in-vitro* testing, but are time and cost prohibitive for evaluating the spectrum of component types, sizes, surgical alignments, and loading conditions that may exist *in-vivo*. Computational models represent an effective method for conducting parametric or probabilistic assessments of implant performance under a variety of loading and boundary conditions, but must be verified against experimental measurements to ensure accuracy of model predictions. The current study showed strong agreement between model-predicted and experimental six DOF tibiofemoral and patellofemoral kinematics in all four specimen-specific implanted cadaver models during dynamic, force-driven models of simulated deep knee bend and gait activities generated in the mechanical Kansas knee simulator.

The current work presents the most recent in a series of explicit FE model verification studies to predict simultaneous whole joint implant mechanics under force-driven, dynamic loading and the influence of specimen-specific soft tissue constraint. An earlier study by Halloran et al. demonstrated strong agreement between model-predicted and experimental kinematics in separate tibiofemoral and patellofemoral component-only models under gait loading conditions (Halloran et al., 2005c). In a more recent study, Halloran et al. compared simultaneous tibiofemoral and patellofemoral kinematic predictions of implant components under prescribed hip rotation and applied quadriceps and ankle loads and representative 2D patellar and quadriceps tendons during a simulated gait cycle in the KKS (Halloran et al., 2009). A follow up study by Baldwin et al. incorporated 2D soft tissue representations for the extensor mechanism structures to evaluate isolated natural and implanted patellofemoral kinematics in four specimen-specific cadaveric knee models during a simulated deep knee bend activity in the KKS (Baldwin et al., 2009b). Even with the additional uncertainty associated with incorporating soft tissue constraint, model-predicted kinematics showed strong agreement with experimental measurements and similar RMS differences to previous studies.

Despite the substantial increase in scope and complexity of predicting simultaneous tibiofemoral and patellofemoral kinematics in four specimen-specific implanted cadaver knee models and replicating experimental control of knee flexion via translation of the quadriceps actuator, RMS differences in the current study were similar to previous studies for both the simulated deep knee bend and gait activities. Due to the larger range of motion in the deep knee bend cycle (up to 120°), model predictions for

106

knee flexion were slightly worse (4.0°) than in the gait cycle (2.7°), but matched experimental knee flexion well in both shape and timing.

Average RMS differences between model-predicted and experimental tibiofemoral kinematics were similar in the deep knee bend and gait cycles with the exception of I-E rotation (1.5 versus 2.2°) and A-P translation (1.8 versus 2.7 mm), which was likely attributable to the out-of-plane rotations applied at the ankle and abrupt change in knee flexion during the swing phase of the gait cycle. However, tibiofemoral translational and rotational RMS differences averaged across both activities (up to 1.8° and 2.3 mm) were only marginally greater than the hip-driven component-only model reported by Halloran et al. (1.5° and 0.5 mm).

Adaptation of a 3D representation for the extensor mechanism structures and conversion to a hip and ankle force-driven representation of the KKS with only quadriceps translations to control knee flexion produced similar patellofemoral kinematic differences to previous hip-rotation-driven and isolated patellofemoral KKS studies. The current RMS differences in patellofemoral medial-lateral tilt rotations (2.6°) and I-S translations (2.5 mm) averaged between the two loading conditions were similar to those by Halloran et al. (2.2°, 1.9 mm) and Baldwin et al. (1.9°, 1.6 mm). In all three studies, patellofemoral tilt and I-S translations were the most difficult to predict, which can most likely be attributed to the unknown state of constraint provided by the patellofemoral ligaments and dependence on proper representation of the patellar-quadriceps tendon complex.

Although ligament recruitment is highly dependent on attachment locations and mechanical properties, the phase II optimized specimen-specific tibiofemoral ligament constraint demonstrated localized recruitment patterns and magnitudes in the sMCL and LCL throughout the range of femoral flexion that were in agreement with previous medial (Arms et al., 1983; Gardiner et al., 2001; Hull et al., 1996; Park et al., 2005; Warren and Marshall, 1979; Wymenga et al., 2006) and lateral (Meister et al., 2000; Sugita and Amis, 2001) recruitment studies. By contrast, when the collateral ligament femoral attachments were moved to the epicondyles (Woo et al., 2006), and all tibiofemoral ligament structures given literature-based stiffness values (Blankevoort et al., 1991b) and no initial strains to represent a generic, literature-based setup, the ligaments demonstrated strain magnitudes beyond published failure levels during uni-axial pull tests (Butler et al., 1986) and kinematic predictions for femoral and patellar flexion and tibiofemoral I-E showed weaker agreement to experimental measurements. The combination of optimizing tibiofemoral ligamentous constraint to experimentally-derived, specimen-specific laxity envelopes and subsequent modeling of the simulated dynamic activities in the KKS represents a step towards addressing what Weiss et al. describe as a need for further research into specimen-specific whole knee joint evaluations (Weiss et al., 2005).

There were several limitations and assumptions that likely contributed to RMS differences between experimental and model predicted kinematics. Specimen-specific collateral ligament, patellar tendon, and quadriceps tendon dimensions and attachments were established from a combination of MR data and experimental dissection, but the size and attachments of the remaining tibiofemoral capsular structures and

patellofemoral ligaments were adopted from literature. Additionally, no post-test mechanical testing was performed on any structures to establish their mechanical properties, which previous sensitivity studies have shown can substantially affect predicted kinematics (Baldwin et al., 2009c; Beillas et al., 2007). Constraint across the tibiofemoral joint was established from the experimental envelope and ligament optimization process, but the solution is likely not unique and could benefit from further experimental methods to verify localized strain (Arms et al., 1983) or force (Griffith et al., 2009) measurements during the envelope assessments and dynamic activities. Additional sources of error can arise from the computational reproduction of experimental component alignment and local anatomic axes from digitized point data (Morton et al., 2007). The assumed values for damping and friction in KKS mechanical actuators, joints, and bearings used in this study have been shown previously to influence model kinematic predictions (Halloran et al., 2009), but were not verified experimentally for the current KKS model.

This study demonstrated strong agreement between model and experimental kinematic predictions under the simplified, controlled loading of a mechanical simulator, but the current methods of establishing specimen-specific tibiofemoral constraint with wrapping, fiber-reinforced ligaments could be adapted to muscle-driven models (Barink et al., 2005; Beillas et al., 2004; Shelburne et al., 2006) to simulate additional activities (i.e. chair rise or stair ascent). The ability of the explicit FE method to predict kinematics, contact mechanics, tendon-to-component articulations, and internal polyethylene stresses (using a deformable mesh) could be invaluable in addressing clinically relevant issues such as crepitation or wear and provide implant

designers with relevant information to potentially reduce the design cycle. Future work will investigate the feasibility of evaluating natural cadaveric specimens in the KKS to provide direct kinematic and ligament recruitment comparisons in the pre- and post-operative knee joint.
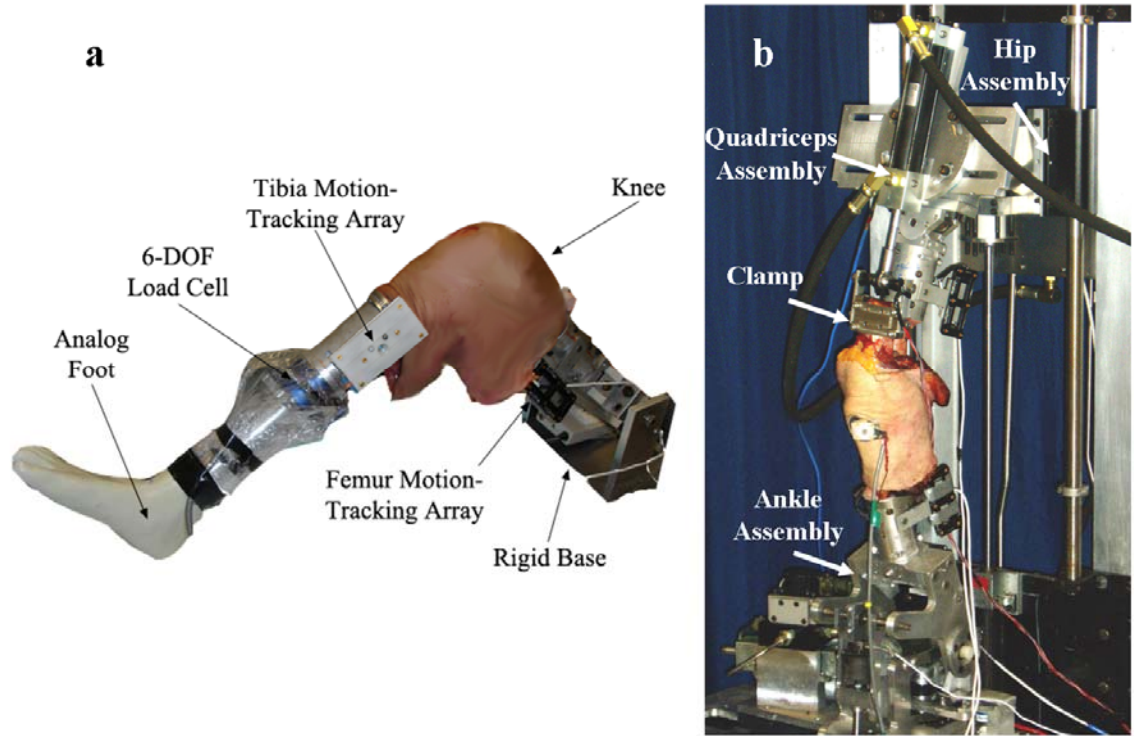
Figure 7.1 (a) Experimental passive laxity envelope assessment setup with instrumented prosthetic foot and (b) Implanted cadaveric specimen in Kansas knee simulator.
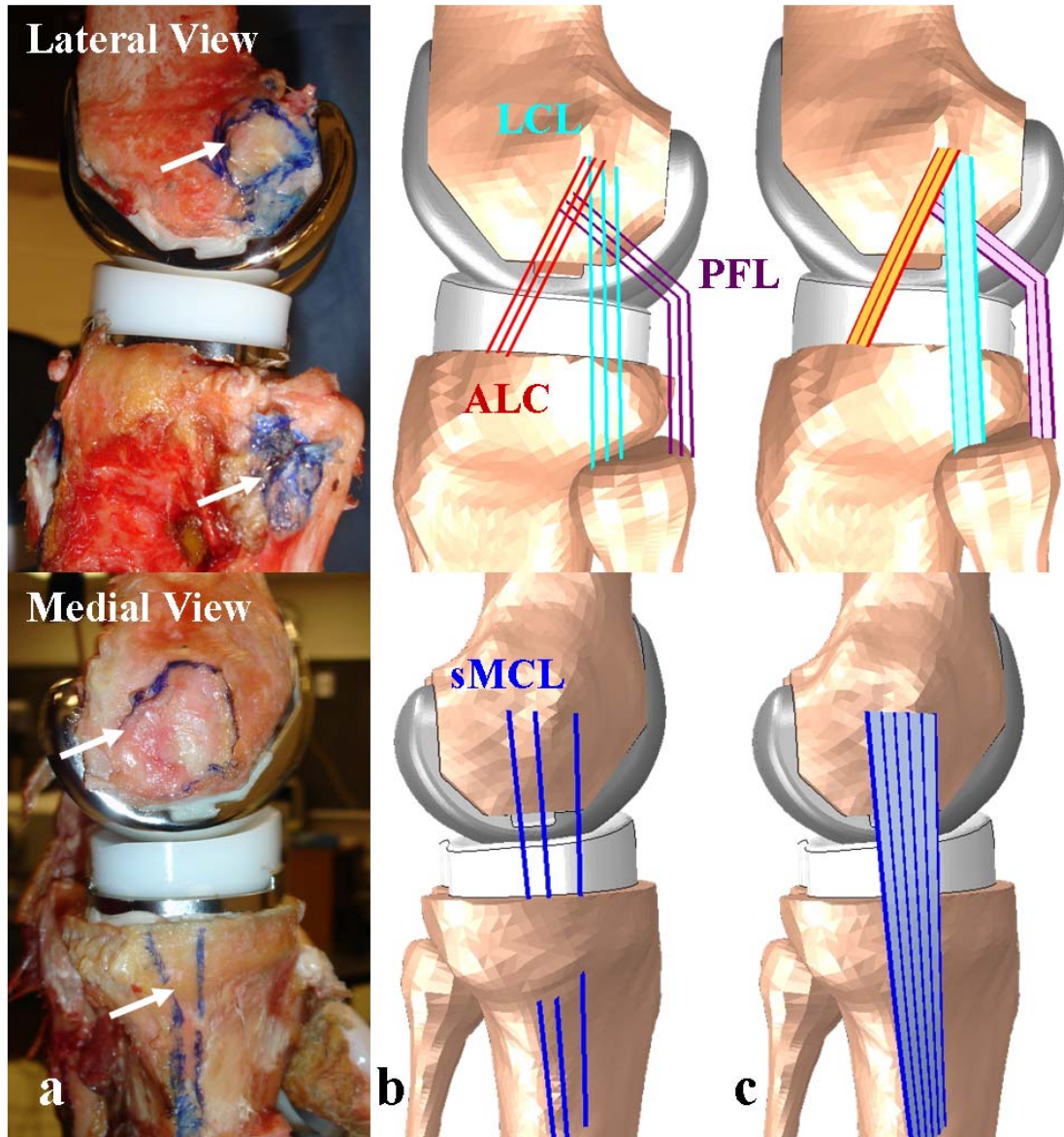
Figure 7.2 (a) Medial and lateral views of dissected specimen with outlined collateral bony attachment areas (arrows), (b) computationally efficient spring representation for phase I optimization, and (c) 2D fiber-reinforced representation for phase II optimization.
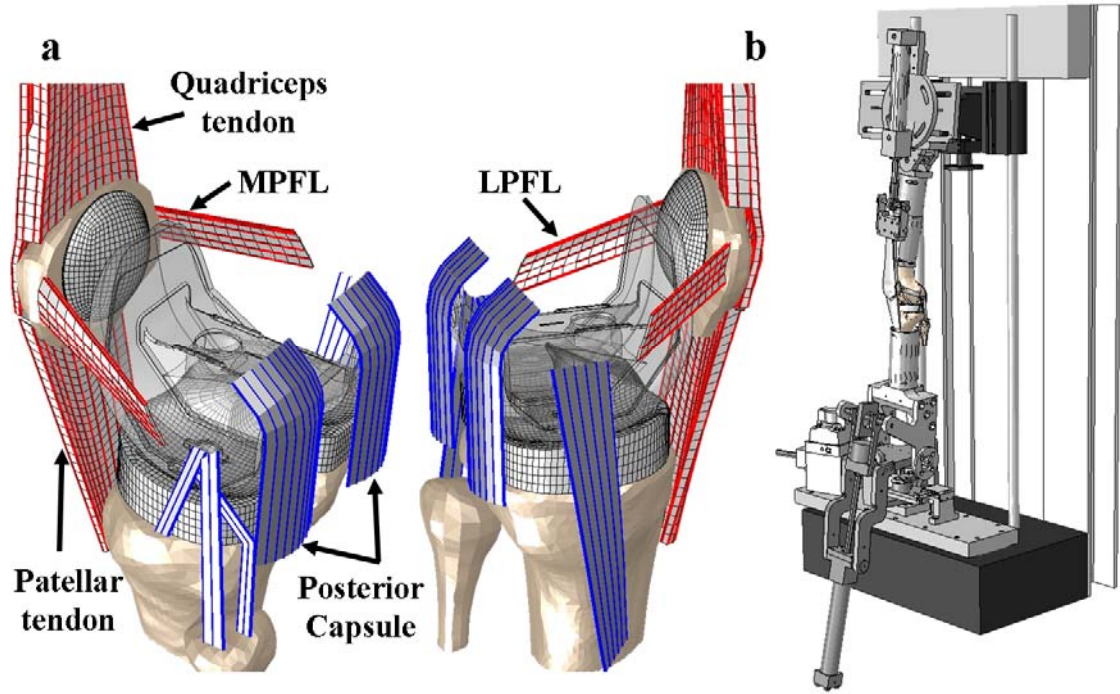
Figure 7.3 (a) Specimen-specific implanted model with 3D extensor mechanism structures (red) and optimized tibiofemoral ligaments (blue); (b) finite element model of KKS setup.
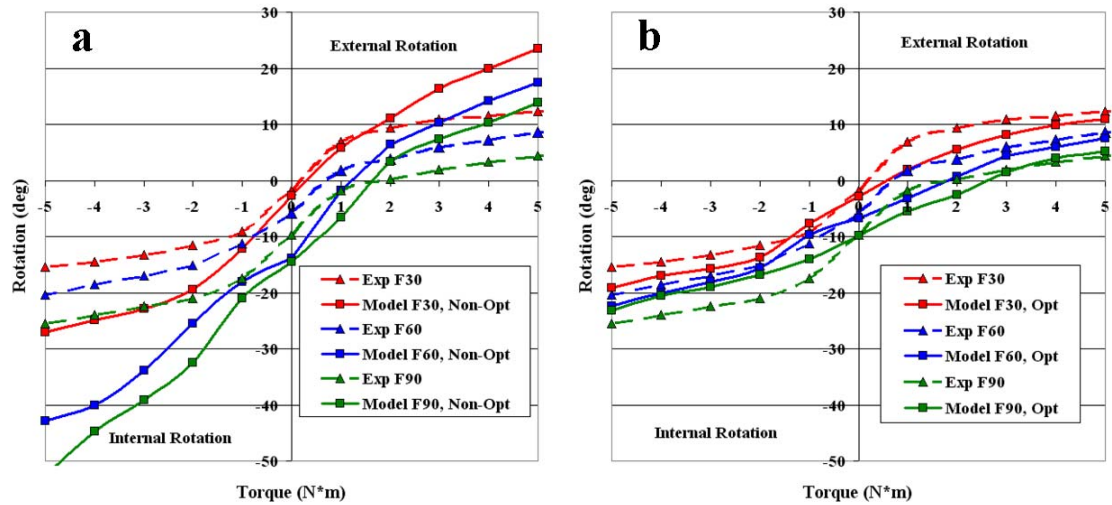
Figure 7.4 Single specimen internal-external experimental and model-predicted torque-rotation responses at 30, 60, and 90° with (a) non-optimized and (b) optimized constraint.
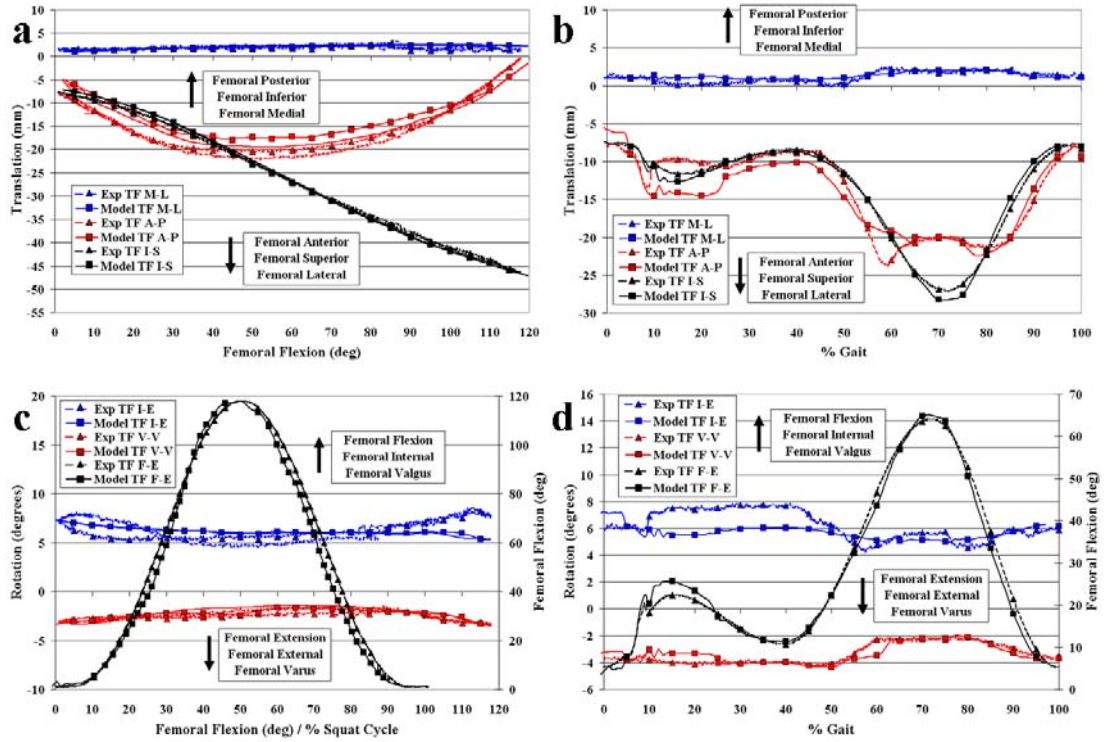
Figure 7.5 Single specimen experimental and model-predicted tibiofemoral translations and rotations in the simulated deep knee bend (a, c) and gait (b, d) activities, respectively.
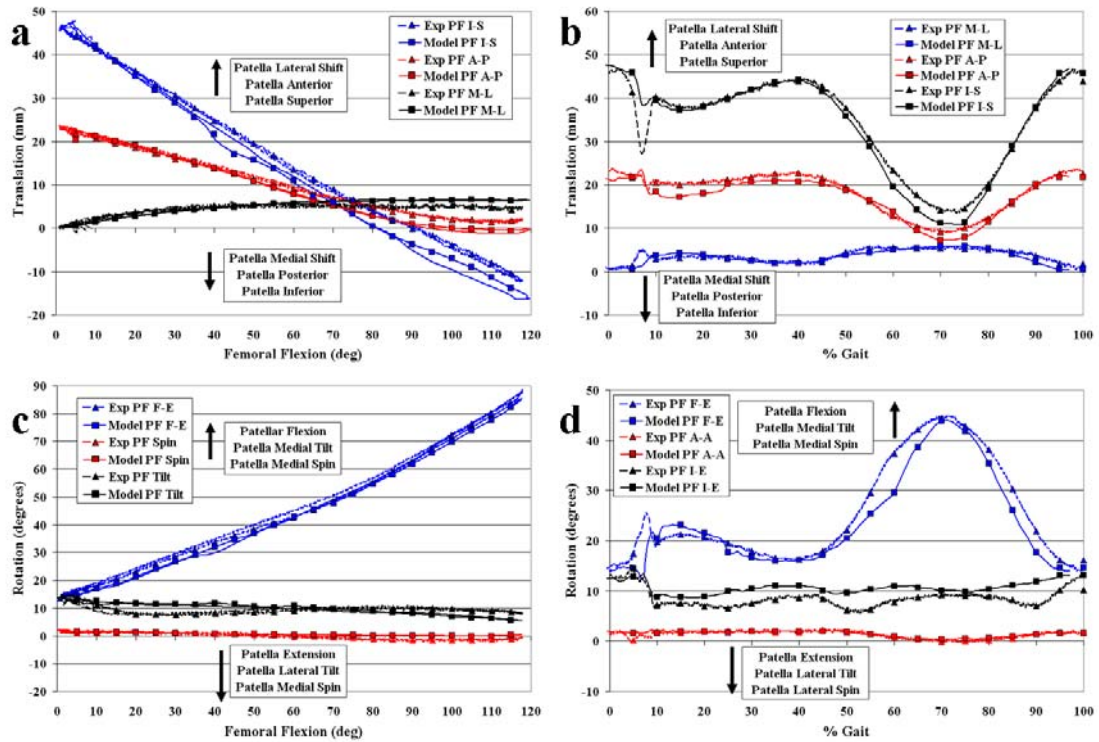
Figure 7.6 Single specimen experimental and model-predicted patellofemoral translations and rotations in the simulated deep knee bend (a, c) and gait (b, d) activities, respectively.
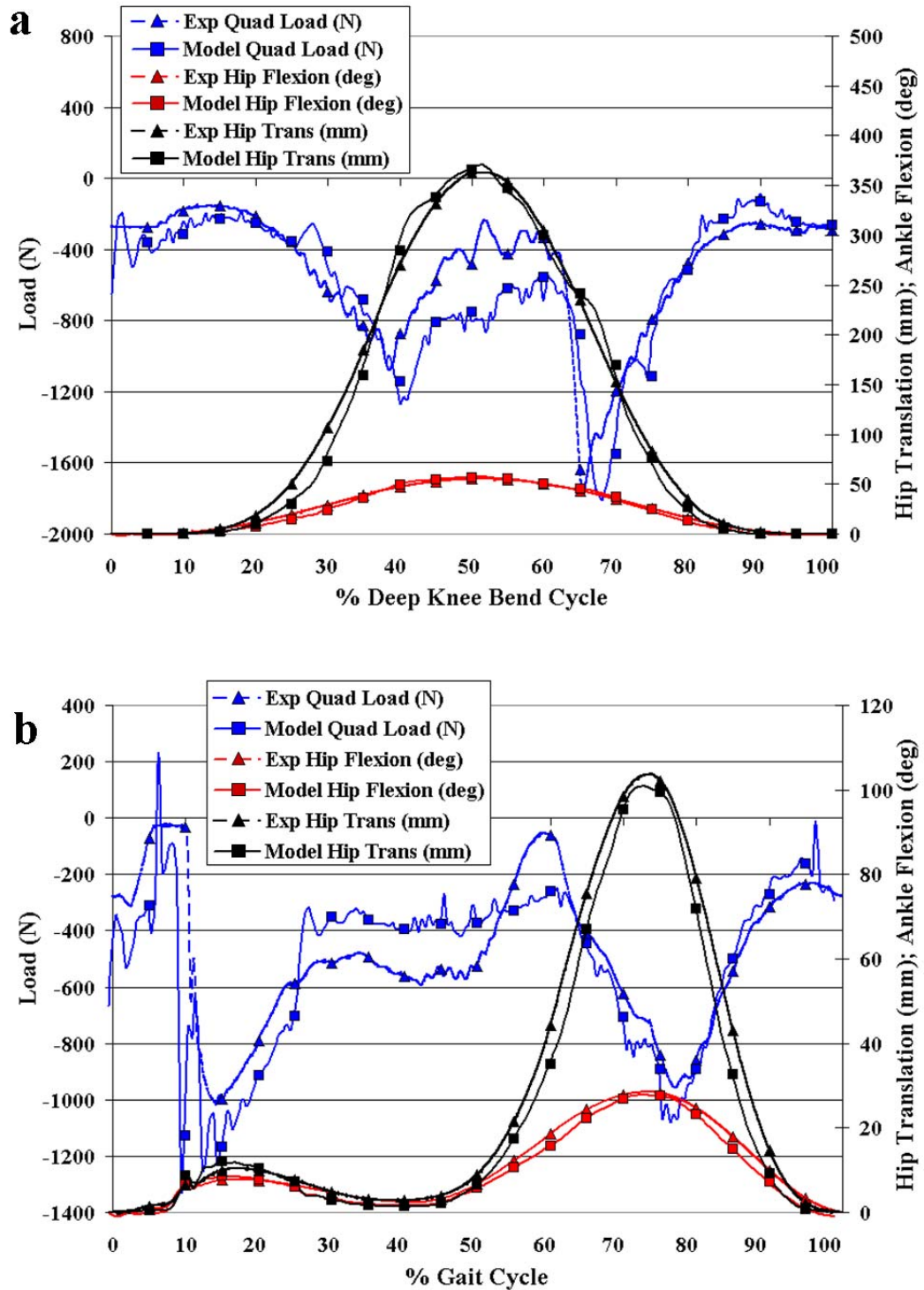
Figure 7.7 Single specimen experimental and model-predicted ankle flexion, hip translation, and quadriceps load in the simulated deep knee bend (a) and gait (b) activities; average RMS differences across all four specimens in parentheses.
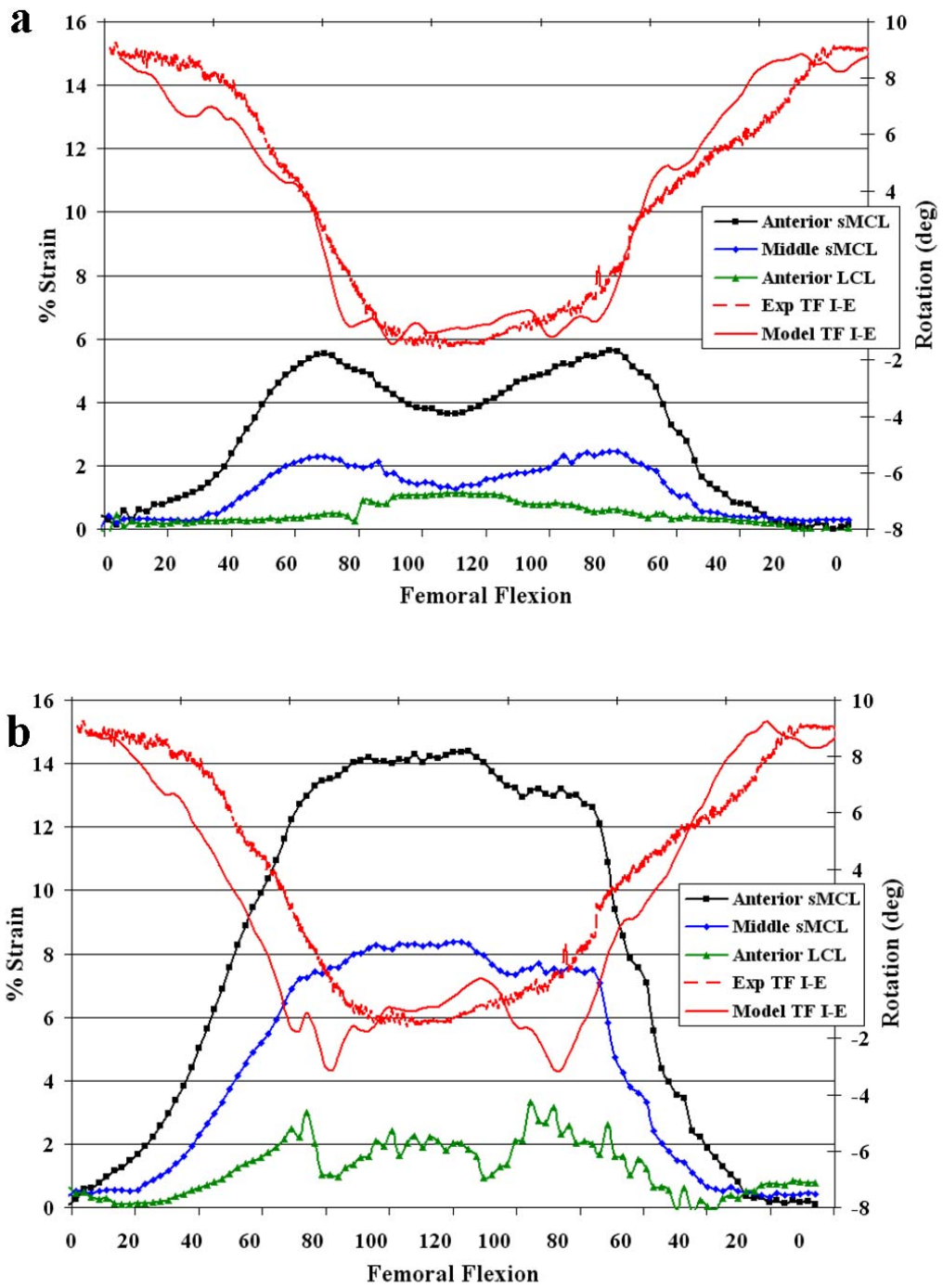
Figure 7.8 Representative localized collateral ligament strains and tibiofemoral I-E rotations for a single specimen using optimized (a) and non-optimized (b) parameters during a deep knee bend activity.

Table 7.1 Average RMS differences between predicted and experimental kinematics and actuator responses.

Output	Deep Knee Bend	Gait	Both
Tibiofemoral F-E (deg)	4.0 ± 0.8	2.7 ± 0.6	3.4 ± 0.9
Tibiofemoral V-V (deg)	0.9 ± 0.5	0.7 ± 0.3	0.8 ± 0.4
Tibiofemoral I-E (deg)	1.5 ± 0.4	2.2 ± 1.8	1.8 ± 1.3
Tibiofemoral M-L (mm)	0.6 ± 0.1	0.7 ± 0.5	0.7 ± 0.4
Tibiofemoral A-P (mm)	1.8 ± 0.8	2.7 ± 0.2	2.3 ± 0.7
Tibiofemoral I-S (mm)	1.2 ± 0.7	1.2 ± 0.6	1.2 ± 0.6
Patellofemoral F-E (deg)	2.9 ± 1.1	3.2 ± 0.5	3.0 ± 0.8
Patellofemoral Spin (deg)	1.7 ± 0.7	0.8 ± 0.5	1.2 ± 0.7
Patellofemoral Tilt (deg)	2.4 ± 0.2	2.7 ± 1.1	2.6 ± 0.8
Patellofemoral M-L (mm)	1.4 ± 0.3	1.0 ± 0.5	1.2 ± 0.4
Patellofemoral A-P (mm)	1.8 ± 0.7	1.2 ± 0.4	1.5 ± 0.6
Patellofemoral I-S (mm)	3.1 ± 1.1	1.9 ± 0.5	2.5 ± 1.0
Quad Load (% of Peak)	17.7 ± 6.5	20.1 ± 8.2	18.9 ± 7.0
Hip Flexion (% of Peak)	4.6 ± 0.9	6.6 ± 1.5	5.6 ± 1.6
Hip Translation (% of Peak)	4.1 ± 1.1	5.6 ± 2.3	4.9 ± 1.9
Ankle Flexion (% of Peak)	5.0 ± 0.5	6.8 ± 2.6	5.9 ± 1.9

CHAPTER 8. EVALUATION OF POSTERIOR-STABILIZED TENDOFEMORAL

CONTACT DURING SIMULATED DEEP SQUAT

8.1. Background and Relevance

The following study represents a clinical application of the previously described KKS model as a result of direct collaboration with surgeons and orthopedic manufacturers who have identified a clinical complication related to a particular implant design type. This study exemplifies the utility of computational models in providing insight into the mechanism of a physical occurrence that would otherwise be difficult to evaluation experimentally or in the TKA patient population.

8.2. Introduction

Irritation of the quadriceps tendon in the suprapatellar region is a complication associated with posterior-stabilized (PS) implants following total knee arthroplasty (TKA) (Pollock et al., 2002). In some cases, tendon inflammation leads to growth of a fibrous mass or nodule that can be trapped in the intercondylar box during active leg extension causing an audible clunking sound and potentially patient discomfort (Beight et al., 1994; Hozack et al., 1989). The etiology of this inflammation has been attributed to a number of factors including prosthetic design, component alignment, alteration of the joint line, patellar height, and patellar tracking (Anderson et al., 2008; Maloney et al., 2003; Ranawat et al., 2006; Yau et al., 2003). Clinical observations have suggested

the quadriceps tendon may contact the anterior border of the femoral component intercondylar box during deeper flexion (Hozack et al., 1989; Pollock et al., 2002), and several studies have shown box dimensions to be a contributing factor in crepitation (Maloney et al., 2003; Yau et al., 2003). Despite these observations, it is still unclear what aspects of anatomic variation and component alignment may increase the potential for box-to-tendon contact potentially leading to crepitation.

Computational models represent an efficient platform for investigating complications in the implanted knee, especially related to component alignment and design. Previous computational studies have investigated various aspects of component placement (D'Lima et al., 2003; Heegaard et al., 2001; Kessler et al., 2008) and quadriceps load distribution (Dhaher and Kahn, 2002; Elias et al., 2006) on predicted kinematics and contact mechanics, but to our knowledge, no study has specifically investigated tendofemoral contact related to the PS implanted knee. The finite element (FE) method is well suited for evaluating crepitation through the use of deformable, three-dimensional (3D) representations of extensor mechanism structures articulating over a PS femoral component surface. This type of analysis could be utilized to investigate the relationship between component placement and patellar height and tendon-to-box articulations as a potential indicator for crepitation.

Accordingly, the objective of the present study was to determine the influence of patellar ligament length and alignment of the patellar and femoral components on tendon articulations, tendon-to-intercondylar box spacing, and patellar flexion during a simulated deep knee bend activity using a specimen-specific finite element model of a

PS implanted knee. Specifically, discrete perturbations in component placement and patellar ligament length were performed using a previously verified force-driven dynamic model (Chapter 7) under experimentally measured hip and ankle loads between 10 and 120° femoral flexion. Tendofemoral articulation was defined by a cumulative region of tendon-to-femoral component contact area summed over the entire range of flexion and extension. Tendon-to-box spacing was measured in the sagittal plane as the minimum distance between the anterior-most edge of the intercondylar box and quadriceps tendon.

8.3. Methods

8.3.1. Model Development

A specimen-specific 3D dynamic, explicit FE model of an implanted cadaver knee was developed in Abaqus/Explicit^{TM} 6.8.1 (Dassault Systemes, Providence, RI) to evaluate tendofemoral articulation during a simulated deep knee bend activity. Prior to model development, an *in-vitro* experiment replicating a deep knee bend activity in a mechanical simulator was conducted on an implanted cadaveric specimen. A fresh-frozen cadaver knee harvested from an intact lower limb was implanted by an orthopedic surgeon with a posterior-stabilized (PS) total knee prosthesis for experimental testing. Tibial and femoral bones were potted in aluminum fixtures and mounted in the Kansas knee simulator (KKS) with the quadriceps tendon rigidly attached to a linear actuator aligned to the femoral long axis. The implanted knee was flexed and extended up to 120° flexion to simulate a deep knee bend activity under applied ankle and hip loads and translation of the quadriceps actuator.

A 3D model of the implanted knee was developed by extracting femoral, patellar, and tibial bony surfaces from magnetic resonance (MR) scan data using ScanIP (Simpleware, Exeter, UK) and aligning computer aided design surfaces of size-matched PS components to the bones via experimental point data (Figure 8.1). A rigid body model of the KKS was developed to reproduce experimental loading and boundary conditions of the deep knee bend activity (Figure 8.1) with the implanted knee model aligned to the experimental initial position. To evaluate tendon articulation over the femoral PS component, a fiber-reinforced soft tissue model was adopted to represent extensor mechanism structures (Baldwin et al., 2009b). Length, width, and thickness of the cadaver patellar ligament (PL), rectus femoris (RF), and vastus intermedius (VI) tendons were determined from MR scans and represented as 3D deformable structures attached to the tibial and patellar bones in the model. Additional structures representing medial and lateral patellofemoral ligaments were also included with literature-based attachments and dimensions (Amis et al., 2003b; Smirk and Morris, 2003). Mechanical properties for all soft tissue structures were tuned to match uni-axial force-deflection responses in separate analyses (Atkinson et al., 2000; Stäubli et al., 1999). Two-dimensional medial, lateral, and posterior capsular structures crossing the tibiofemoral joint were also included to maintain joint constraint throughout the simulated deep knee bend activity (Figure 8.1). Contact was defined between all soft tissue and bony or implanted surfaces for wrapping in deeper flexion. A previous verification study demonstrated model-predicted 3D patellofemoral and tibiofemoral kinematics to be within 3 mm and 3° of experimental measurements during a simulated deep knee bend (Baldwin et al., 2009a).

8.3.2. Model Perturbations

An initial radiographic study was conducted on groups (N=20) of patients with and without evidence of crepitation following PS TKA to determine magnitudes of discrete changes in patellar ligament length and patellar and femoral component alignment perturbations for a design of experiments analysis. Based on observed patient variability, the patellar ligament length was increased or decreased by 10 mm from the original specimen length (Neutral state) to represent patients with patellar alta and baja, respectively. With the patellar bone in the neutral position, the domed component placement was perturbed superiorly and inferiorly (Pat I-S) by 5 mm and separately flexed and extended (Pat F-E) by 10° on the resection plane about a local patellar medial-lateral axis. Femoral component alignment was also perturbed by flexing and extending (Fem F-E) 10° about the femoral medial-lateral axis (Figure 8.2).

Potential for crepitation was measured for each perturbed state as a function of tendofemoral contact, tendon-to-intercondylar box gap, and patellar flexion over the deep knee bend cycle. Tendofemoral contact was defined by the cumulative region of tendon contact area on the femoral component summed over all flexion angles throughout the knee bend activity. Tendon-to-box spacing was determined by the minimum distance between the anterior border of the intercondylar box and the suprapatellar tendon in the sagittal plane (Figure 8.2). Patellar flexion was calculated with respect to the femur using a three-cylindrical description of joint motion (Grood and Suntay, 1983).

8.4. Results

Tendon contact showed consistent patterns across all perturbations with consistent contact along the ridges of the femoral component and an arcing pattern in the groove (Figure 8.3). Increasing patellar ligament length (alta), superiorizing or extending the patellar component and flexing the femoral component resulted in contact regions further from the anterior edge of the intercondylar box when compared to the neutral model (Figure 8.4). Conversely, shortening the patellar ligament length (baja), inferiorizing or flexing the patellar component, and extending the femoral component caused contact regions to be closer to the intercondylar box. The most substantial differences were noted in the patellar alta and baja models with no mid-sagittal tendon contact in the alta model and contact directly along the anterior intercondylar edge in the baja model.

In the sagittal plane, minimum box-to-tendon distance was found to be 1.9 mm in the neutral state with the greatest and least distance occurring in the alta (4.7 mm) and baja (0 mm) models, respectively. Superiorizing the patellar component by 5 mm and flexing by 10° increased box-to-tendon distances to 2.2 mm; inferiorizing by 5 mm reduced box-to-tendon distance to 1.5 mm; extending the patella by 10° showed no change from the neutral state. Femoral component flexion increased tendon-to-box distance to 2.9 while extending decreased it to 2.2 mm. Patellar flexion with respect to the femoral component was most affected by changes in patellar ligament length (up to 12° difference) and relatively unaffected by patellar and femoral component alignment.

8.5. Discussion

Complications of the implanted PF joint are among the most common causes of TKA failure (Brick and Scott, 1988; Meding et al., 2008) and include anterior knee pain, impingement, fracture, dislocation and crepitation. Irritation of the quadriceps tendon in the suprapatellar region causing crepitation is a complication found primarily following PS TKA. The progression of this condition to a fibrous nodule can create a painful catching in the intercondylar box which typically requires subsequent surgical removal (Beight et al., 1994; Hozack et al., 1989). Although the etiology of crepitation is likely multi-factorial, clinical evidence has implied crepitation is related to contact between the anterior edge of the intercondylar box and quadriceps tendon. To investigate this relationship, the current computational study utilized a specimen-specific whole joint implanted cadaveric model to track articulation of a deformable 3D quadriceps tendon over a PS femoral component surface during a simulated deep knee bend activity. The model showed strong correlations to experimental kinematic tibiofemoral and patellofemoral measurements (root mean square differences of less than 3 mm and 3°), making it a suitable platform to investigate the effect of perturbations in patellar ligament length and implant component alignment on tendon articulation and sagittal plane tilt.

With the selected level of discrete anatomic and component alignment perturbations, the most influential factor affecting tendofemoral contact, tendon-to-box spacing, and patellar flexion was patellar height. A shortened patellar ligament, simulating patellar baja, caused the suprapatellar quadriceps tendon to directly contact

the anterior edge of the intercondylar box in deep flexion (no box-to-tendon spacing) and reduced patellar flexion. This is consistent with the clinical findings of Yau et al. who demonstrated that a low-lying patella was significantly related to patellar clunk syndrome, a common progression of crepitation, in a study group of 236 PS TKA patients (Yau et al., 2003). In this model, the tendon-to-box contact occurred in deeper flexion (> 90º), which is in agreement with Pollock et al. who found that crepitation occurred in PS TKA patients during activities with deeper knee flexion, such as rising from a sitting position, but not during walking (Pollock et al., 2002).

Component alignment perturbations resulted in smaller but clear changes to the resulting tendofemoral contact locations and kinematics. Superiorizing the patellar component or extending the resection plane with respect to the femur was found to increase the distance between the quadriceps tendon and anterior edge of the intercondylar box, increase the box-to-tendon gap in the sagittal plane, and increase patellar flexion. Both alignment perturbations cause the quadriceps to be elevated from the femoral surface in deeper flexion, moving tendon articulation away from the intercondylar box. Flexing of the femoral component with respect to the femur bone had a similar effect on tendon contact by moving the intercondylar box away from the quadriceps tendon in deep flexion. These results would suggest that patients who present a lower patellar height may need appropriate component placement that could increase the distance between the intercondylar box and quadriceps tendon in deeper flexion.

There are several limitations with the current approach that must be addressed. Although the KKS provides a suitable platform for computational assessment of whole joint mechanics, the simplified loading via the rectus femoris and vastus intermedius tendons may not fully capture the *in-vivo* interaction between the extensor hood and femoral component in deeper flexion. Future studies should include the longus and obliquus portions of the vasti tendon and flex or extend the leg under applied loads of the extensor muscle group. In addition, *in-vivo* PF kinematics derived from fluoroscopy of PS TKA patients performing high flexion activities (i.e. deep knee bend) could be used to assess tendofemoral contact under more physiologic loading. In this study, a single domed patellar component design and size was investigated with discrete changes in patellar height and component alignment. Additional evaluations could investigate tendon-to-box contact using different patellar component design types (i.e. anatomic) and sizes, with component overhang, and by changing the tibiofemoral joint line height (Yau et al., 2003). Lastly, future evaluations could also explore a more holistic spectrum of anatomic and component alignment perturbations via a probabilistic approach.

Elucidating the parameters affecting tendency for quadriceps tendon contact with the intercondylar box will aid in optimizing clinical outcomes for patients with PS TKA. Additionally, the current FE representation of the KKS mechanical simulator can provide insight into the potential effects of intercondylar box dimensions and position on tendon contact during the PS design phase.
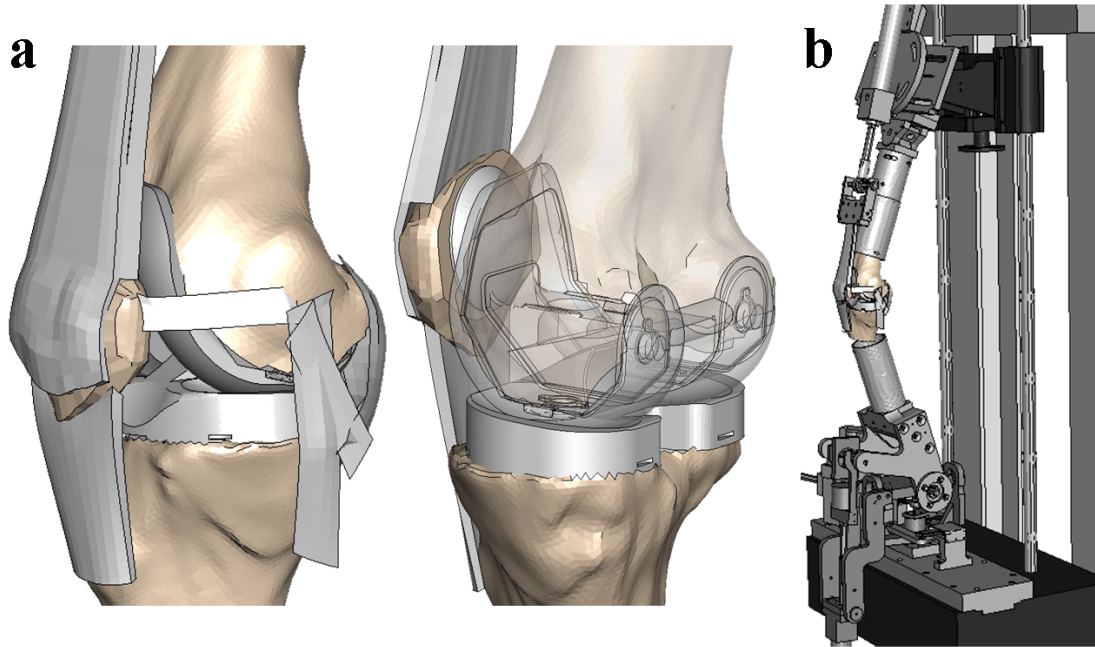
Figure 8.1 (a) Specimen-specific implanted knee model (b) Kansas knee simulator model.
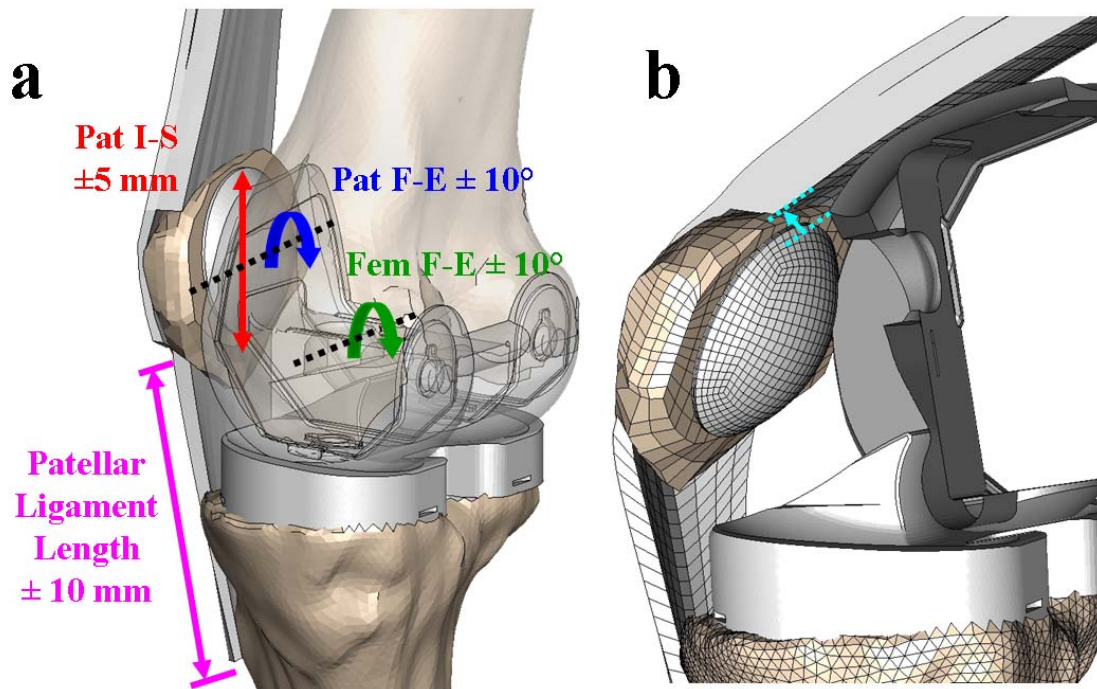
Figure 8.2 (a) Diagram of input parameter perturbations (b) illustration of minimum tendon-to-box spacing measurement.
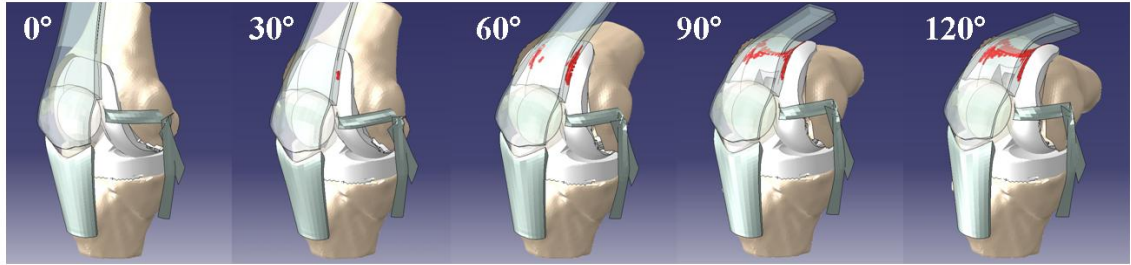
Figure 8.3 Tendon-to-femoral component contact throughout the range of flexion in the neutral implanted model.
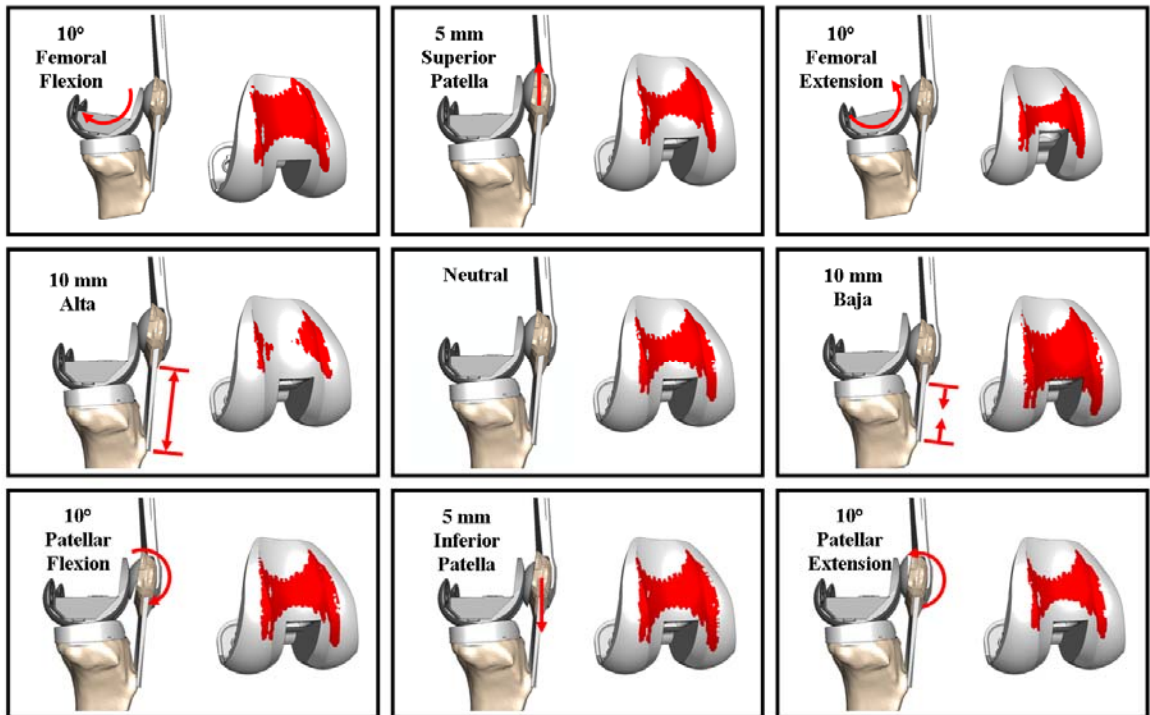
Figure 8.4 Cumulative tendon contact regions for perturbed models.

CHAPTER 9. DEVELOPMENT OF SUBJECT-SPECIFIC AND STATISTICAL

SHAPE MODELS OF THE KNEE USING AN EFFICIENT GEOMETRY

EXTRACTION AND MESH MORPHING APPROACH

9.1. Background and Motivation

The following study represents the initial stages of applying the previously described methods for modeling the implanted knee to the more complex natural knee. Previous natural knee modeling efforts were deliberately simplified in scope, such as with the isolated patellofemoral study, to limit the number of unknown variables within the model. These types of isolated compartment studies are valuable as a means to compare pre- and post-TKA joint mechanics for a particular compartment, but the knee functions as an interrelated tri-compartmental system that must be considered as a whole to capture the relationship between articular surfaces, soft tissue constraint, and applied muscle loads.

As an initial step towards muscle-driven models of the natural knee, the current study focused on efficient extraction of the natural articular surfaces from magnetic resonance images. The purpose was to reduce the laborious and difficult process of generating specimen-specific 3D hexahedral meshes of natural articular surfaces and to simplify the process through the use of a custom-built interface. The methods presented here are the first steps towards efficiently generating a "population" of natural knee models based on principal component analysis and mesh-morphing methods.

9.2. Introduction

Subject-specific finite element (FE) models incorporating anatomical articular cartilage surfaces and soft tissue geometric representations can provide insight into knee mechanics for healthy normal and pathologic conditions (Pena et al., 2006; Suggs et al., 2003; Yao et al., 2006). Accurate predictions of knee joint mechanics in FE models depends on multiple factors including appropriate representations of the geometry, properties of anatomic structures and the application of boundary conditions (i.e. kinematics and muscle forces) (Besier et al., 2005b). Segmentation of computed tomography (CT) and magnetic resonance (MR) scan data has become the accepted standard for subject-specific model development (Cohen et al., 1999; McGibbon, 2003). However, the processing is typically manual and time consuming, requiring approximately two days of work to extract the articular layers of a knee joint (Cohen et al., 1999). In addition, model development time is increased with the meshing of segmented surfaces into 3-D hexahedral solids, which are recommended for accurate FE representations for bone strain (Viceconti et al., 1998) and contact (ABAQUS, 2006). The hexahedral meshing process is also manual and often requires advanced knowledge of mesh generation techniques (Muccini et al., 2000).

Recently, statistical shape models have been demonstrated for bony geometries (Barratt et al., 2008; Bredbenner and Nicolella, 2008; Bryan et al., 2008; Rajamani et al., 2007) with the potential to efficiently generate a patient-specific model from anatomical measurements for use in computer-assisted surgery (CAS) or to create a simulated population of subjects for assessment of implant design. Statistical shape

modeling involves a principal component analysis (PCA) performed on a training set of extracted subject geometries to determine the modes of spatial variation (Barratt et al., 2008; Bredbenner and Nicolella, 2008; Bryan et al., 2008; Rajamani et al., 2007). In addition to manually segmenting the geometries to form the training set, a traditional challenge in statistical shape modeling is that registration, a correspondence of the landmark locations (mesh nodes) for each instance in the training set, requires implementation of custom algorithms and can be computationally expensive (Barratt et al., 2008; Bredbenner and Nicolella, 2008; Bryan et al., 2008; Rajamani et al., 2007).

To address these issues of model development efficiency, recent studies have investigated various aspects of automating the model development process. Automated threshold-based algorithms have been employed to extract bones from CT scans (Taddei et al., 2006; Testi et al., 2001), however, these techniques have not been successfully applied to soft tissue structures (e.g. cartilage, ligaments) from MR scans. Another common approach is to use traditional segmentation of CT images to generate a 'target' surface and to automate the mapping of a template mesh to fit the subject-specific segmented surfaces (Besier et al., 2005b; Couteau et al., 2000; Fernandez et al., 2004; Grosland et al., 2008; Kallemyn et al., 2007; Keyak et al., 1990; Shim et al., 2007; Sigal et al., 2008).

The current study enhanced the model development efficiency by proposing an integrated extraction and hex meshing approach that is applicable to structures in both CT and MR scans, has accuracy similar to manual extraction techniques, and can streamline statistical shape modeling by utilizing mesh control points from the extracted

geometry. Accordingly, the objectives of the current study were: 1) to develop an efficient, integrated mesh-morphing-based extraction approach to create hexahedral meshes of subject-specific geometries from scan data and to apply the approach to natural knee femoral, tibial, and patellar articular surfaces from MR images, 2) to compare geometries and predicted contact results from a quasi-static FE analyses between meshed surfaces using the semi-automated approach and traditional segmentation, and 3) to demonstrate a statistical shape model of the knee characterizing the modes of variation using PCA.

9.3. Methods

9.3.1. Integrated Extraction and Mesh Morphing Platform

The integrated platform utilized a custom graphical user interface (GUI) and required a template mesh for each structure. The template mesh, developed using the traditional approach of manually segmenting (ScanIP, Simpleware, Exeter, UK) and meshing the structures of interest for a single subject, was used for morphing the geometries of subsequent subjects. Mesh morphing of the template was conducted using built-in Hypermesh (Altair, Inc., Troy, MI) features that maintained internal element quality (i.e. size and skewness) after mesh manipulation. To prepare for morphing a structure, the template mesh was subdivided into sets of contiguous elements to create groups (domains) bounded by control points (handles) on the group corners (Figure 9.1). Displacing control handles linearly redistributed internal nodes between the final handle positions within each domain (Figure 9.1). Each meshed structure was subdivided into domains and attempted to minimize the number of control

handles required to identify anatomic borders while maintaining enough resolution to capture geometric changes.

The GUI was developed in Matlab (Mathworks Inc., Natick, MA) to display a series of sagittal MR images and overlay sets of moveable points corresponding to the coordinates of the template mesh control handles. The GUI was subdivided into five sections to guide user operations: 1) general image and scan information input fields, 2) contour identification for patellar, tibial, and femoral structures, 3) a preview panel to show existing points located on previous images, 4) a mesh preview panel to orient the user to the location of the displayed sagittal slice on the template mesh, and 5) the current sagittal image (Figure 9.2). Mesh morphing with the GUI was initiated by specifying image details (e.g. field-of-view dimensions, image resolution, leg side, scanned flexion angle) to convert control handle coordinates from "mesh" space to image "scan" space (i.e. 512 x 512 pixels). The medial- and lateral-most images associated with visible borders of each structure are then used to scale the template meshes and redistribute control handles along the medial-lateral direction. Points corresponding to template mesh control handles are overlaid on the displayed sagittal images and manually manipulated to identify the perimeter of the desired anatomic structure (Figure 9.3). Once a structure was completely outlined, point coordinates were smoothed by fitting piecewise polynomials (2nd-4th order) in the sagittal, coronal and frontal planes minimizing the root-mean-square error between smoothed and identified handle coordinates. Differences between the initial template and final smoothed point coordinates were exported as morphing commands automatically executed on the template mesh within Hypermesh.

9.3.2. Application to Structures of the Knee

To evaluate the capabilities of the semi-automated platform, models of the femoral cartilage, medial and lateral tibial cartilage, and patellar bone and cartilage were developed from sagittal MR scan data (512 x 512 pixels, slice thickness between 1 and 1.5 mm) for 10 healthy normal subjects. Template meshes for the articular cartilage were created from one segmented knee geometry (Figure 9.4); 3D hexahedral elements were used with an average edge length of approximately 2.5 mm and three elements between the articulating and bony sides. The patellar bone was meshed with 2D shell elements and included in the template set to allow attachment and wrapping of the extensor mechanism soft tissue structures for patellofemoral analyses. The template femoral mesh was subdivided into medial and lateral condylar and notch regions to manage geometric discontinuities and adapt mesh resolution to curvature changes (Figure 9.4). Specifically, curvature along the medial-lateral axis in the condylar regions was more gradual than in the notch and, therefore, domains were spaced at 6 mm intervals compared to 3 mm intervals in the notch region. Otherwise, all elements were aligned to a global "sagittal" plane and spaced along the medial-lateral direction at constant 3 mm intervals. The number of elements and control points varied for each structure and totaled approximately 5,500 hexahedral elements with 817 control points (Table 9.1). Once the template mesh was developed, the GUI was used to position the control points in the displayed sagittal MR image for the other subjects.

9.3.3. Efficiency and Accuracy of Geometry and Contact Mechanics

The accuracy of the current semi-automated method was evaluated by comparing control point coordinates and predicted contact mechanics between the GUI-generated hexahedral meshes and articular surfaces generated via traditional segmentation for three subjects (Figure 9.4). For comparison purposes, the traditional segmented geometry was represented by a template geometry with control handles positioned to match the segmented surfaces for each structure. Accuracy of the geometry was evaluated by calculating root mean square (RMS) differences in the coordinate positions of the control points; RMS differences were averaged for each structure and across the three subjects. To quantify efficiency, the average time required to generate hexahedral meshes of all structures was recorded for both the semi-automated and traditional manual methods.

The effect of the model development methods on predicted contact mechanics was evaluated through a series of quasi-static FE analyses. FE models were developed in Abaqus/Explicit^{TM} 6.7-1 (Dassault Systemes, Providence, RI) using the semi-automated and traditional segmentation approaches. A ramped load (up to 700 N for tibiofemoral and 350 N for patellofemoral contact) was applied normal to the patellar and tibial surfaces to contact the femoral cartilage at fixed tibiofemoral flexion angles of 0°, 30°, 60°, and 90°. Each articular structure was a deformable, linear elastic material with a modulus of 6 MPa and Poisson's ratio of 0.47 (Besier et al., 2005b). Model-predicted peak contact pressures and contact areas were calculated for each meshed structure and compared over the specified flexion angles.

136

9.3.4. Statistical Shape Modeling

The integrated extraction, mesh-morphing platform provided the added benefit of a standardized set of 3D meshes, which were used to develop a statistical shape model. Typically, a registration process is required to identify the nodal locations on the segmented surfaces. With the current approach, the control points were used as the parameters to define the statistical shape model. A PCA was performed on the 3D coordinates of each control point for the femoral (1670 control points), medial (168) and lateral (144) tibial, and patellar articular surfaces (150) and patella (135) (Figure 9.4) to characterize the variability in the training set of 10 subjects. Individual geometries were aligned to a common origin on the tibia. PCA reduces the dimensionality of a data set with a large number of variables to a small number of variables that retain a pre-defined fraction (e.g. 95%) of the variation present in the data set (Jolliffe, 2002). The result of the eigen-based PCA is a statistical shape model defined by a series of modes of variation represented by the principal components or eigenvalues. The individual modes of variations define the variations in size, location and shape of the structures and when linearly superposed represent the overall variability.

9.4. Results

Hexahedral meshes of femoral, tibial, and patellar articular surfaces were successfully generated using the integrated extraction, mesh-morphing approach on MR data from 10 subjects. Accuracy of the extracted geometry was evaluated by comparing geometric differences between the semi-automated and traditional manual approaches

for three subjects; average RMS differences across all articular geometries were $0.54 \pm$ 0.32 (S.D.) mm and are reported in Table 9.2 for each structure and subject. Creating a complete set of 3D hexahedral meshes on a single specimen using the GUI-based method required an average of 1.5 hours for each of the 10 specimens in the PCA training set, compared to 16-32 hours for traditional segmentation and meshing, depending on the expertise of the analyst.

Results from the quasi-static FE contact analyses showed relatively small differences between the semi-automated and manually generated meshes at various femoral flexion angles. Average differences in model-predicted peak contact pressure and area predictions across all structures were less than 0.16 (5.3 %) MPa and 24.4 (4.7 %) mm^2 at the four flexion angles investigated (Figure 9.5).

Uniformity of the template mesh allowed for the efficient creation of statistical shape models for the articulating surfaces from the set of morphed mesh geometries. The PCA resulted in a series of principal components and corresponding eigenvectors indicating the direction of variation for each control point. The statistical shape model had 9 non-zero principal components with the first 5 modes representing 96% of the variability (Table 9.3). Modes of variation included a combination of size and shape changes, as well as positional alignment for the various structures (Figure 9.6). Mode 1, representing translation, rotation and femoral scaling, accounted for 52.4% of the variability. Mode 2 represented lateral condylar changes and inferior-superior translation of the patella. Modes 3 and 4 were primarily related to anterior-posterior and inferior-superior shape changes, respectively.

138

9.5. Discussion

Clinically relevant issues involving the natural knee, such as tibiofemoral osteoarthritis and patellofemoral pain syndrome, continue to warrant biomechanical evaluations to understand their etiology and potential intervention strategies (Besier et al., 2005b). The FE method has proven useful in understanding natural knee kinematics, contact mechanics, and internal stresses and strains (Mesfar and Shirazi-Adl, 2006b; Pena et al., 2006; Yao et al., 2006), but the extensive time required to generate specimen-specific hexahedral meshed articular surfaces, required for accurate contact prediction and joint representation, have typically limited study sample sizes and larger-scale clinical applicability. Segmentation performed on medical images is the current standard for generating 3D anatomic surface geometry, but the process is often time-consuming and the resulting meshes require additional processing for subsequent FE contact analyses. For these reasons, the objective of the current study was to develop an efficient integrated mesh-morphing-based extraction approach to create hexahedral meshes of subject-specific geometries from scan data. The approach was demonstrated in the natural knee femoral, tibial, and patellar articular surfaces from MR scan data, but the generalized approach can be easily applied to include other structures or types of scan data.

After development of the template mesh and GUI, the integrated extraction, mesh-morphing approach required ~1.5 hours to generate a complete set of 3D femoral, tibial, and patellar hexahedral meshes for each subject without the use of traditional segmentation or mesh pre-processing. Traditionally, extracting structures from MR

images via segmentation must be performed manually due to minimal differentiation in grayscale values between cartilage and surrounding structures and must be performed on each image to export a continuous surface. Depending on image spacing and complexity of the desired anatomic structure, this process can take many hours to complete, resulting in user fatigue and potential discontinuity in border identification. The current method expedited mesh generation by reducing the number of images required for border identification to approximately every 3 mm regardless of MR stack z-spacing and reduced the number of points required to manipulate (i.e. only 14 points per image for tibial cartilage) in order to identify anatomic borders. To maintain good mesh element quality, the template mesh set was pre-scaled to closely match the current geometry dimensions and displayed control points in the GUI were constrained along axes normal to the articular surfaces. Automating the process of morphing the template mesh set to the subject-specific geometry within Hypermesh eliminated the need for manual mesh pre-processing and made the final meshes directly exportable to FE solvers for contact analysis.

While the current approach improved the efficiency of model development, it was also critical to ensure that the resulting models were accurate representations of the anatomic structures. Accordingly, characterization of the uncertainty errors in geometry and finite element results was performed on a subset of three subjects. Using control point coordinates around the perimeter of each structure, the GUI-generated meshes differed from traditionally segmented surfaces by an average RMS difference of 0.54 mm and by less than 5.3% in predicted peak contact pressure and 4.7% in area predictions in quasi-static FE contact analyses over a range of flexion angles.

Comparing the accuracy and efficiency of the current method to previous attempts at automated mesh generation methods is difficult considering previous studies have mostly been applied to bones using computerized tomography (CT) datasets (Couteau et al., 2000; Grosland et al., 2008; Shim et al., 2007; Sigal et al., 2008; Viceconti et al., 2004) and controlled deformation of a template mesh to a "target" bony surface. While this type of deformation mapping has been shown to be accurate to fractions of a millimeter (Grosland et al., 2008; Sigal et al., 2008), the process still requires segmentation of CT images to acquire target surface geometry and has not been demonstrated on MR datasets. The accuracy of the current method is more appropriately compared to the approaches taken by Shim et al. and Fernandez et al. in which a desired anatomic structure was "seeded" with landmark points around the target surface boundaries and sub-sectioned into grids of higher order hermite elements connected through the 3D volume (Fernandez et al., 2004; Shim et al., 2008; Shim et al., 2007). Comparing their automated mesh generation techniques to target surfaces, Shim et al. reported RMS errors of less than 0.5 mm for a set of seven femoral and pelvis specimens when all image slices were utilized (Shim et al., 2007), while Fernandez et al. reported minimum RMS errors of 1.32 mm and 1.50 mm for single specimen rectus femoris and lung lobe geometries, respectively (Fernandez et al., 2004). The geometric uncertainties from this study were comparable to those reported by Shim et al. (2007) and additionally, the FE results were within the ranges of reported contact predictions at similar load levels (Besier et al., 2005a; Mesfar and Shirazi-Adl, 2005).

The subject-specific meshes developed using the semi-automated approach were seamlessly implemented as the training set for a statistical shape model. By using the mesh control points as the variables in the PCA, the registration process typically used in other studies (Barratt et al., 2008; Bredbenner and Nicolella, 2008; Bryan et al., 2008; Rajamani et al., 2007) was not required. The statistical shape model demonstrated how variation in both geometric shape and alignment position can be accounted for in multiple structures of the knee. The efficient implementation using MR images in contrast to prior CT-based studies will enable consideration of other soft tissue structures (ligaments and their attachments) in the future (Baldwin et al., 2009c). While all scans were in full extension, there was significant positional variation present, notably in patellar alignment (Figure 9.6). Using the demonstrated approach, the statistical shape model could be strengthened by using scan data from a greater number of subjects in a loaded, known position (Yao et al., 2008). Applied with correlations to anatomical measurements (Connolly et al., 2008), the statistical shape model can aid in CAS surgical planning, or as part of a probabilistic framework, can assess joint mechanics in a population of subjects.

In closing, this paper has detailed a novel integrated approach to perform extraction and meshing of knee structures from subject-specific scan data, with broad applicability to any joint. By integrating mesh morphing, the approach facilitated FE analysis and statistical shape modeling, which characterizes the modes of variation in a population of subject-specific models. The new approach, with improved efficiency and maintained accuracy, has the potential to increase the scale of subject-specific modeling studies, as well as to facilitate population-based joint mechanics evaluations.

Table 9.1 Element and control point information for the template meshes.

Structure	Number of Elements	Number of Control Points for GUI (for PCA)	Element type	Edge Length [mm]	Control points per slice (medial-lateral z-spacing)
Femoral Cartilage	2570	220 (1670)	3-D Hex	2.0-2.5	16 (6 mm) in condyles; 8 (3 mm) in notch
Medial Tibial Cartilage	825	168	3-D Hex	1.8	14 (3 mm)
Lateral Tibial Cartilage	990	144	3-D Hex	1.8	12 (3 mm)
Patellar Cartilage	500	150	3-D Hex	2.8	12 (3 mm)
Patellar Bone	600	135	2-D Shell	2.8	9 (3 mm)
Total	5485	817			

Table 9.2 Root mean square differences (millimeters) in mesh control point locations between the semi-automated approach and traditional manual segmentation.

	Subject			
	1	2	3	Mean (S.D.)
Femur	1.17	0.33	1.12	0.87 (0.47)
Medial Tibia	0.40	0.54	0.26	0.40 (0.14)
Lateral Tibia	0.42	0.25	0.45	0.37 (0.11)
Patella	0.40	0.33	0.86	0.53 (0.29)
Total				0.54 (0.32)

Table 9.3 Principal component modes and cumulative variability accounted for with inclusion of each mode.

Mode	1	2	3	4	5
Variability (%)	52.4	74.3	85.0	93.2	96.0
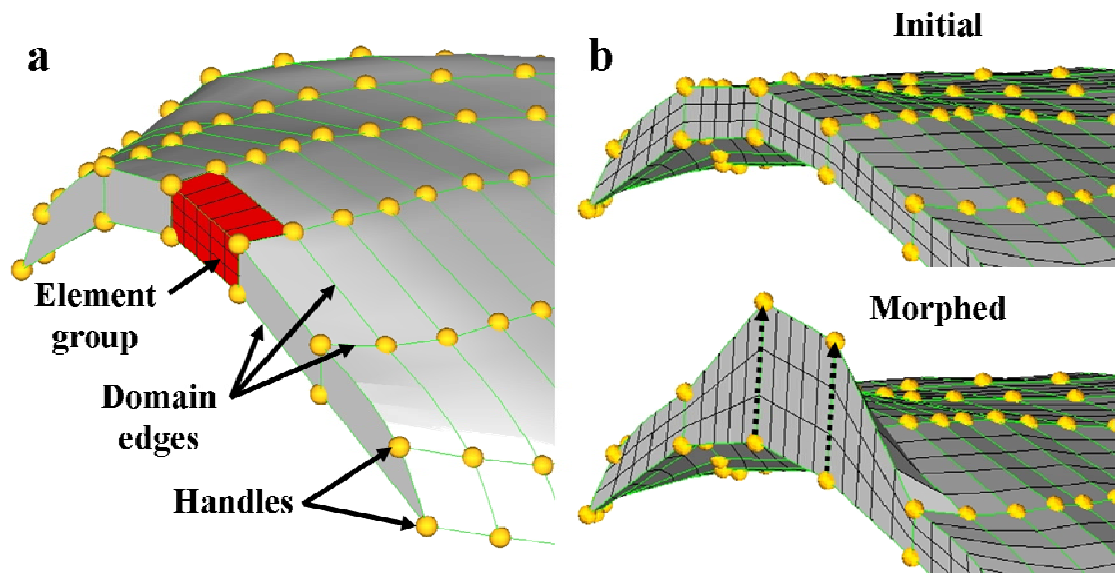
Figure 9.1 (a) Diagram depicting a template mesh element group, domains and control handles; (b) illustration of linear influence of internal nodes upon morphing.
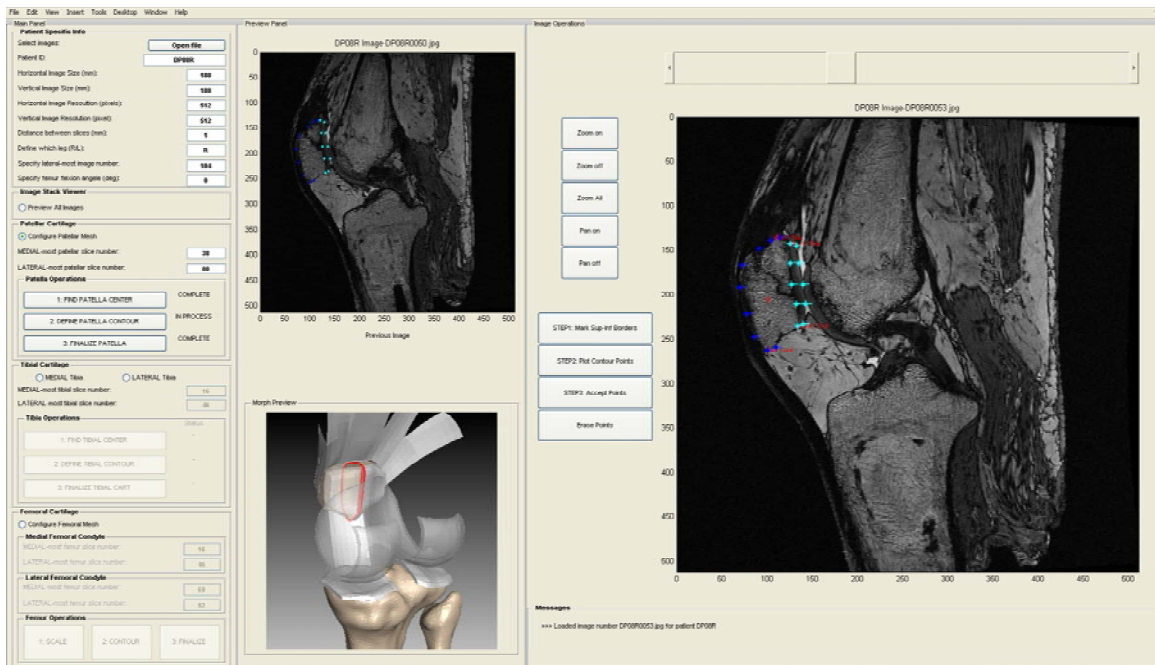
Figure 9.2 Graphical user interface (GUI) displaying MR image and control points for the patella.
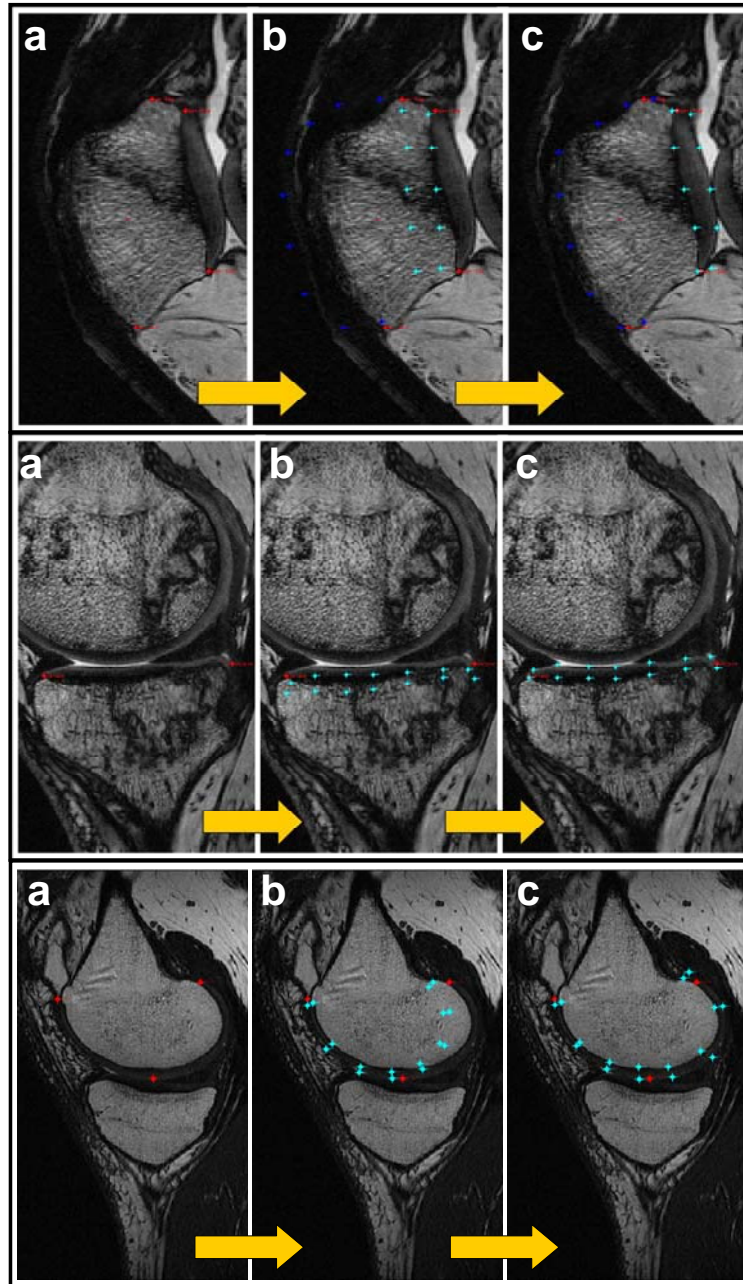
Figure 9.3 Identification of patellar (top), medial tibial (middle) and femoral (bottom) cartilage for a single subject; (a) identification of points (red) designating in-plane borders of anatomic geometry, (b) overlay of scaled template mesh control point locations (cyan), (c) contour points moved to structure boundaries.
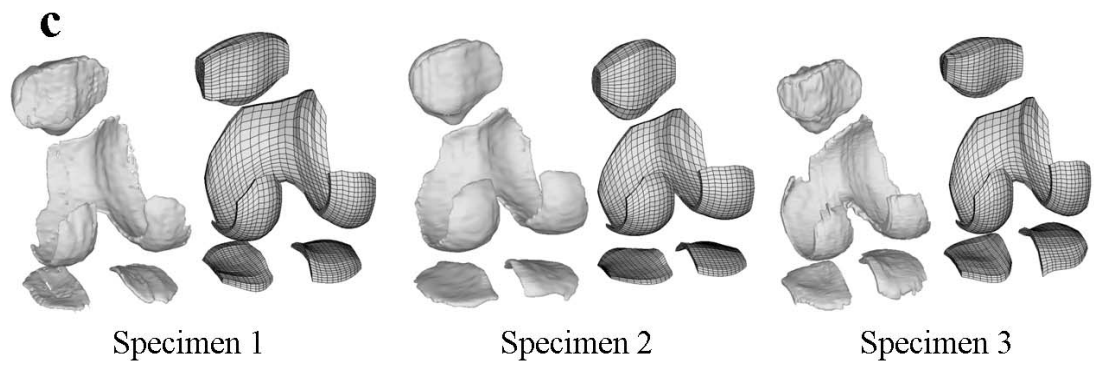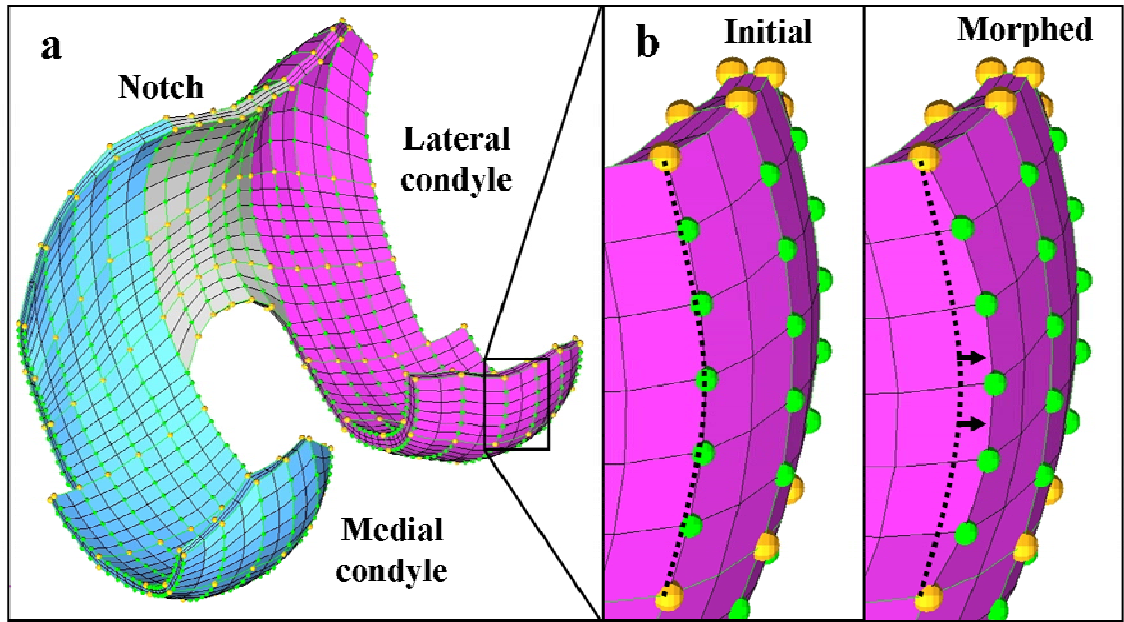
Figure 9.4 (a) Exploded view of template patellar, tibial and femoral hexahedral meshes illustrating control points (yellow), (b) medial, lateral, and notch regions of the femoral cartilage, and (c) three subject-specific segmented surfaces (left) and semi-automated hexahedral solid meshes (right).

MANUAL
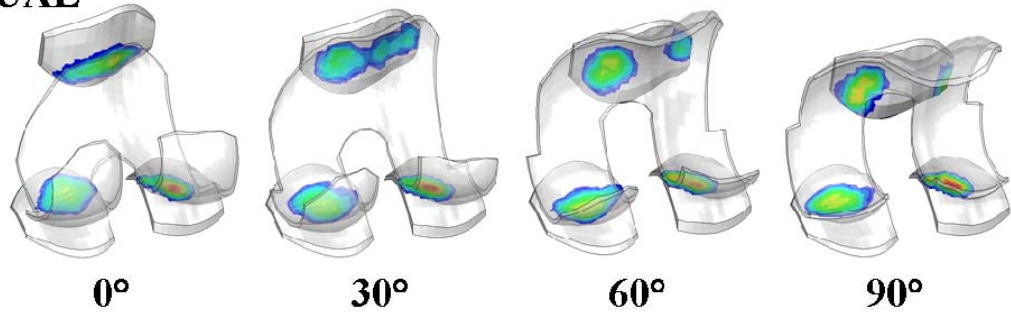
GUI
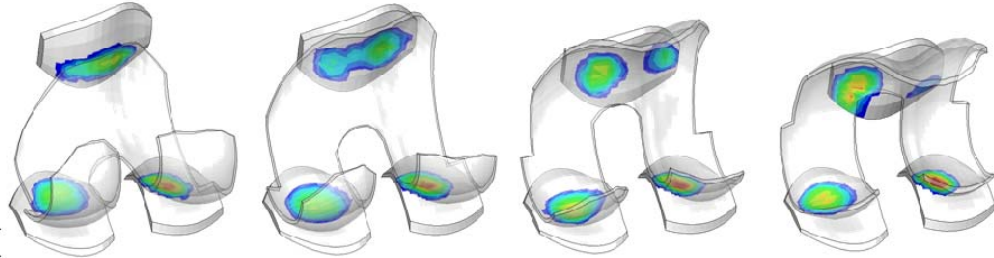
Figure 9.5 Comparison of model-predicted contact pressure contours between 0 and 90°
femoral flexion for a single subject generated with traditional manual segmentation
(top) and integrated extraction, mesh-morphing (bottom) approaches.
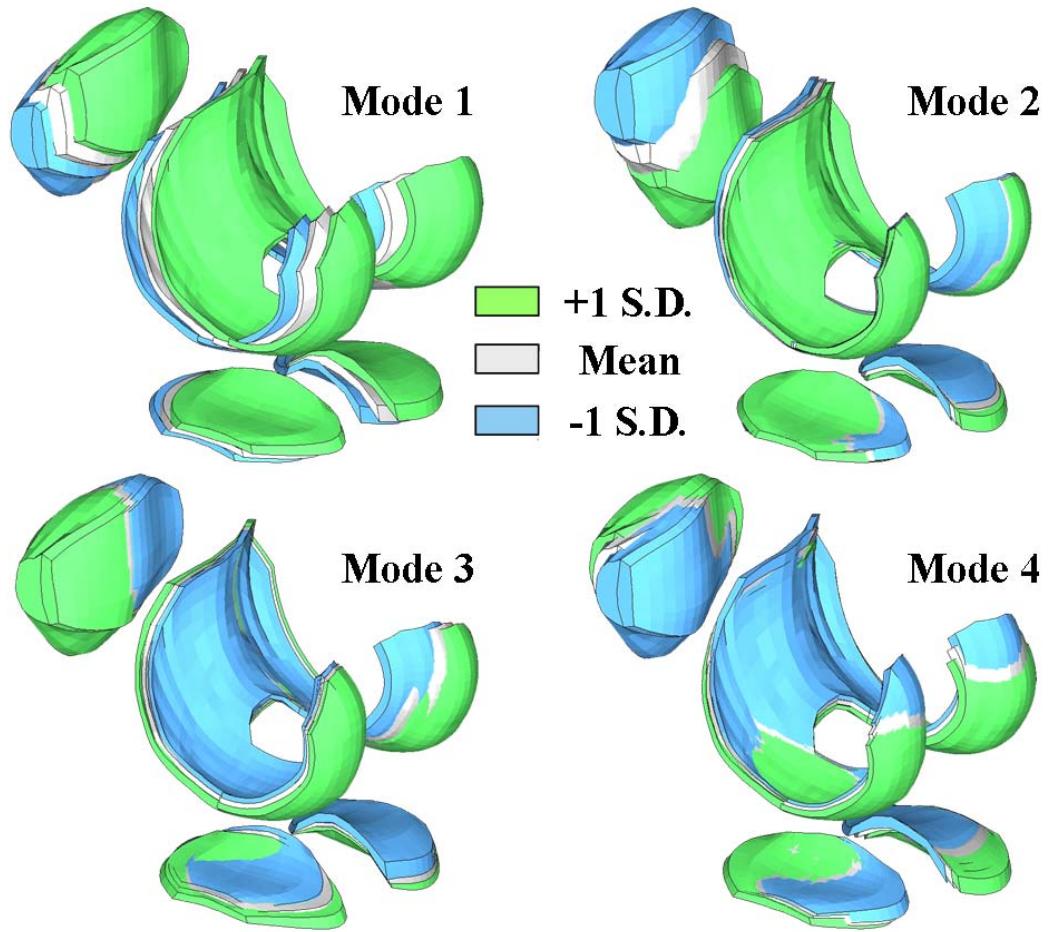
Figure 9.6 Statistical shape model of the knee showing mean and ±1 standard deviation (S.D.) geometries for the first 4 modes of variation.

CHAPTER 10. CONCLUSIONS AND RECOMMENDATIONS

The studies presented in this dissertation represent a progression of work using the explicit FE method to understand the influence of soft tissue constraint on clinically relevant issues involving the natural and implanted knee. Specific emphasis was placed on verifying model predictions against either published literature findings or directly against experimental measurements as a means to ensure model accuracy. Creating custom FE biomechanical models is inherently difficult due to the substantial time and specific knowledge required to create complex anatomic geometries and perform model pre-processing, debugging, and post-processing. However, once constructed, the relative ease in changing loading or boundary conditions, mechanical property definitions, or conducting parametric or probabilistic studies can provide invaluable information that would otherwise be impossible or cost-prohibitive to obtain. In application to implant design, the studies presented in this dissertation represent development of a suite of computational tools that could be used to improve long-term implant performance *in-vivo* and potentially reduce the implant design cycle.

The computationally efficient natural knee ligament model described in Chapter 4 represents a novel application of established probabilistic techniques that successfully identified important aspects of constraint that may have further computational or clinical applicability. For example, results from the probabilistic knee ligament model may be used to improve the efficiency of optimizing ligamentous constraint by

eliminating unimportant ligament structures or parameters from the input set or from specific loading scenarios where recruitment is negligible. Clinically, the probabilistic ligament model could be used to assist in pre-operative planning of soft tissue reconstruction efforts by focusing repair on the most important ligaments or the most influential mechanical or attachment parameters for particular loading condition. The strong agreement between predicted laxity bounds using the efficient AMV and more commonly used Monte Carlo methods demonstrate the advantage of using the AMV approach to generate similar results to the Monte Carlo analysis at a reduced computational cost.

In a similar fashion, the probabilistic implanted patellofemoral model successfully identified the most important aspects of implant component alignment influencing TKA kinematics and contact mechanics and predicted bounds of output measures as an indication of robustness to surgical malalignment. Although this particular study utilized a generic or representative knee and virtual implantation, the important alignment parameters identified were in agreement with previous experimental evaluations performed by other groups, providing additional credibility to the current method in the absence of direct model verification. Methods used in this study could be applied to future patellar component design evaluations as a comparative measure of robustness to surgical malalignment or to understand the effect of particular feature or size changes on predicted patellar mechanics. The probabilistic natural knee ligament model and implanted patellofemoral model are examples of coupling FE and probabilistic methods to expand the predictive capability of a single deterministic model to theoretical populations and to provide more realistic output measures given the large

150

amount of anatomic and mechanical uncertainty in modeling biomechanical events. These methods have broad applicability to other biomechanical research and should continue to be used to offset the assumptions and limitations of individual deterministic models.

Chapters 6 and 7 present work that specifically focused on methods for verifying predicted kinematics directly against experimental measurements in specimen-specific knee models. This required an initial step of developing an efficient, anatomic ligament material model that could be used to represent the various knee ligaments while providing localized fiber recruitment patterns and interactions with surrounding bony or implanted structures. The fiber-reinforced ligament representation described in Chapter 3 was crucial to providing whole joint constraint during simulated dynamic events at a relatively low computational cost while maintaining solution stability.

The isolated patellofemoral model-verification study presented in Chapter 6 demonstrated the fiber-reinforced representation was effective in providing soft tissue constraint for multiple specimens in their natural and implanted states. Root mean square differences between model-predicted and experimental kinematics in the isolated patellofemoral study were similar to those of previous component-only studies, indicating the current implementation of the fiber-reinforced material model was appropriate for representing cadaveric ligamentous constraint with a minimal impact on model accuracy. Yet, this initial application of the fiber-reinforced material model required literature-based stiffness parameters and manual tuning of the initial strains in the patellofemoral ligaments to achieve acceptable kinematic predictions. The next

logical step in moving towards representing whole joint specimen-specific constraint was to develop a method for adjusting ligament parameters via optimization to match experimental laxity responses.

The dual-phase optimization approach described in Chapter 7 presented a novel computational method for reproducing specimen-specific ligamentous constraint crossing the tibiofemoral joint. This work represents a unique method of combining experimental torque-rotation responses in implanted cadaveric specimens to establish a passive laxity envelope as a direct input for optimizing ligament parameters in specimen-specific FE knee models. While an acceptable match was found in model-predicted and experimental laxity envelopes for four separate specimens, the more important application was in the force-driven whole joint models.

Cadaveric testing in the Kansas knee simulator provided a suitable basis for performing computational whole joint evaluations. The deep knee bend and gait loading cycles included in the model-verification study provided a good combination of simulated activities with a large range of motion (deep knee bend) and out-of-plane loading (gait). Similar to the isolated patellofemoral study, there was only a small increase in RMS differences compared to previous component-only whole joint investigations. When comparing the same knee models with literature-based and optimized ligament values, it was apparent that the optimization process was an important factor in reproducing experimental kinematics and predicting realistic ligament recruitment.

The study of crepitation related to PS implant alignment and anatomic variability described in Chapter 8 demonstrated a crucial step towards applying computational biomechanics to clinically relevant problems. Orthopedic surgeons are well versed in their particular surgical techniques, but there are many complications associated with TKA that they struggle to understand and go largely unaddressed. This situation provides a unique opportunity for the computational biomechanist to provide new or unique information which could potentially affect future component designs to mitigate or eliminate the problem. Collaboration with clinicians is pivotal in applying computational methods directly to clinical problems and should be a continued direction of future research.

The techniques of developing subject-specific natural knee models described in Chapter 9 were included in this dissertation as an indication of future research. Previous studies primarily focused on the implanted knee, which is beneficial in eliminating the complexity of modeling cruciate and meniscal structures removed during TKA surgery. However, to properly assess long-term clinical success of an implant design, it would be beneficial to understand the unaltered state of the joint compared to the post-TKA joint. Specifically, modeling constraint in the natural knee could assist in improving component placement on a patient-by-patient basis or be used to assess the effect of implant design on reproducing ligament balance and range of motion in the unaltered joint. The methods presented in the current study address the most time-consuming aspect of natural knee modeling by improving the efficiency of generating articular cartilage meshes from medical images. In future efforts, statistical shape modeling could be expanded to include efficient generation of soft tissue

structures to quickly generate an entire ligament knee model based on a limited set of input parameters.

In summary, the techniques described in this dissertation represent advancements in creating and analyzing more realistic, anatomic whole joint ligamentous knee models. Future endeavors should attempt to apply these techniques to the more challenging natural joint state and implement the fiber-reinforced material model into forward- or muscle-driven lower limb natural or implanted models to perform computational investigations under more physiological loading conditions.

LIST OF REFERENCES

ABAQUS, 2006. ABAQUS Analysis User's Manual. Simulia, Providence, RI. (Version 6.6-1):

Abdel-Rahman, E.M., Hefzy, M.S., 1998. Three-dimensional dynamic behaviour of the human knee joint under impact loading. Medical Engineering & Physics. 20 (4):276-290.

Amis, A.A., Bull, A.M., Gupte, C.M., Hijazi, I., Race, A., Robinson, J.R., 2003a. Biomechanics of the PCL and related structures: posterolateral, posteromedial and meniscofemoral ligaments. Knee Surgery and Sports Traumatology Arthroscopy. 11 (5):271-281.

Amis, A.A., Firer, P., Mountney, J., Senavongse, W., Thomas, N.P., 2003b. Anatomy and biomechanics of the medial patellofemoral ligament. Knee. 10 (3):215-220.

Amis, A.A., Senavongse, W., Bull, A.M., 2006. Patellofemoral kinematics during knee flexion-extension: An in vitro study. Journal of Orthopedic Research. 24 (12):2201-2211.

Anderson, J.A., Baldini, A., Sculco, T.P., 2008. Patellofemoral function after total knee arthroplasty: a comparison of 2 posterior-stabilized designs. Journal of Knee Surgery. 21 (2):91-96.

Andrikoula, S., Tokis, A., Vasiliadis, H.S., Georgoulis, A., 2006. The extensor mechanism of the knee joint: an anatomical study. Knee Surgery Sports Traumatology Arthroscopy. 14 (3):214-220.

Anglin, C., Brimacombe, J.M., Hodgson, A.J., Masri, B.A., Greidanus, N.V., Tonetti, J., Wilson, D.R., 2008. Determinants of patellar tracking in total knee arthroplasty. Clinical Biomechanics. 23 (7):900-910.

Arms, S., Boyle, J., Johnson, R., Pope, M., 1983. Strain Measurement in the Medial Collateral Ligament of the Human Knee: An Autopsy Study. Journal of Biomechanics. 16 (7):491-496.

Armstrong, A.D., Brien, H.J., Dunning, C.E., King, G.J., Johnson, J.A., Chess, D.G., 2003. Patellar position after total knee arthroplasty: influence of femoral component malposition. Journal of Arthroplasty. 18 (4):458-465.

Atkinson, P., Atkinson, T., Huang, C., Doane, R., 2000. A Comparison of the Mechanical and Dimensional Properties of the Human Medial and Lateral Patellofemoral Ligaments. 46th Annual Meeting of the Orthopaedic Research Society. 0776.

155

Bach, J.M., Hull, M.L., Patterson, H.A., 1997. Direct measurement of strain in the posterolateral bundle of the anterior cruciate ligament. Journal of Biomechanics. 30 (3):281-283.

Baldini, A., Anderson, J.A., Zampetti, P., Pavlov, H., Sculco, T.P., 2006. A new patellofemoral scoring system for total knee arthroplasty. Clinical Orthopedics and Related Research. 452 150-154.

Baldwin, M.A., Clary, C.W., Maletsky, L.P., Laz, P.J., Rullkoetter, P.J., 2009a. Predicting Whole Joint Mechanics during Simulated Dynamic Loading Using Specimen-specific Ligamentous Constraint. (in review).

Baldwin, M.A., Clary, C.W., Maletsky, L.P., Rullkoetter, P., 2009b. Verification of Predicted Specimen-Specific Natural and Implanted Patellofemoral Kinematics during Simulated Deep Knee Bend. (in review).

Baldwin, M.A., Laz, P.J., Stowe, J.Q., Rullkoetter, P.J., 2009c. Efficient Probabilistic Representation of Tibiofemoral Soft Tissue Constraint. Computer Methods in Biomechanics and Biomedical Engineering. (in review)

Baldwin, M.A., Rullkoetter, P., 2007. Computationally Efficient, Explicit Finite Element Model for Evaluation of Patellofemoral Mechanics. ASME SBC 2007 Summer Bioengineering Conference. (176480):

Barink, M., van Kampen, A., de Waal Malefijt, M., Verdonschot, N., 2005. A three-dimensional dynamic finite element model of the prosthetic knee joint: Simulation of joint laxity and kinematics. Proceedings of the Institution of Mechanical Engineers, Part H: Journal of Engineering in Medicine. 219 (6):415-424.

Barratt, D.C., Chan, C.S., Edwards, P.J., Penney, G.P., Slomczykowski, M., Carter, T.J., Hawkes, D.J., 2008. Instantiation and registration of statistical shape models of the femur and pelvis using 3D ultrasound imaging. Medical Image Analysis. 12 (3):358-374.

Beight, J.L., Yao, B., Hozack, W.J., Hearn, S.L., Booth, R.E., Jr., 1994. The patellar "clunk" syndrome after posterior stabilized total knee arthroplasty. Clinical Orthopedics and Related Research. (299):139-142.

Beillas, P., Lee, S.W., Tashman, S., Yang, K.H., 2007. Sensitivity of the tibio-femoral response to finite element modeling parameters. Computer Methods in Biomechanics and Biomedical Engineering. 10 (3):209-221.

Beillas, P., Papaioannou, G., Tashman, S., Yang, K.H., 2004. A new method to investigate in vivo knee behavior using a finite element model of the lower limb. Journal of Biomechanics. 37 (7):1019-1030.

Bendjaballah, M.Z., Shirazi-Adl, A.: Menisci and stability of human knee in extension: A finite element model study. pp 313-314. San Francisco, CA, USA, ASME, New York, NY, USA, 1995

Bendjaballah, M.Z., Shirazi-Adl, A., Zukor, D.J., 1997a. Finite element analysis of human knee joint in varus-valgus. Clinical Biomechanics. 12 (3):139-148.

Bendjaballah, M.Z., Shirazi-Adl, A., Zukor, D.J.: Passive knee joint mechanics in A-P forces - role of boundary conditions, cruciates, and menisci. pp 143-144. Dallas, TX, USA, ASME, Fairfield, NJ, USA, 1997b

Besier, T.F., Draper, C.E., Gold, G.E., Beaupre, G.S., Delp, S.L., 2005a. Patellofemoral joint contact area increases with knee flexion and weight-bearing. Journal of Orthopaedic Research. 23 (2):345-350.

Besier, T.F., Gold, G.E., Beaupre, G.S., Delp, S.L., 2005b. A modeling framework to estimate patellofemoral joint cartilage stress in vivo. Medical Science in Sports Exercise. 37 (11):1924-1930.

Besier, T.F., Gold, G.E., Delp, S.L., Fredericson, M., Beaupre, G.S., 2008. The influence of femoral internal and external rotation on cartilage stresses within the patellofemoral joint. Journal of Orthopedic Research. 26 (12):1627-1635.

Blankevoort, L., Huiskes, R., 1996. Validation of a three-dimensional model of the knee. Journal of Biomechanics. 29 (7):955-961.

Blankevoort, L., Huiskes, R., De Lange, A., 1988. The Envelope of passive knee joint motion. Journal of Biomechanics. 21 (9):705-720.

Blankevoort, L., Huiskes, R., de Lange, A., 1991a. Recruitment of knee joint ligaments. Journal of Biomechanical Engineering, Transactions of the ASME. 113 (1):94-103.

Blankevoort, L., Kuiper, J.H., Huiskes, R., Grootenboer, H.J., 1991b. Articular contact in a three-dimensional model of the knee. Journal of Biomechanics. 24 (11):1019-1031.

Blemker, S.S., Delp, S.L., 2005. Three-dimensional representation of complex muscle architectures and geometries. Annals of Biomedical Engineering. 33 (5):661-673.

Bradley, J., FitzPatrick, D., Daniel, D., Shercliff, T., O'Connor, J., 1988. Orientation of the cruciate ligament in the sagittal plane. A method of predicting its length-change with flexion. Journal of Bone and Joint Surgery Britain. 70 (1):94-99.

Bredbenner, T.L., Nicolella, D.P., 2008. Statistical Shape and Density Based Finite Element Modeling of the Human Proximal Femur. Transactions of the 54th Annual Meeting of the Orthopaedic Research Society. 33 0305.

Brick, G.W., Scott, R.D., 1988. The patellofemoral component of total knee arthroplasty. Clinical orthopaedics and related research. 231 163-178.

Bryan, R., Mohan, S., Hopkins, A., Nair, P., Taylor, M., 2008. Generation of a Statistical Model of the Whole Femur Incorporating Shape and Material Property Distribution. Transactions of the 54th Annual Meeting of the Orthopaedic Research Society. 33 0912.

Butler, D.L., Kay, M.D., Stouffer, D.C., 1986. Comparison of Material Properties in Fascicle-Bone Units from Human Patellar Tendon and Knee Ligaments. Journal of Biomechanics. 19 (6):425-432.

Butler, D.L., Noyes, F.R., Grood, E.S., 1980. Ligamentous restraints to anterior-posterior drawer in the human knee. A biomechanical study. Jounral of Bone and Joint Surgery America. 62 (2):259-270.

Bylski-Austrow, D.I., Grood, E.S., Hefzy, M.S., Holden, J.P., Butler, D.L., 1990. Anterior cruciate ligament replacements. A mechanical study of femoral attachment location, flexion angle at tensioning, and initial tension. Journal of Orthopaedic Research. 8 (4):522-531.

Caruntu, D.I., Hefzy, M.S., 2004. 3-D anatomically based dynamic modeling of the human knee to include tibio-femoral and patello-femoral joints. Journal of Biomechanical Engineering. 126 (1):44-53.

Chandrashekar, N., Mansouri, H., Slauterbeck, J., Hashemi, J., 2006. Sex-based differences in the tensile properties of the human anterior cruciate ligament. Journal of Biomechanics. 39 (16):2943-2950.

Chu, X.B., Wu, H.S., Xu, C.M., Zhu, Y.L., Feng, M.G., He, Z.Y., 2006. The effect of rotational alignment of the femoral components on the patellofemoral biomechanics in total knee arthroplasty. Zhonghua Wai Ke Za Zhi. 44 (16):1136-1140.

Cohen, Z.A., Henry, J.H., McCarthy, D.M., Mow, V.C., Ateshian, G.A., 2003. Computer simulations of patellofemoral joint surgery. Patient-specific models for tuberosity transfer. American Journal of Sports Medicine. 31 (1):87-98.

Cohen, Z.A., McCarthy, D.M., Kwak, S.D., Legrand, P., Fogarasi, F., Ciaccio, E.J., Ateshian, G.A., 1999. Knee cartilage topography, thickness, and contact areas from MRI: in-vitro calibration and in-vivo measurements. Osteoarthritis and Cartilage. 7 (1):95-109.

Cohen, Z.A., Roglic, H., Grelsamer, R.P., Henry, J.H., Levine, W.N., Mow, V.C., Ateshian, G.A., 2001. Patellofemoral stresses during open and closed kinetic chain exercises. An analysis using computer simulation. American Journal of Sports Medicine. 29 (4):480-487.

Connolly, A., FitzPatrick, D., Moulton, J., Lee, J., Lerner, A., 2008. Tibiofemoral cartilage thickness distribution and its correlation with anthropometric variables. Proceedings of the IMechE - Part H: Journal of Engineering in Medicine. 222 (1):29-39.

Corana, A., Marchesi, C., 1987. Minimizing Multimodal Functions of Continuous Variables with the "Simualted Annealing" Algorithm. Transactions on Mathematical Software. 13 (3):262-280.

Couteau, B., Payan, Y., Lavallee, S., 2000. The mesh-matching algorithm: An automatic 3D mesh generator for finite element structures. Journal of Biomechanics. 33 (8):1005-1009.

D'Lima, D.D., Chen, P.C., Kester, M.A., Colwell, C.W., Jr., 2003. Impact of patellofemoral design on patellofemoral forces and polyethylene stresses. The American Journal of Bone Joint Surgery. 85-A Suppl 4 85-93.

Deheer, D.C., Hillberry, B.M., 1992. The effect of thickness and nonlinear material behavior on contact stresses in polyethylene tibial components. 38th Annual Meeting of the Orthopaedic Research Society.

Della Croce, U., Cappozzo, A., Kerrigan, D.C., 1999. Pelvis and lower limb anatomical landmark calibration precision and its propagation to bone geometry and joint angles. Medical & Biological Engineering & Computing. 37 (2):155-161.

Dhaher, Y.Y., Kahn, L.E., 2002. The effect of vastus medialis forces on patello-femoral contact: a model-based study. Journal of Biomechanical Engineering. 124 (6):758-767.

Easley, S.K., Pal, S., Tomaszewski, P.R., Petrella, A.J., Rullkoetter, P.J., Laz, P.J., 2007. Finite element-based probabilistic analysis tool for orthopaedic applications. Computer Methods and Programs in Biomedicine. 85 (1):32-40.

Elias, J.J., Bratton, D.R., Weinstein, D.M., Cosgarea, A.J., 2006. Comparing two estimations of the quadriceps force distribution for use during patellofemoral simulation. Journal of Biomechanics. 39 (5):865-872.

Elias, J.J., Cosgarea, A.J., 2006. Technical errors during medial patellofemoral ligament reconstruction could overload medial patellofemoral cartilage: a computational analysis. American Journal of Sports Medicine. 34 (9):1478-1485.

159

Elias, J.J., Mattessich, S.M., Kumagai, M., Mizuno, Y., Cosgarea, A.J., Chao, E.Y., 2004a. In vitro characterization of the relationship between the Q-angle and the lateral component of the quadriceps force. Proc Inst Mech Eng [H]. 218 (1):63-67.

Elias, J.J., Wilson, D.R., Adamson, R., Cosgarea, A.J., 2004b. Evaluation of a computational model used to predict the patellofemoral contact pressure distribution. Journal of Biomechanics. 37 (3):295-302.

Evans, P., 1979. The postural function of the iliotibial tract. Annals of the Royal College of Surgery, England. 61 (4):271-280.

Farahmand, F., Senavongse, W., Amis, A.A., 1998. Quantitative study of the quadriceps muscles and trochlear groove geometry related to instability of the patellofemoral joint. Journal of Orthopaedic Research. 16 (1):136-143.

Fernandez, J.W., Hunter, P.J., 2005. An anatomically based patient-specific finite element model of patella articulation: towards a diagnostic tool. Biomechanics in Modeling and Mechanobiology. 4 (1):20-38.

Fernandez, J.W., Mithraratne, P., Thrupp, S.F., Tawhai, M.H., Hunter, P.J., 2004. Anatomically based geometric modelling of the musculo-skeletal system and other organs. Biomechanical Modeleling in Mechanobiology. 2 (3):139-155.

Fukubayashi, T., Torzilli, P.A., Sherman, M.F., Warren, R.F., 1982. An in vitro biomechanical evaluation of anterior-posterior motion of the knee. Tibial displacement, rotation, and torque. Journal of Bone and Joint Surgery America. 64 (2):258-264.

Gardiner, J.C., Weiss, J.A., 2003. Subject-specific finite element analysis of the human medial collateral ligament during valgus knee loading. Journal of Orthopaedic Research. 21 (6):1098-1106.

Gardiner, J.C., Weiss, J.A., Rosenberg, T.D., 2001. Strain in the human medial collateral ligament during valgus loading of the knee. Clinical Orthopedics and Related Research. (391):266-274.

Girgis, F.G., Marshall, J.L., Monajem, A., 1975. The cruciate ligaments of the knee joint. Anatomical, functional and experimental analysis. Clinical Orthopedics and Related Research. 106 216-230.

Godest, A.C., Beaugonin, M., Haug, E., Taylor, M., Gregson, P.J., 2002. Simulation of a knee joint replacement during a gait cycle using explicit finite element analysis. Journal of Biomechanics. 35 (2):267-275.

Goffe, W.L., Ferrier, G.D., Rogers, J., 1994. Global Optimization of Statistical Functions with Simulated Annealing. Journal of Econometrics. 60 (1-2):65-99.

Gollehon, D.L., Torzilli, P.A., Warren, R.F., 1987. The role of the posterolateral and cruciate ligaments in the stability of the human knee. A biomechanical study. Journal of Bone and Joint Surgery America. 69 (2):233-242.

Griffith, C.J., Wijdicks, C.A., LaPrade, R.F., Armitage, B.M., Johansen, S., Engebretsen, L., 2009. Force measurements on the posterior oblique ligament and superficial medial collateral ligament proximal and distal divisions to applied loads. American Journal of Sports Medicine. 37 (1):140-148.

Grood, E.S., Hefzy, M.S., Lindenfield, T.N., 1989. Factors affecting the region of most isometric femoral attachments. Part I: The posterior cruciate ligament. The American Journal of Sports Medicine. 17 (2):197-207.

Grood, E.S., Stowers, S.F., Noyes, F.R., 1988. Limits of movement in the human knee. Effect of sectioning the posterior cruciate ligament and posterolateral structures. Journal of Bone and Joint Surgery America. 70 (1):88-97.

Grood, E.S., Suntay, W.J., 1983. Joint Coordinate System for the Clinical Description of Three-Dimensional Motions: Application to the Knee. Journal of Biomechanical Engineering, Transactions of the ASME. 105 (2):136-144.

Grosland, N.M., Bafna, R., Magnotta, V.A., 2008. Automated hexahedral meshing of anatomic structures using deformable registration. Computer Methods in Biomechanics and Biomedical Engineering. 12 (1):35-43.

Guess, T.M., Maletsky, L.P., 2005. Computational modelling of a total knee prosthetic loaded in a dynamic knee simulator. Medical Engineering and Physics. 27 (5):357-367.

Haldar, A., Mahadevan, S., 2000. Probability, Reliability and Statistical Methods in Engineering Design.

Halloran, J., Maletsky, L.P., Taylor, M., Clary, C., Petrella, A., Rullkoetter, P., 2005a. Dynamic Finite Element Model Predicts Tibio- and Patello-femoral Mechanics. 51st Annual Meeting of the Orthopaedic Research Society. 0116.

Halloran, J., Maletsky, L.P., Taylor, M., Clary, C., Petrella, A., Rullkoetter, P., 2006. Validation of Predicted TKR Kinematic Variation with Implant Design. 52nd Annual Meeting of the Orthopaedic Research Society. 31 0588.

Halloran, J.P., Clary, C.W., Maletsky, L.P., Taylor, M., Petrella, A., Rullkoetter, P., 2009. Verification of Predicted Knee Replacement Kinematics during Simulated Gait in the Kansas Knee Simulator. Biomechanical Engineering (in review).

Halloran, J.P., Easley, S.K., Petrella, A.J., Rullkoetter, P.J., 2005b. Comparison of deformable and elastic foundation finite element simulations for predicting knee

replacement mechanics. Journal of Biomechanical Engineering. 127 (5):813-818.

Halloran, J.P., Petrella, A.J., Rullkoetter, P.J., 2005c. Explicit finite element modeling of total knee replacement mechanics. Journal of Biomechanics. 38 (2):323-331.

Harner, C.D., Baek, G.H., Vogrin, T.M., Carlin, G.J., Kashiwaguchi, S., Woo, S.L., 1999. Quantitative analysis of human cruciate ligament insertions. Arthroscopy. 15 (7):741-749.

Harner, C.D., Xerogeanes, J.W., Livesay, G.A., Carlin, G.J., Smith, B.A., Kusayama, T., Kashiwaguchi, S., Woo, S.L., 1995. The human posterior cruciate ligament complex: an interdisciplinary study. Ligament morphology and biomechanical evaluation. The American Journal of Sports Medicine. 23 (6):736-745.

Healy, W.L., Wasilewski, S.A., Takei, R., Oberlander, M., 1995. Patellofemoral complications following total knee arthroplasty. Correlation with implant design and patient risk factors. Journal of Arthroplasty. 10 (2):197-201.

Heegaard, J., Leyvraz, P.F., Curnier, A., Rakotomanana, L., Huiskes, R., 1995. The biomechanics of the human patella during passive knee flexion. Journal of Biomechanics. 28 (11):1265-1279.

Heegaard, J., Leyvraz, P.F., Van Kampen, A., Rakotomanana, L., Rubin, P.J., Blankevoort, L., 1994. Influence of soft structures on patellar three-dimensional tracking. Clinical orthopaedics and related research. 299 (Feb):235-243.

Heegaard, J.H., Leyvraz, P.F., Hovey, C.B., 2001. A computer model to simulate patellar biomechanics following total knee replacement: the effects of femoral component alignment. Clinical Biomechanics. 16 (5):415-423.

Hefzy, M.S., Abdel-Rahman, E.M.: Three-dimensional dynamic modeling of the human knee joint: formulation and solution technique. pp 909-916. Atlanta, GA, USA, ASME, New York, NY, USA, 1996

Hefzy, M.S., Grood, E.S., Noyes, F.R., 1989. Factors affecting the region of most isometric femoral attachments. Part II: The anterior cruciate ligament. The American Journal of Sports Medicine. 17 (2):208-216.

Hozack, W.J., Rothman, R.H., Booth, R.E., Jr., Balderston, R.A., 1989. The patellar clunk syndrome. A complication of posterior stabilized total knee arthroplasty. Clinical Orthopedics and Related Research. (241):203-208.

Hsu, H.C., Luo, Z.P., Rand, J.A., An, K.N., 1996. Influence of patellar thickness on patellar tracking and patellofemoral contact characteristics after total knee arthroplasty. Journal of Arthroplasty. 11 (1):69-80.

Hughston, J.C., Eilers, A.F., 1973. The Role of the Posterior Oblique Ligament in Repairs of Acute Medial (Collateral) Ligament Tears of the Knee. Journal of Bone Joint Surgery America. 55 (5):923-940.

Hull, M.L., Berns, G.S., Varma, H., Patterson, H.A., 1996. Strain in the medial collateral ligament of the human knee under single and combined loads. Journal of Biomechanics. 29 (2):199-206.

Jolliffe, I.T., 2002. Principal Component Analysis. Springer, New York, NY. (502):

Kallemyn, N.A., Shivanna, K.H., Grosland, N.M., 2007. A novel method for patient specific finite element mesh development of the spine. 31st Annual Meeting of the American Society of Biomechanics. Palo Alto, CA

Kessler, O., Patil, S., Colwell, C.W., Jr., D'Lima, D.D., 2008. The effect of femoral component malrotation on patellar biomechanics. Journal of Biomechanics. 41 (16):3332-3339.

Keyak, J.H., Meagher, J.M., Skinner, H.B., Mote, J.C.D., 1990. Automated three-dimensional finite element modelling of bone: a new method. Journal of Biomedical Engineering. 12 (5):389-397.

Komistek, R.D., Dennis, D.A., Mabe, J.A., Walker, S.A., 2000. In vivo determination of patellofemoral contact positions. Clinical Biomechanics. 15 (1):29-36.

LaPrade, R.F., Engebretsen, A.H., Ly, T.V., Johansen, S., Wentorf, F.A., Engebretsen, L., 2007a. The anatomy of the medial part of the knee. Journal of Bone and Joint Surgery America. 89 (9):2000-2010.

LaPrade, R.F., Ly, T.V., Wentorf, F.A., Engebretsen, L., 2003. The posterolateral attachments of the knee: a qualitative and quantitative morphologic analysis of the fibular collateral ligament, popliteus tendon, popliteofibular ligament, and lateral gastrocnemius tendon. American Journal of Sports Medicine. 31 (6):854-860.

LaPrade, R.F., Morgan, P.M., Wentorf, F.A., Johansen, S., Engebretsen, L., 2007b. The anatomy of the posterior aspect of the knee. An anatomic study. Journal of Bone and Joint Surgery America. 89 (4):758-764.

Laz, P.J., Pal, S., Halloran, J.P.,Patrella, A.J., Rullkoetter, P.J., 2005. Probabilistic Finite Element Predictions of Knee Wear Simulator Mechanics. Journal of Biomechanics. 1-8.

Laz, P.J., Stowe, J.Q., Baldwin, M.A., Petrella, A.J., Rullkoetter, P., 2007. Incorporating uncertainty in mechanical properties for finite element-based evaluation of bone mechanics. Journal of Biomechanics. 40 (13):2831-2836.

163

Lee, T.Q., Budoff, J.E., Glaser, F.E., 1999. Patellar component positioning in total knee arthroplasty. Clinical Orthopedics and Related Research. (366):274-281.

Li, G., Gil, J., Kanamori, A., Woo, S.L.Y., 1999. Validated three-dimensional computational model of a human knee joint. Journal of Biomechanical Engineering, Transactions of the ASME. 121 (6):657-662.

Li, G., Suggs, J., Gill, T., 2002. The effect of anterior cruciate ligament injury on knee joint function under a simulated muscle load: A three-dimensional computational simulation. Annals of Biomedical Engineering. 30 (5):713-720.

Limbert, G., Middleton, J., 2006. A constitutive model of the posterior cruciate ligament. Medical Engineering and Physics. 28 (2):99-113.

Limbert, G., Taylor, M., 2002. On the constitutive modeling of biological soft connective tissues. A general theoretical framework and explicit forms of the tensors of elasticity for strongly anisotropic continuum fiber-reinforced composites at finite strain. International Journal of Solids and Structures. 39 (8):2343-2358.

Luo, Z.P., Sakai, N., Rand, J.A., An, K.N., 1997. Tensile stress of the lateral patellofemoral ligament during knee motion. American Journal of Knee Surgery. 10 (3):139-144.

Maletsky, L.P., Hillberry, B.M., 2005. Simulating dynamic activities using a five-axis knee simulator. Journal of Biomechanical Engineering. 127 (1):123-133.

Maloney, W.J., Schmidt, R., Sculco, T.P., 2003. Femoral component design and patellar clunk syndrome. Clinical Orthopedics and Related Research. (410):199-202.

Markolf, K.L., Kochan, A., Amstutz, H.C., 1984. Measurement of knee stiffness and laxity in patients with documented absence of the anterior cruciate ligament. Journal of Bone and Joint Surgery America. 66 (2):242-252.

Markolf, K.L., Mensch, J.S., Amstutz, H.C., 1976. Stiffness and laxity of the knee--the contributions of the supporting structures. A quantitative in vitro study. Journal of Bone and Joint Surgery America. 58 (5):583-594.

Maynard, M.J., Deng, X., Wickiewicz, T.L., Warren, R.F., 1996. The popliteofibular ligament. Rediscovery of a key element in posterolateral stability. The American Journal of Sports Medicine. 24 (3):311-316.

McGibbon, C.A., 2003. Inter-rater and intra-rater reliability of subchondral bone and cartilage thickness measurement from MRI. Magnetic Resonance Imaging. 21 (7):707-714.

Meding, J.B., Fish, M.D., Berend, M.E., Ritter, M.A., Keating, E.M., 2008. Predicting Patellar Failure After Total Knee Arthroplasty. Clinical orthopaedics and related research. 466 (11):2769-2774.

Meister, B.R., Michael, S.P., Moyer, R.A., Kelly, J.D., Schneck, C.D., 2000. Anatomy and kinematics of the lateral collateral ligament of the knee. American Journal of Sports Medicine. 28 (6):869-878.

Mesfar, W., Shirazi-Adl, A., 2006a. Biomechanics of changes in ACL and PCL material properties or prestrains in flexion under muscle force-implications in ligament reconstruction. Computer Methods in Biomechanics and Biomedical Engineering. 9 (4):201-209.

Mesfar, W., Shirazi-Adl, A., 2005. Biomechanics of the knee joint in flexion under various quadriceps forces. Knee. 12 (6):424-434.

Mesfar, W., Shirazi-Adl, A., 2008. Computational biomechanics of knee joint in open kinetic chain extension exercises. Computer Methods Biomechanics and Biomedical Engineering. 11 (1):55-61.

Mesfar, W., Shirazi-Adl, A., 2006b. Knee joint mechanics under quadriceps--hamstrings muscle forces are influenced by tibial restraint. Clinical Biomechanics. 21 (8):841-848.

Miller, M.C., Zhang, A.X., Petrella, A.J., Berger, R.A., Rubash, H.E., 2001. The effect of component placement on knee kinetics after arthroplasty with an unconstrained prosthesis. Journal of Orthopedic Research. 19 (4):614-620.

Mizuno, Y., Kumagai, M., Mattessich, S.M., Elias, J.J., Ramrattan, N., Cosgarea, A.J., Chao, E.Y., 2001. Q-angle influences tibiofemoral and patellofemoral kinematics. Journal of Orthop Research. 19 (5):834-840.

Moglo, K., Shirazi-Adl, A.: Role of cruciate ligaments in the knee joint in flexion under drawer loads. pp 120-125. Salzburg, Austria, Int. Assoc. of Science and Technology for Development, 2003a

Moglo, K.E., Shirazi-Adl, A., 2003b. Biomechanics of passive knee joint in drawer: load transmission in intact and ACL-deficient joints. Knee. 10 (3):265-276.

Mommersteeg, T.J.A., Blankevoort, L., Huiskes, R., Kooloos, J.G.M., Kauer, J.M.G., 1996a. Characterization of the mechanical behavior of human knee ligaments: a numerical-experimental approach. Journal of Biomechanics. 29 (2):151-160.

Mommersteeg, T.J.A., Huiskes, R., Blankevoort, L., Kooloos, J.G.M., Kauer, J.M.G., 1997. An inverse dynamics modeling approach to determine the restraining function of human knee ligament bundles. Journal of Biomechanics. 30 (2):139-146.

Mommersteeg, T.J.A., Huiskes, R., Blankevoort, L., Kooloos, J.G.M., Kauer, J.M.G., Maathuis, P.G.M., 1996b. Global verification study of a quasi-static knee model with multi-bundle ligaments. Journal of Biomechanics. 29 (12):1659-1664.

Morton, N.A., Maletsky, L.P., Pal, S., Laz, P.J., 2007. Effect of variability in anatomical landmark location on knee kinematic description. Journal of Orthopedic Research. 25 (9):1221-1230.

Muccini, R., Baleani, M., Viceconti, M., 2000. Selection of the best element type in the finite element analysis of hip prostheses. Journal of Medicine & Engineering Technology. 24 (4):145-148.

Munshi, M., Pretterklieber, M.L., Kwak, S., Antonio, G.E., Trudell, D.J., Resnick, D., 2003. MR imaging, MR arthrography, and specimen correlation of the posterolateral corner of the knee: an anatomic study. American Journal of Roentgenology. 180 (4):1095-1101.

Neptune, R.R., Wright, I.C., van den Bogert, A.J., 2000. The influence of orthotic devices and vastus medialis strength and timing on patellofemoral loads during running. Clinical Biomechanics. 15 (8):611-618.

Netter, F.H., 2006. Atlas of Human Anatomy, 4th Edition.

Nomura, E., Horiuchi, Y., Kihara, M., 2000. Medial patellofemoral ligament restraint in lateral patellar translation and reconstruction. Knee. 7 (2):121-127.

Nomura, E., Inoue, M., Osada, N., 2005. Anatomical analysis of the medial patellofemoral ligament of the knee, especially the femoral attachment. Knee Surgery Sports Traumatology Arthroscopy. 13 (7):510-515.

Pagnano, M.W., Trousdale, R.T., 2000. Asymmetric patella resurfacing in total knee arthroplasty. American Journal of Knee Surgery. 13 (4):228-233.

Pal, S., Haider, H., Laz, P.J., Knight, L.A., Rullkoetter, P.J., 2008. Probabilistic computational modeling of total knee replacement wear. Wear. 264 (7-8):701-707.

Pal, S., Langenderfer, J.E., Stowe, J.Q., Laz, P.J., Petrella, A.J., Rullkoetter, P.J., 2007. Probabilistic modeling of knee muscle moment arms: effects of methods, origin-insertion, and kinematic variability. Annals of Biomedical Engineering. 35 (9):1632-1642.

Park, S.E., DeFrate, L.E., Suggs, J.F., Gill, T.J., Rubash, H.E., Li, G., 2005. The change in length of the medial and lateral collateral ligaments during in vivo knee flexion. Knee. 12 (5):377-382.

Park, S.E., Stamos, B.D., DeFrate, L.E., Gill, T.J., Li, G., 2004. The effect of posterior knee capsulotomy on posterior tibial translation during posterior cruciate ligament tibial inlay reconstruction. American Journal of Sports Medicine. 32 (6):1514-1519.

Pena, E., 2005. A Three-Dimensional Finite Element Analysis of the Combined Behavior of Ligaments and Menisci in the Healthy Human Knee Joint. Journal of Biomechanics. 1-16.

Pena, E., Calvo, B., Martinez, M.A., Doblare, M., 2006. A three-dimensional finite element analysis of the combined behavior of ligaments and menisci in the healthy human knee joint. Journal of Biomechanics. 39 (9):1686-1701.

Pena, E., Martinez, M.A., Calvo, B., Palanca, D., Doblare, M., 2005. A finite element simulation of the effect of graft stiffness and graft tensioning in ACL reconstruction. Clinical Biomechanics. 20 (6):636-644.

Petersen, W., Loerch, S., Schanz, S., Raschke, M., Zantop, T., 2008. The role of the posterior oblique ligament in controlling posterior tibial translation in the posterior cruciate ligament-deficient knee. American Journal of Sports Medicine. 36 (3):495-501.

Piziali, R.L., Seering, W.P., Nagel, D.A., Schurman, D.L., 1980. Function of the Primary Ligaments of the Knee in Anteior-Posterior and Medial-Lateral Motions. Journal of Biomechanics. 13 (9):777-784.

Pollock, D.C., Ammeen, D.J., Engh, G.A., 2002. Synovial entrapment: a complication of posterior stabilized total knee arthroplasty. Journal of Bone Joint Surgery America. 84-A (12):2174-2178.

Powers, C.M., Chen, Y.J., Scher, I., Lee, T.Q., 2006. The influence of patellofemoral joint contact geometry on the modeling of three dimensional patellofemoral joint forces. Journal of Biomechanics. 39 (15):2783-2791.

Quapp, K.M., Weiss, J.A., 1998. Material characterization of human medial collateral ligament. Journal of Biomechanical Engineering, Transactions of the ASME. 120 (6):757-763.

Race, A., Amis, A.A., 1996. Loading of the two bundles of the posterior cruciate ligament: an analysis of bundle function in a-P drawer. Journal of Biomechanics. 29 (7):873-879.

Race, A., Amis, A.A., 1994 The mechanical properties of the two bundles of the human posterior cruciate ligament. Journal of Biomechanics. Jan; 27 (1):13-24.

Rajamani, K.T., Styner, M.A., Talib, H., Zheng, G., Nolte, L.P., Gonzalez Ballester, M.A., 2007. Statistical deformable bone models for robust 3D surface extrapolation from sparse data. Medical Image Analysis. 11 (2):99-109.

Ramaniraka, N.A., Terrier, A., Theumann, N., Siegrist, O., 2005. Effects of the posterior cruciate ligament reconstruction on the biomechanics of the knee joint: A finite element analysis. Clinical Biomechanics. 20 (4):434-442.

Ranawat, A.S., Ranawat, C.S., Slamin, J.E., Dennis, D.A., 2006. Patellar crepitation in the P.F.C. sigma total knee system. Orthopedics. 29 (9 Suppl):S68-70.

Recondo, J.A., Salvador, E., Villanúa, J.A., Barrera, M.C., Gervás, C., Alústiza, J.M., 2000. Lateral stabilizing structures of the knee: functional anatomy and injuries assessed with MR imaging. Radiographics. 20 Spec No S91-S102.

Restrepo, C., Hozack, W.J., Orozco, F., Parvizi, J., 2008. Accuracy of femoral rotational alignment in total knee arthroplasty using computer assisted navigation. Computer Aided Surgery. 13 (3):167-172.

Robinson, J.R., Bull, A.M., Thomas, R.R., Amis, A.A., 2006. The role of the medial collateral ligament and posteromedial capsule in controlling knee laxity. American Journal of Sports Medicine. 34 (11):1815-1823.

Robinson, J.R., Bull, A.M.J., Amis, A.A., 2005. Structural properties of the medial collateral ligament complex of the human knee. Journal of Biomechanics. 38 (5):1067-1074.

Robinson, J.R., Sanchez-Ballester, J., Bull, A.M., Thomas Rde, W., Amis, A.A., 2004. The posteromedial corner revisited. An anatomical description of the passive restraining structures of the medial aspect of the human knee. Journal of Bone and Joint Surgery Britain. 86 (5):674-681.

Sakane, M., Fox, R.J., Woo, S.L.Y., Livesay, G.A., Li, G., Fu, F.H., 1997. In situ forces in the anterior cruciate ligament and its bundles in response to anterior tibial loads. Journal of Orthopaedic Research. 15 (2):285-293.

Shahane, S.A., Ibbotson, C., Strachan, R., Bickerstaff, D.R., 1999. The popliteofibular ligament. An anatomical study of the posterolateral corner of the knee. Journal of Bone Joint Surgery Britain. 81 (4):636-642.

Shelburne, K.B., Pandy, M.G., 1997. Musculoskeletal model of the knee for evaluating ligament forces during isometric contractions. Journal of Biomechanics. 30 (2):163-176.

Shelburne, K.B., Torry, M.R., Pandy, M.G., 2006. Contributions of muscles, ligaments, and the ground-reaction force to tibiofemoral joint loading during normal gait. Journal of Orthopaedic Research. 24 (10):1983-1990.

Shim, V.B., Pitto, R.P., Streicher, R.M., Hunter, P.J., Anderson, I.A., 2008. Development and validation of patient-specific finite element models of the hemipelvis generated from a sparse CT data set. Journal of Biomechanical Engineering-Transactions of the Asme. 130 (5):

Shim, V.B., Pitto, R.P., Streicher, R.M., Hunter, P.J., Anderson, I.A., 2007. The use of sparse CT datasets for auto-generating accurate FE models of the femur and pelvis. Journal of Biomechanics. 40 (1):26-35.

Shirazi-Adl, A., Moglo, K.E., 2005. Effect of changes in cruciate ligaments pretensions on knee joint laxity and ligament forces. Computer Methods in Biomechanics and Biomedical Engineering. 8 (1):17-24.

Sigal, I., A., Hardisty, M., R., Whyne, C., M., 2008. Mesh-morphing algorithms for specimen-specific finite element modeling. Journal of Biomechanics.

Siston, R.A., Patel, J.J., Goodman, S.B., Delp, S.L., Giori, N.J., 2005. The variability of femoral rotational alignment in total knee arthroplasty. Journal of Bone Joint Surgery America. 87 (10):2276-2280.

Smirk, C., Morris, H., 2003. The anatomy and reconstruction of the medial patellofemoral ligament. Knee. 10 (3):221-227.

Song, Y., Debski, R.E., Musahl, V., Thomas, M., Woo, S.L.Y., 2004. A three-dimensional finite element model of the human anterior cruciate ligament: A computational analysis with experimental validation. Journal of Biomechanics. 37 (3):383-390.

Staeubli, H.U., Bollmann, C., Kreutz, R., Becker, W., Rauschning, W., 1999. Quantification of intact quadriceps tendon, quadriceps tendon insertion, and suprapatellar fat pad: MR arthrography, anatomy, and cryosections in the sagittal plane. American Journal of Roentgenology. 173 (3):691-698.

Stäubli, H.U., Schatzmann, L., Brunner, P., Rincón, L., Nolte, L.P., 1999. Mechanical tensile properties of the quadriceps tendon and patellar ligament in young adults. The American Journal of Sports Medicine. 27 (1):27-34.

Suggs, J., Wang, C., Li, G., 2003. The effect of graft stiffness on knee joint biomechanics after ACL reconstruction - A 3D computational simulation. Clinical Biomechanics. 18 (1):35-43.

Sugita, T., Amis, A.A., 2001. Anatomic and biomechanical study of the lateral collateral and popliteofibular ligaments. The American journal of sports medicine. 29 (4):466-472.

Taddei, F., Cristofolini, L., Martelli, S., Gill, H.S., Viceconti, M., 2006. Subject-specific finite element models of long bones: An in vitro evaluation of the overall accuracy. Journal of Biomechanics. 39 (13):2457-2467.

Testi, D., Zannoni, C., Cappello, A., Viceconti, M., 2001. Border-tracing algorithm implementation for the femoral geometry reconstruction. Computer Methods and Programs in Biomedicine. 65 (3):175-182.

Veltri, D.M., Deng, X.H., Torzilli, P.A., Maynard, M.J., Warren, R.F., 1996. The role of the popliteofibular ligament in stability of the human knee. A biomechanical study. The American journal of sports medicine. 24 (1):19-27.

Viceconti, M., Bellingeri, L., Cristofolini, L., Toni, A., 1998. Comparative study on different methods of automatic mesh generation of human femurs. Medical Engineering & Physics. 20 (1):1-10.

Viceconti, M., Davinelli, M., Taddei, F., Cappello, A., 2004. Automatic generation of accurate subject-specific bone finite element models to be used in clinical studies. Journal of Biomechanics. 37 (10):1597-1605.

Warren, L.F., Marshall, J.L., 1979. The supporting structures and layers on the medial side of the knee: an anatomical analysis. The Journal of bone and joint surgery American volume. 61 (1):56-62.

Weiss, J.A.: Computational modeling of ligament and tendon mechanics. pp 163-164. Beever Creek, CO, USA, ASME, New York, NY, USA, 1995

Weiss, J.A., Gardiner, J.C., Ellis, B.J., Lujan, T.J., Phatak, N.S., 2005. Three-dimensional finite element modeling of ligaments: technical aspects. Medical Engineering and Physics. 27 (10):845-861.

Weiss, J.A., Maker, B.N., Govindjee, S., 1996. Finite element implementation of incompressible, transversely isotropic hyperelasticity. Computer Methods in Applied Mechanics and Engineering. 135 (1-2):107-128.

Wismans, J., Veldpaus, F., Janssen, J., Huson, A., Struben, P., 1980. A three-dimensional mathematical model of the knee-joint. J Biomech. 13 (8):677-685.

Withrow, T.J., Huston, L.J., Wojtys, E.M., Ashton-Miller, J.A., 2006. The relationship between quadriceps muscle force, knee flexion, and anterior cruciate ligament strain in an in vitro simulated jump landing. American Journal of Sports Medicine. 34 (2):269-274.

Woo, S.L., Abramowitch, S.D., Kilger, R., Liang, R., 2006. Biomechanics of knee ligaments: injury, healing, and repair. Journal of Biomechanics. 39 (1):1-20.

Wu, Y.T., Millwater, H.R., Cruse, T.A., 1990. Advanced Probabilistic Structural-Analysis Method for Implicit Performance Functions. Aiaa Journal. 28 (9):1663-1669.

Wymenga, A.B., Kats, J.J., Kooloos, J., Hillen, B., 2006. Surgical anatomy of the medial collateral ligament and the posteromedial capsule of the knee. Knee Surgery in Sports Traumatology Arthroscopy. 14 (3):229-234.

Yao, J., Salo, A.D., Lee, J., Lerner, A.L., 2008. Sensitivity of tibio-menisco-femoral joint contact behavior to variations in knee kinematics. Journal of Biomechanics. 41 (2):390-398.

Yao, J., Snibbe, J., Maloney, M., Lerner, A.L., 2006. Stresses and strains in the medial meniscus of an ACL deficient knee under anterior loading: A finite element analysis with image-based experimental validation. Journal of Biomechanical Engineering. 128 (1):135-141.

Yau, W.P., Wong, J.W., Chiu, K.Y., Ng, T.P., Tang, W.M., 2003. Patellar clunk syndrome after posterior stabilized total knee arthroplasty. Journal of Arthroplasty. 18 (8):1023-1028.

Yoshii, I., Whiteside, L.A., Anouchi, Y.S., 1992. The effect of patellar button placement and femoral component design on patellar tracking in total knee arthroplasty. Clinical Orthopedics and Related Research. (275):211-219.

Zavatsky, A.B., 1997. A kinematic-freedom analysis of a flexed-knee-stance testing rig. Journal of Biomechanics. 30 (3):277-280.
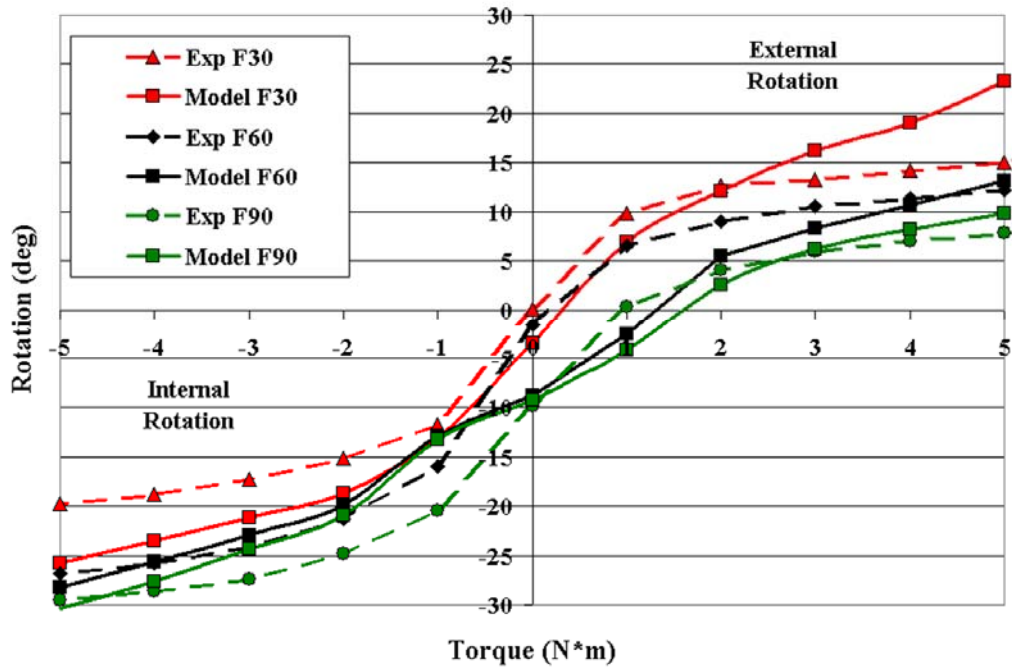
Figure A.1 Specimen #1 tibiofemoral internal-external torque-rotation experimental (Exp) and phase II optimized (Model) results at 30, 60 and 90° femoral flexion.
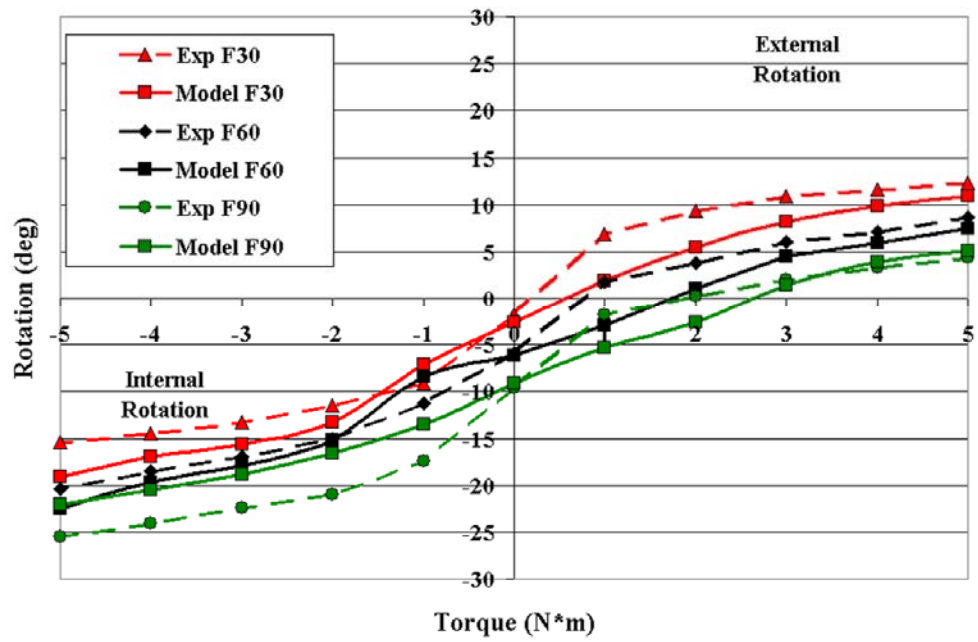
Figure A.2 Specimen #2 tibiofemoral internal-external torque-rotation experimental (Exp) and phase II optimized (Model) results at 30, 60 and 90° femoral flexion.
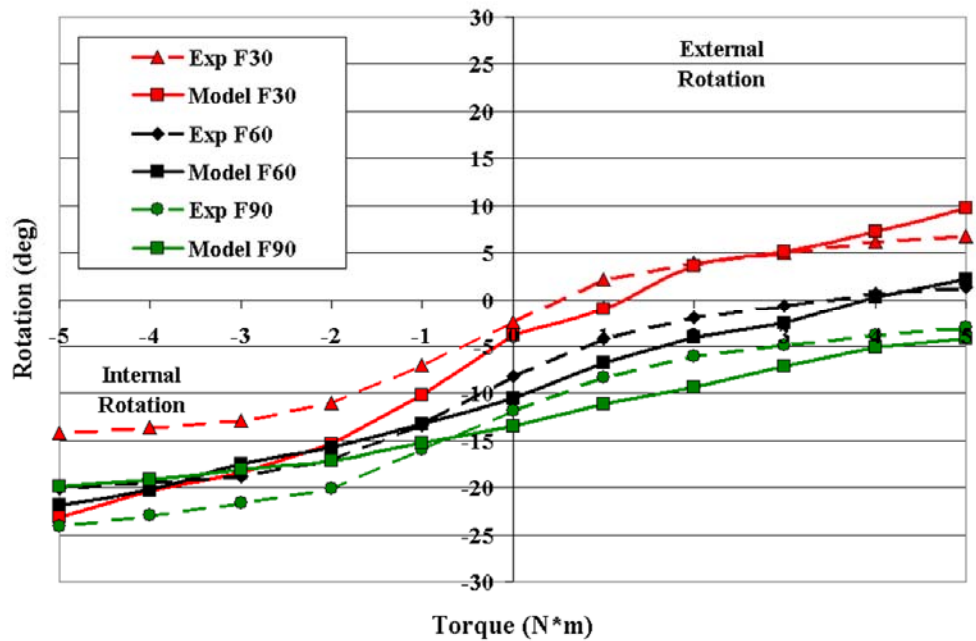

Figure A.3 Specimen #3 tibiofemoral internal-external torque-rotation experimental (Exp) and phase II optimized (Model) results at 30, 60 and 90° femoral flexion.
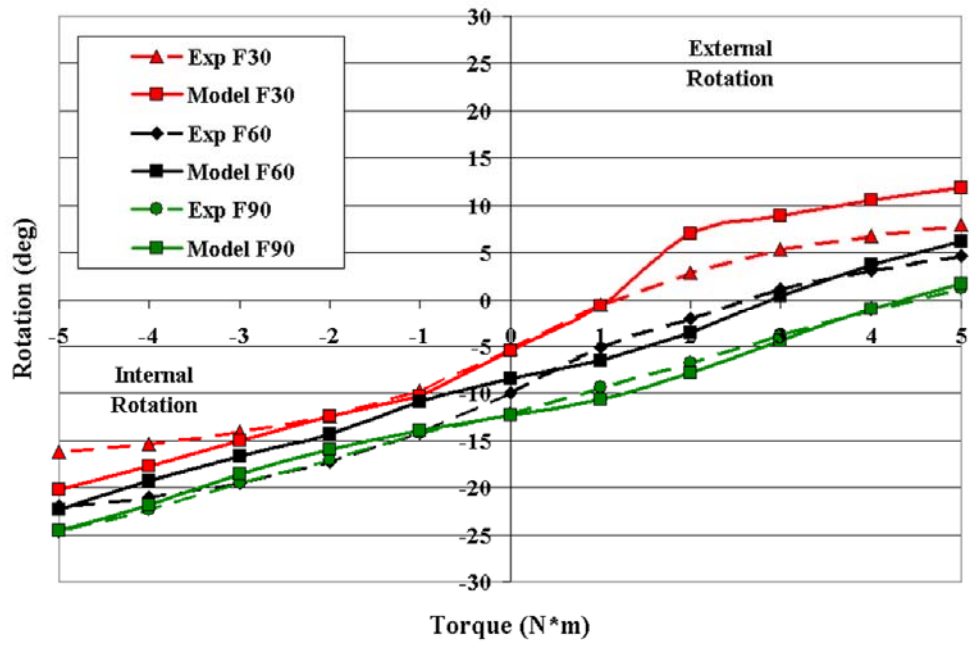
Figure A.4 Specimen #4 tibiofemoral internal-external torque-rotation experimental (Exp) and phase II optimized (Model) results at 30, 60 and 90° femoral flexion.